arXiv:1609.05415v1 [astro-ph.GA] 18 Sep 2016

# CHANDRA ACIS SURVEY OF X-RAY POINT SOURCES IN NEARBY GALAXIES. II. X-RAY LUMINOSITY FUNCTIONS AND ULTRALUMINOUS X-RAY SOURCES

Song Wang[1], Yanli Qiu[1,3], Jifeng Liu[1,2], and Joel N. Bregman[4]

## ABSTRACT

Based on the recently completed *Chandra*/ACIS survey of X-ray point sources in nearby galaxies, we study the X-ray luminosity functions (XLFs) for X-ray point sources in different types of galaxies and the statistical properties of ultraluminous X-ray sources (ULXs). Uniform procedures are developed to compute the detection threshold, to estimate the foreground/background contamination, and to calculate the XLFs for individual galaxies and groups of galaxies, resulting in an XLF library for 343 galaxies of different types. With the large number of surveyed galaxies, we have studied the XLFs and ULX properties across different host galaxy types, and confirm with good statistics that the XLF slope flattens from lenticular ($\alpha \sim 1.50 \pm 0.07$) to elliptical ($\sim 1.21 \pm 0.02$), to spirals ($\sim 0.80 \pm 0.02$), to peculiars ($\sim 0.55 \pm 0.30$), and to irregulars ($\sim 0.26 \pm 0.10$). The XLF break dividing the neutron star and black hole binaries is also confirmed, albeit at quite different break luminosities for different types of galaxies. A radial dependency is found for ellipticals, with a flatter XLF slope for sources located between $D_{25}$ and $2D_{25}$, suggesting the XLF slopes in the outer region of early-type galaxies are dominated by low-mass X-ray binaries in globular clusters. This study shows that the ULX rate in early-type galaxies is $0.24 \pm 0.05$ ULXs per surveyed galaxy, on a $5\sigma$ confidence level. The XLF for ULXs in late-type galaxies extends smoothly until it drops abruptly around $4 \times 10^{40}$ erg s$^{-1}$, and this break may suggest a mild boundary between the stellar black hole population possibly including 30 $M_\odot$ black holes with super-Eddington radiation and intermediate mass black holes.

[1]Key Laboratory of Optical Astronomy, National Astronomical Observatories, Chinese Academy of Sciences, Beijing 100012, China;
jfliu@bao.ac.cn, songw@bao.ac.cn

[2]College of Astronomy and Space Sciences, University of Chinese Academy of Sciences, Beijing 100049, China

[3]University of Chinese Academy of Sciences, Beijing 100049, China

[4]University of Michigan, Ann Arbor, MI 48109

*Subject headings:* catalogs – galaxies: general – X-rays: binaries – X-rays: galaxies

## 1. INTRODUCTION

X-ray observations of more than forty years have revealed a variety of X-ray point sources beyond the solar system in the Milky Way and Magellanic Clouds. Although the bright X-ray sources in the Milky Way are easily studied, many of them are not observable due to the heavy obscuration of the galactic disk, and one must correct for completeness when studying the statistical properties of Galactic X-ray binaries (e.g., Grimm et al. 2002). Studies of X-ray binaries in more distant galaxies may be free from the obscuration problem, and more importantly, provide us uniform samples of X-ray binaries in different environments. Much work has been done to study the X-ray source populations in distant galaxies since the lunch of *Einstein* (Fabbiano 1989) and *ROSAT* (Roberts & Warwick 2000), and a quantum leap in this field has been achieved with the *Chandra* mission (see Fabbiano & White 2006; Fabbiano 2006, for a review).

New classes of X-ray sources not previously seen in the Milky Way have emerged from studies of distant galaxies, such as the ultraluminous X-ray sources (ULXs), which were first detected by *Einstein* (Long & van Speybroeck 1983; Fabbiano 1989). ULXs are defined as extranuclear sources with an observed luminosity of at least $10^{39}$ erg/s, in excess of the Eddington limit of a neutron star. A large amount of both observational and theoretical work has focused on the nature of ULXs, including the high luminosity, the X-ray spectra and short time variability, the association with active star-forming regions, and the formation and evolution of ULXs (see Fabbiano 2005, 2006, for a review). Recently, it was generally believed that ULXs in nature appear in two categories: the long-sought intermediate mass black holes (IMBHs) as the seeds of supermassive black holes (Heger & Woosley 2002; Miller & Colbert 2004); or stellar mass black holes in a new ultraluminous accretion state (Makishima et al. 2000; King et al. 2001; Zezas & Fabbiano 2002).

The X-ray luminosity function (XLF) is a powerful tool for the characterization of the populations of discrete X-ray sources detected in nearby galaxies. Kilgard et al. (2002) studied three starburst and five spiral galaxies, and found that starburst galaxies have flatter XLF slopes than do normal spirals. Grimm et al. (2003) studied the X-ray sources (mainly high-mass X-ray binaries; HMXBs) in a dozen of late-type and starburst galaxies, and found that the total X-ray luminosity and the XLF scale with the star formation rate (SFR). While HMXB XLFs are typically described by straight power-laws, XLFs are typically described by broken or cut-off power-laws for low-mass X-ray binaries in early-type galaxies or re-

gions lacking current star formation. Mineo et al. (2013) reported the numbers of ULXs (in one colliding galaxy pair) are strongly correlated with the local SFR densities, but the luminosities of these sources show weak correlation with SFR densities.

In the general picture, starbursting galaxies have flatter XLFs than spiral or early-type galaxies, disagreements, however, exist for some important details of the XLFs. For low mass X-ray binaries (LMXBs) in galaxies lacking current star formation, the XLFs are typically described by broken or cut-off power-laws, with several possible but controversial knees: (*i*) The knees at a few $10^{37}$ erg s$^{-1}$ (Grimm et al. 2003; Gilfanov 2004) may be explained by accretion on neutron star from Roche lobe overflow, which is driven by gravitational wave emission when below $\sim\ 2\times10^{37}$ erg s$^{-1}$, and by magnetic stellar winds at higher luminosities (Postnov & Kuranov 2005). Some studies proposed that systems below $10^{37}$ erg s$^{-1}$ may be transients (Bildsten & Deloye 2004). However, Kim et al. (2006) did not find such a break in the LMXB XLF in two normal elliptical galaxies. (*ii*) The knees at a few $10^{38}$ erg s$^{-1}$ (Sarazin et al. 2000, 2001) may be consistent with the Eddington luminosity of normal neutron star (NS) binaries, the luminosity of massive neutron stars (NSs), He-enriched NS binaries (Ivanova & Kalogera 2006), or low-mass BH binaries. (*iii*) The knees at a few $10^{39}$ erg s$^{-1}$ (Jeltema et al. 2003) could be attributable to ULXs or small number statistics. In some sense, these discrepancies are expected, because those studies use different galaxy samples that are usually small (on the order of a dozen), and they adopt different methods to construct XLFs and different methods to correct for the survey incompleteness.

We have embarked on an effort to study the X-ray point sources, especially ULXs, in nearby galaxies with uniform procedures using the wealth of *Chandra* Data Archive after eight years' accumulation (Liu 2011, hereafter Paper I). As detailed in Paper I, 383 galaxies within 40 Mpc with isophotal major axis above 1 arcminute have been observed by 626 ACIS observations, and our uniform analysis of these observations has led to 11,824 point sources within the $2D_{25}$ isophotes of 380 galaxies, by far the largest extragalactic X-ray point source catalog of such. There are a large number of galaxies observed for each galaxy morphological type, making it possible to compare XLFs among galaxies of each type and between galaxies of different types with good statistics. Meticulous efforts have been made to identify the nuclear X-ray sources, so that we can excise them from the catalog and study the remaining ordinary X-ray binary populations.

In this paper, we study XLFs and statistical properties for ULXs for different samples of galaxies with uniform procedures. In section 2, we describe our treatments of the detection threshold and the foreground/background contamination estimates for extragalactic point source surveys. In section 3, we describe our procedures to construct a stitched survey for individual galaxies aided by an example, and present a library of XLFs for 343 galaxies.

In section 4, we describe how to construct surveys of a sample of galaxies, and present the XLFs and statistical properties for different samples of galaxies. We summarize our results and discuss the significance of the XLF break at $4 \times 10^{40}$ erg s$^{-1}$ in section 5.

## 2. TWO ISSUES FOR EXTRAGALACTIC SURVEYS

In carrying out extragalactic point source surveys, two issues are of particular importance: the incompleteness; and the foreground/background contaminations. Below we describe our methods to compute detection thresholds pixel by pixel for ACIS observations used in this work, and the different ways to estimate the foreground/background objects projected into the galaxies.

### 2.1. Detection Threshold

The sensitivity for an X-ray observation includes two issues, the detecting limit and the incompleteness. The first issue gives the minimum flux of a source that can be detected with a specific detection algorithm such as `wavdetect`, widely used for *Chandra* observations. The second issue gives the fraction of sources at certain fluxes that are missed by the detection algorithm. The XLF becomes artificially flattened at the faint end due to the missing sources close to the detect limits, and the missing source fraction must be known to correct for this flattening. These issues are usually addressed by extensive simulations such as those for the *Chandra* deep fields (Giacconi et al. 2001) and for the ChaMP project (Kim et al. 2004), in which fake sources at different flux levels at different positions on the CCD chips are simulated and detected. As shown by these simulations, the detect limit and the missing source fraction are very complicated functions of the off-axis angle and background level, and there are no satisfying analytical forms for such functions.

When constructing XLFs for this survey, we exclude the flattened part at the faint end affected by the missing sources. This ensures the XLFs are free of the artificial flattening problem by sacrificing the sensitivity range from the detect limit to where incompleteness begins. Then where does incompleteness come into play? We try to get the answer from the survey itself following Kong et al. (2003). Figure 1 shows the distribution of detection significance for all sources detected in 626 ACIS observations. As the detection significance decreases, the source number increases in a power-law form until $\sigma \approx 4$, beyond which the source number drops sharply from the expected power-law form. This indicates that incompleteness begins at $\sigma = 4$, regardless of the off-axis angles for the detection algorithm

used for our survey. As shown in Figure 1, the missing source fraction increases for lower detection significance, reaching 45% at $3\sigma$ and 85% at $2\sigma$.

The detection threshold is a complex function of off-axis angles (OAA), background counts per pixel, and different source counts (Kim & Fabbiano 2003). In general, the detection threshold increases as the effective background rate and the OAA increase, and as the source count decreases. The detection efficiency significantly decreases with the OAA, meaning more source counts are needed to achieve a similar detection sensitivity at larger off-axis radii compared to on-axis observations, due to the variation of the *Chandra* PSF with the OAA (Primini et al. 2011). As shown in Evans et al. (2010), the PSF close to the optical axis of the telescope is approximately symmetric with a 50% enclosed energy fraction radius of $\sim$ 0.3″ over a wide range of energies, but the PSF at 15″ off-axis is asymmetric, significantly extended, and strongly energy dependent, with a 50% enclosed energy fraction radius of $\sim$ 13″ at 1.5 keV. In this paper, the detection threshold for certain detection significance is derived from the survey itself. As shown in Figure 2a, the source counts increase monotonically with the detection significance, albeit with large dispersions. This dispersion, however, reduces greatly if we fix the OAA and the background level. In example, of the sources with $\sigma = 3.8 \sim 4.2$, 90% have between 8 and 25 source counts, but 90% have between 8 and 12 counts for the subset with OAA less than 2′ and background level between 0.01 and 0.03 count pixel$^{-1}$ (Figure 2b). To compute the detection threshold for $4\sigma$, we use sources with $\sigma$ between 3.8 and 4.2, and group them based on OAAs and background levels. For each group, we compute the average OAA, the average background level, and the average source count as the detection threshold. The resulting detection thresholds for $4\sigma$, as plotted in Figure 3, are used to calculate the detection threshold for any given OAA and background level with interpolation or extrapolation.

### 2.2. Estimates of Foreground and Background Objects

When studying X-ray point source populations in nearby galaxies, one needs to exclude the foreground stars and background QSO/AGNs projected into the host galaxies by chance. It would be best if we can identify the foreground/background objects with multiwavelength observations, but is impractical given the huge telescope time required to carry out such identifications for a large survey like this. Fortunately, we do not really need to know which are foreground/background objects for statistical work in this paper. What we really need is a statistical estimate, as the number of contaminating sources per flux interval, so that we can subtract these estimates from the observed number of sources per flux interval. Below we show two ways to make such statistical estimates for contaminating sources.

One conventional way to estimate the contamination from the foreground/background objects is to use the log$N$-log$S$ relation that predicts the number of X-ray sources per deg$^2$ $N$ as a function of flux $S$. Hasinger et al. (1993) derived a log$N$-log$S$ relation based on $ROSAT$ observations of the Lockman Hole region, where the differential form is $dN/dS = N_1 S^{-\beta_1}$ for $S > S_b$ and $dN/dS = N_2 S^{-\beta_2}$ for $S < S_b$, with $S$ in unit of $10^{-14}$ erg cm$^{-2}$ s$^{-1}$ in the 0.5–2 keV band, $S_b = 2.66 \pm 0.66$, $N_2 = 111 \pm 10$, $\beta_1 = 2.72 \pm 0.27$, $\beta_2 = 1.94 \pm 0.19$, and $N_1 = 238.1$. Mushotzky et al. (2000) derived a log$N$-log$S$ relation based on a long *Chandra* ACIS observation, where the number of sources over the flux range (2.3–70)$\times 10^{-16}$ erg cm$^{-2}$ s$^{-1}$ are given by $N(>S) = 185(\frac{S}{7\times10^{-15}})^{-0.7\pm0.2}$, with $S$ as the 0.5–2 keV flux. Giacconi et al. (2001) derived another log$N$-log$S$ relation based on the *Chandra* deep field source observations, where the number of sources over the flux range (2–200)$\times 10^{-16}$ erg cm$^{-2}$ s$^{-1}$ is given by $N(>S) = 370(\frac{S}{2\times10^{-15}})^{-0.85\pm0.15}$, with $S$ as the 0.5–2 keV flux.

Another way to estimate the contamination from the foreground and background objects makes use of observed fields void of nearby galaxies. From these blank fields outside $2D_{25}$ isophotes of any nearby galaxies, X-ray point sources should be detected and fluxes be computed from count rates with the same procedures as from fields within $2D_{25}$ isophotes of nearby galaxies. Then the number of sources in a flux interval $\Delta N(F_1, F_2)$ can be accumulated from these blank fields and serve as a template for contaminating sources after normalized by the surveyed area of these blank fields. This nearby galaxy survey, with its uniform analysis of 626 ACIS observations, naturally provides a collection of blank fields, i.e., the regions outside of $2D_{25}$ isophotes of galaxies. Figure 4 shows the number of contaminating sources per deg$^2$ as a function of flux derived from this collection of blank fields.

The contaminating sources from different estimates are compared in Figure 4. To enable the comparison between different contamination estimates, we plot them in Figure 4 as a function of *Chandra* ACIS-S3 count rate. Assuming $n_H = 2 \times 10^{20}$ cm$^{-2}$, one ACIS-S3 photon/count would correspond to the 0.5–2 keV flux $S$ of $2.57 \times 10^{-12}$ erg s$^{-1}$ used in the Hasinger log$N$-log$S$ relation assuming a power law with $\Gamma = 2$, the 0.5–2 keV flux $S$ of $2.35 \times 10^{-12}$ erg s$^{-1}$ used in the Mushotzky log$N$-log$S$ relation assuming a power law with $\Gamma = 1.4$, the 0.5–2 keV flux $S$ of $2.50 \times 10^{-12}$ erg s$^{-1}$ used in the Giacconi log$N$-log$S$ relation assuming a power law with $\Gamma = 1.7$, and the 0.3–8 keV flux $F$ of $7.90 \times 10^{-12}$ erg s$^{-1}$ used in $\Delta N(F_1, F_2)$ assuming a power law with $\Gamma = 1.7$. The fourth flux $F$ is the same as used for the source catalog in Paper I. As shown in Figure 4, the blank field estimate shows a knee around 0.01 count s$^{-1}$ like the Hasinger relation, but is significantly lower at fluxes below 0.001 count s$^{-1}$ than the Hasinger estimate. This is due to the poor extrapolation of the formula in Hasinger et al. (1993), in which the lower flux limit of the used data points is $\sim 10^{-15}$ erg cm$^{-2}$ s$^{-1}$ ($\sim 0.002$ count s$^{-1}$). The blank field estimate is roughly consistent with the Mushotzky and Giacconi estimates, but extends to much higher flux levels.

In this work, the blank field estimate is adopted for the foreground/background contamination. It is advantageous to use this estimate because the contaminating sources are detected and treated exactly the same way as the point sources associated with the galaxies. In addition, these blank fields have the same positions as the surveyed galaxies, making the foreground/background estimate free of cosmic variance. The other estimates are also computed for comparison and included in the XLF library in Section 3.3.

## 3. SURVEYS OF INDIVIDUAL GALAXIES

Many galaxies in our archival survey have multiple *Chandra* ACIS observations with different exposure times covering different parts of the galaxies. To maximize the galaxy coverage, we stitch all available observations together to construct surveys of individual galaxies. That is, when observations block each other, pixels in longer observations take precedence over pixels in shorter observations, which means only the deepest single observations are used for a given area of the sky, so as to make the stitched survey as deep as possible. In such cases, we first order the observations by their exposure times, then sum up pixels in each observation that are not blocked by pixels in any preceding observations. In the end, the stitched survey of a galaxy comes down to a collection of pixels possibly from different observations for that galaxy. We do not co-add/merge the observations with different exposures to avoid additional uncertainties, such as different PSFs for same sources at different off-axis radii, although this "stitching" method "wastes" some existing exposures. As shown by recent studies of XLFs for NGC 3031, different observations provide a consistent determination of its XLF despite measuring significant variability in a considerable fraction of sources (Sell et al. 2011). Thus, our stitched deep survey will yield XLFs similar to other surveys made by changing the order of observations, yet maximizes the power to study XLFs at the low luminosity end. Below we describe the surveyed sky area curve and the surveyed blue light curve computed from this collection of pixels in Section 3.1, show the construction of XLFs by an example in Section 3.2, and present a library of XLFs for individual galaxies in Section 3.3.

### 3.1. Surveyed Sky Area and Blue Light

Given a collection of pixels for a stitched survey, we first compute the survey area curve $A(>F)$ as the sky area in which an X-ray source above the limiting flux $F$ can always be detected in an observation or a survey. As discussed above, we compute $F$ from the $4\sigma$ detection threshold to avoid incompleteness. For each pixel in an ACIS observation, we

compute its OAA and the $4\sigma$ detection threshold in count as described above, where the background level is taken as the average of the whole ACIS chip. The detection threshold is converted to a count rate, given the exposure time and the vignetting factor that is computed as an analytical function of the OAA provided by the *Chandra* calibration team. To convert the count rate to the limiting flux, we use the response matrix at the chip center of that observation to account for *Chandra*'s response evolution over the past years. The limiting flux $F$ is then computed in 0.3–8 keV by assuming a power-law with $\Gamma = 1.7$ and Galactic absorption at the nominal pointing of that observation.

The survey area curve $A(>F)$ for a collection of pixels is computed by summing the area of the pixels for which the detection thresholds correspond to flux less than $F$. To compute $A(>F)$ for a galaxy, we compute for each pixel the separation $\alpha$ between the galaxy center and the pixel and compare to the elliptical radius $R_{25}$ of the $D_{25}$ isophotal ellipse along the great arc connecting the galaxy center and the pixel. A pixel is considered as in a galaxy if it is within the $2D_{25}$ isophote of the galaxy, or in a blank field if outside the $2D_{25}$ isophotes of any galaxies. For pixels within two overlapping galaxies, they belong to the closer galaxy in units of the elliptical radius. The survey area curve $A(>F)$ for a galaxy in this survey can be computed by summing the area of the pixels within this galaxy for which the detection thresholds correspond to flux less than $F$. Similarly, the survey area curves for parts of a galaxy, e.g., the region between $D_{25}$–$2D_{25}$, can be computed by considering only pixels within those parts.

To compare X-ray point source populations in different types of galaxies, we need to account for their variations in the stellar mass content, which can be deduced from the total light of the galaxy and the stellar mass-to-light ratio ($M/L$). Although the $M/L$ varies significantly in the optical compared to the near-infrared (Bell & De Jong 2001), the blue light from RC3 is used because of the lack of a consistent compilation of near-infrared magnitudes for these survey galaxies. The blue and near-infrared light trace different star population and suffer different extinction, which would result in different effective radii of galaxies. This could affect the computed light curve $\pounds(>F)$ and finally the $\pounds$-corrected XLF. However, as shown by McDonald et al. (2011), the radial distributions are quite similar for optical and near-infrared bands, thus the discrepancy of the $\pounds$-corrected XLF due to the bulge light may be small.

The surveyed blue light curve $\pounds_B(>F)$ for a galaxy gives the blue light as a measure of the stellar contents in which X-ray sources above $F$ can be detected in an observation. This curve is calculated the same way as the surveyed area curve $A(>F)$, except that we sum up the blue light in a pixel instead of the area of a pixel. To compute the blue light in a pixel, we compute the light profile for the galaxy from the total blue light $\pounds_B$ and the effective radius

$R_e$ that encloses 50% of the total light. This method is the same as used in our previous work on a *ROSAT*/HRI survey of nearby galaxies (Liu et al. 2006), and the procedures are also described in the appendix. The survey area curve $A(>L)$ and the surveyed blue light curve $\pounds_B(>L)$ on the luminosity intervals are calculated by converting $F$ to $L$ with $L = 4\pi D^2 F$ using the distance to the surveyed galaxy. To enable the summation of X-ray sources in different galaxies with the same luminosities, we have adopted the same luminosity intervals for all observations. This corresponds to different flux intervals for galaxies with different distances.

### 3.2. XLF for NGC 3031

NGC 3031 (M81) is a well-studied nearby galaxy at 3.63±0.3 Mpc (Freedman et al. 1994, using the Cepheid period-luminosity relationship). It is a Sb-type spiral with semi-major/minor axis of 13.5/7 arcmin, and has been observed with 19 *Chandra*/ACIS observations (Figure 5a) with exposure times ranging from 10 ksec to 50 sec spanning five years from 2000 to 2005 as tabulated in Sell et al. (2011). We stitch a deep survey of NGC 3031 out of these 19 observations by using all ACIS S3 and S2 pixels excluding those blocked by longer observations, which lead to a total of $3.1 \times 10^6$ pixels, or 218 arcmin$^2$, covering 73% of the $D_{25}$ isophote. This "stitched" survey covers 50% more sky area than any single ACIS observation, which covers at most 146 arcmin$^2$ with S3 and S2 chips.

With these $3.1 \times 10^6$ pixels, the surveyed sky area curve $A(>L)$ and the surveyed blue light curve $\pounds_B(>L)$ are computed following Section 3.1 and plotted on the luminosity grid in Figure 5b. The expected background/foreground sources for each luminosity bin $(L_1, L_2)$, which corresponds to flux bin $(F_1, F_2)$, is computed as $A(>L_1)$ * $\Delta N_{b/f}(F_1, F2)$, where $\Delta N_{b/f}(F_1, F2)$ is the number of sources per square degree from the blank fields void of nearby galaxies. X-ray point sources detected in these observations as listed in Table 3 of Paper I are assigned to the pixels where the source centroids are. Point sources above $4\sigma$ associated with any of the $3.1 \times 10^6$ pixels are considered detected in this stitched survey, and are assigned to luminosity bins based on their 0.3–8 keV luminosity. Of these detected, one point source is identified as the galactic nucleus of NGC 3031.

The XLF curves are computed given the detected sources, identified galactic nuclei, and the background/foreground estimates. The cumulative curves are plotted in Figure 5c, including the number of detected sources $N(>L)$, the numbers $N_{b/f}(> L)$ of expected background/foreground objects, the number of net sources $N_{net}(> L) = N(> L) - N_{b/f}(> L)$, and the number of net non-nuclear sources $N_{net,nG}(> L) = N(> L) - N_{Gnuc} - N_{b/f}(> L)$ . To correct the flattening of XLF at the low luminosity end due to less surveyed blue light,

we normalize the detected sources in each luminosity bin by the surveyed blue light curve $\pounds_B(>L)$. The $\pounds_B$-corrected number of net sources $N^{\pounds}_{net}(>L) = N(>L) * \pounds^{tot}_B/\pounds_B(>L) - N_{b/f}(>L)$, and the $\pounds_B$-corrected number of net non-nuclear sources $N^{\pounds}_{net,nG}(>L) = N(>L)*\pounds^{tot}_B/\pounds_B(>L) - N_{Gnuc} - N_{b/f}(>L)$; both $\pounds_B$-corrected curves are plotted in Figure 5d.

This stitched survey is sensitive to luminosities as low as $2 \times 10^{36}$ erg s$^{-1}$, and detects 99 point sources above the limiting luminosity $L_{X,lim} = 4 \times 10^{36}$ erg s$^{-1}$, defined as the $L_X$ at which the surveyed blue light is 50% of the total blue surveyed. In comparison, there are 122 point sources from all observations with detection significance above $4\sigma$ in at least one observation. Out of the 99 detected sources above $L_{X,lim}$, about 27.8 (28%) are expected to be background/foreground objects. There is one ULX detected above $2 \times 10^{39}$ erg s$^{-1}$, with 0.03 background/foreground objects expected, suggesting that the ULX is truly associated with NGC 3031. Recently, Sell et al. (2011) studied the XLFs in different regions and the entire galaxy of NGC 3031. Although it is difficult to make direct comparisons between their XLF and our XLF due to different detection thresholds and spectral models used, our XLF does show a similar knee at $10^{37}$ erg s$^{-1}$ that also appears in their XLF for the entire galaxy. This knee in our XLF is a true feature instead of an artificial flattening due to less surveyed blue light at the low luminosity end, because it is also present in the $\pounds_B$ corrected XLF as shown in Figure 5d.

### 3.3. XLFs for 343 Galaxies

XLFs for all surveyed galaxies are computed in the same way as for NGC 3031. There are 343 galaxies with surveyed area more than 30% of their $D_{25}$ isophotal sizes as listed in Table 1. For each galaxy, listed are the number of ACIS observations utilized in Paper I, the number of sources detected above $4\sigma$ from all observations, the number of sources detected above $4\sigma$ in the stitched deep survey, the sky coverage, the limiting luminosity $\log L_{X,lim}$, the number of sources detected above $L_{X,lim}$, the expected background/foreground for sources above $L_{X,lim}$, the number of ULXs from all observations, the net number of ULXs from this stitched survey, the expected background/foreground for sources above $2 \times 10^{39}$ erg s$^{-1}$, and the host galaxy properties. The survey depths for these galaxies span 4 orders of magnitude ranging from $3 \times 10^{35}$ to $6 \times 10^{39}$ erg s$^{-1}$. As plotted in Figure 6a, there are 27 galaxies with a limiting luminosity $L_{X,lim}$ below $10^{37}$ erg s$^{-1}$, and 107 galaxies with limiting luminosity $L_{X,lim}$ below $10^{38}$ erg s$^{-1}$. These 343 galaxies include 130 early-type galaxies, 187 spiral galaxies, 5 peculiars and 21 irregular galaxies. As compared to the RC3 (de Vaucouleurs et al. 1991) galaxies within 40 Mpc as shown in Figure 6b, our survey oversamples early galaxies, S0/a-

Sb galaxies and peculiars, and undersamples Sbc-Sm and irregular galaxies. A query against the NED service finds 15 starburst galaxies, and 121 AGNs of different kinds.

XLFs for the above 343 galaxies are created on the luminosity bins from $\log L = 34$ to $\log L = 42$ with $\Delta \log L = 0.05$. For each luminosity bin, we include the corresponding flux bin, the surveyed sky area, the surveyed blue light, the numbers of background/foreground objects estimated based on the Hasinger log$N$-log$S$ relation, the Mushotzky log$N$-log$S$ relation and the blank fields , the number of detected sources $N_{src}$, the number of galactic nuclear sources $N_{Gnuc}$, the number of net sources $N_{net} = N_{src} - N_{b/f}$, the number of net non-nuclear sources $N_{net,nG} = N_{src} - N_{Gnuc} - N_{b/f}$ , and the $\pounds_B$-corrected numbers of net sources $N^{\pounds}_{net} = N_{src} * \pounds^{tot}_B / \pounds_B(> L) - N_{b/f}$ and net non-nuclear sources $N^{\pounds}_{net,nG} = N_{src} * \pounds^{tot}_B / \pounds_B(> L) - N_{Gnuc} - N_{b/f}$. For each quantity, we include both the differential value for the luminosity bin and the cumulative value. For each galaxy, we present XLFs for sources within $D_{25}$ isophotes, which are used by studies in Section 4. We also present XLFs for sources within elliptical annuli of the galaxy from galactic center to $2D_{25}$ in steps of 0.1 elliptical radii, which can be used to study XLFs for sources in various parts of galaxies.

## 4. SURVEYS OF GALAXY SAMPLES

Studies of X-ray point source populations with individual galaxies are often limited by the small number of sources at high luminosities. For better statistics, it is conventional to combine X-ray sources from a sample of galaxies with certain properties. Our XLF library provides a large pool of galaxies to construct samples of galaxies. In the following, we describe the construction of XLFs from the total survey of all 343 galaxies and compute the statistical properties in Section 4.1, compare the XLFs and statistical properties for galaxy samples across different morphological types in Section 4.2, and compare the XLFs and statistical properties for galaxy samples with different SFRs in Section 4.3. To maximize the number of sources yet minimize the contamination of background/foreground objects, we compute XLFs and corresponding statistics for sources within $D_{25}$ isophotes unless specifically stated.

### 4.1. Total Survey of All Galaxies

A total survey of all 343 galaxies is constructed by summing up the stitched deep surveys of individual galaxies. As listed in Table 2, the combined survey detects 4970 sources above $4\sigma$ while all observations of these 343 galaxies detected 5920 X-ray point sources (including 282 ULXs above $2 \times 10^{39}$ erg s$^{-1}$). The combined XLF curves can be computed by directly

summing up (from individual galaxies in each luminosity bin): the surveyed sky area; the surveyed blue light; the estimated numbers of background/foreground objects; the number of detected sources; the number of identified galactic nuclei; the number of net sources; the number of net non-nuclear sources. The $\pounds_B$-corrected numbers of net sources and net non-nuclear sources can then be computed based on the combined surveyed blue light curve and the combined numbers. As shown in Figure 7a, the combined sky area coverage amounts to $\sim 10^8$ ACIS pixels (1.9 square degree) within the $D_{25}$ isophotes of 343 galaxies, and the combined blue light amounts to $2.5 \times 10^{12} L_\odot$ with 40% of the blue light above $2 \times 10^{38}$ erg s$^{-1}$. Figure 7b shows the cumulative curves for the detected sources, the estimated background/foreground objects, the ($\pounds_B$-corrected) net sources, the identified galactic nuclei, and the ($\pounds_B$-corrected) net nonnuclear sources.

The expected background/foreground objects are an increasing fraction of the detected sources toward lower luminosities. At luminosities above $10^{40}/10^{39}/10^{38}/10^{37}$ erg s$^{-1}$, there are 4.1/71.9/390.5/803.0 background/foreground objects expected, about 4.2%/11.9%/13.2% /18.3% of the 97/605/2955/4383 detected sources. This fraction goes to its maximum of 23.6% (1170.6/4970) at the lowest luminosity of $1.2 \times 10^{35}$ erg s$^{-1}$ that the combined survey can detect. Galactic nuclear sources are considered as another "contamination" for the normal X-ray binary population in nearby galaxies. As shown in Figure 7b, about half of the detected sources above $4 \times 10^{39}$ erg s$^{-1}$ are identified as galactic nuclei, while all detected sources above $10^{41}$ erg s$^{-1}$ are identified as galactic nuclei. We have listed in Table 2 the numbers of nonnuclear sources (or ULXs), of identified galactic nuclei, and of expected background/foreground objects for luminosities above $2 \times 10^{39}/4 \times 10^{39}/10^{40}$ erg s$^{-1}$ respectively. Also listed are the numbers with errors of ULXs per surveyed galaxy as an indicator for ULX frequency, and of ULXs per $10^{10} L_\odot$ surveyed blue light with error as a normalized indicator.

The normal X-ray binary population in nearby galaxies can be described by the net nonnuclear sources. At the low luminosity end, the net nonnuclear curve flattens due to less surveyed blue light. After correction by the combined surveyed blue light curve, the net nonnuclear source curve can be described by a power-law between a few $\times 10^{38}$ erg s$^{-1}$ and $\sim 10^{40}$ erg s$^{-1}$. The $\pounds_B$-corrected curve below $10^{38}$ erg s$^{-1}$ appears to have a flatter power-law slope. This may reflect a true feature of the X-ray binary population, or it could be caused by the insufficient correction for the surveyed blue light. As shown in Figure 8a, the "raw" differential histogram of net non-nuclear sources can be described by a power-law until it bends over with a sharp break around $2 \times 10^{38}$ erg s$^{-1}$. After corrected by the surveyed blue light curve, the curve is less bent and the break moves toward slightly higher luminosities. There are only two sources detected above $2 \times 10^{40}$ erg s$^{-1}$ as shown in the differential histogram; this leads to a cut-off around this luminosity in the cumulative curve in Figure 7b.

Throughout the work, the differential histogram of net non-nuclear sources are fitted with a single power-law of $dN(>L)/dL = AL_{39}^{-\alpha}$, or a broken power-law of $dN(>L)/dL = A(L/L_b)^{-\alpha}$ for $L \leq L_b$ and $dN(>L)/dL = A(L/L_b)^{-\alpha 2}$ for $L \geq L_b$ if the reduced $\chi^2_\nu > 1$ for the single power-law fit. Furthermore, The $\chi^2$ test is used to determine which is statistically acceptable. Here A is normalized by the total surveyed blue light to enable comparison across different galaxy samples. The parameters are obtained through minimizing $\chi^2 = \sum_i (N(L_i) - N_i)^2/e_i^2$, with $L_{39}$ as the luminosity in unit of $10^{39}$ erg s$^{-1}$, $L_i$ as the central luminosity of a luminosity bin, $N_i$ as the number of net nonnuclear sources in the luminosity bin, and $e_i$ as the Poisson error for the number of detected sources in the luminosity bin. To reduce the effects of possible insufficient $\pounds_B$ corrections, we only fit the luminosity range above which $\pounds_B(>L)$ exceeds 30% of the total surveyed blue light. We further restrain our fit to below the luminosity above which there are only two ULXs found. As shown in Figure 8b, the differential histogram for this total survey can be fitted by a single power law of $A = 0.2$ and $\alpha = 0.98$ with $\chi^2/\mathrm{dof} = 86.8/49$, or fitted with a broken power law of $A = 0.21$, $\alpha = 0.51$, $\log L_b = 38.4$, $\alpha_2 = 1.1$ with $\chi^2/\mathrm{dof} = 48.8/47$ (Table 3). When the significance level is set as $\alpha = 0.05$, the critical value of $\chi^2$ distribution for the broken power law (dof = 47) is 64.001, greater than 48.8; the critical value for the single power law (dof = 49) is 66.339, less than 86.8. Therefore, not only is the broken power law is a better fit, it is statistically acceptable while the single power-law fit must be rejected. The $1\sigma$ statistical uncertainty is determined during the fitting.

### 4.2. Galaxies of Different Types

The above total survey uses all galaxy types known to have a mixture of different X-ray binary populations, and the explanation of the XLF is rather difficult. Here we try to isolate different X-ray binary populations by studying them in different types of galaxies. We first divide them into early-type galaxies and late-type galaxies, then we divide them further into ellipticals and lenticulars for early-type galaxies, and S0/a-Sa, Sab-Sb, Sbc-Sc, Scd-Sd, Sdm-Sm for spiral galaxies, and irregular and peculiar galaxies. For each sample of galaxies, the survey statistics and the ULX statistics are computed as for the above total survey and listed in Table 2. The cumulative and differential XLF curves are computed for all galaxy samples as for the total survey. The differential curves of the net non-nuclear sources are fitted with a single power-law, and a broken power-law if a single power-law does not fit well. The resulted parameters are listed for the single power law and for the broken power law in Table 3.

The cumulative and differential net non-nuclear source curves for different galaxy sam-

ples are overplotted to facilitate comparison between different galaxy types. As is obvious from Figure 9a,b, the XLF is much steeper for early-type galaxies than for late-type galaxies. X-ray sources from late-type galaxies dominate the mixed total survey above a few $10^{38}$ erg s$^{-1}$, while X-ray sources from early-type galaxies dominate at lower luminosities. The late-type galaxy sample is dominated by spiral galaxies, with very few X-ray sources from the irregular galaxy sample and the peculiar galaxy sample. A single power-law can fit the XLFs for irregular/peculiar galaxy samples well, and no broken power-law are fitted given the small number of X-ray sources from these two samples. Despite the huge difference in the number of X-ray sources in different samples, it is clear that the slopes for XLFs change significantly for different galaxy types, becoming flatter and flatter in the order of early-type galaxies, late-type galaxies, spiral galaxies, peculiars and irregulars.

The cumulative and differential XLF curves for early-type and subtype (elliptical and lenticular) galaxies are plotted in Figure 10. While earlier works suggest that ULXs in early-type galaxies are mostly background/foreground objects (e.g., Irwin et al. 2004), this *Chandra* ACIS survey does find dozens of ULXs above $2 \times 10^{39}$ erg s$^{-1}$ that are significantly more than predicted by the background/foreground estimate. Indeed, the net non-nuclear source curve extends smoothly down to a few $10^{39}$ erg s$^{-1}$, with a possible bend down around $10^{39}$ erg s$^{-1}$. The quantitative fitting results prove that a broken power-law fit (as overplotted in Figure 10b) is indeed better than a single power-law on a 98.5% confidence level (F test). Above $6 \times 10^{39}$ erg s$^{-1}$, there appears to be an extra population of a dozen of ULXs in addition to the power-law fit. Inspection of the sub-type samples shows that this extra population mainly comes from elliptical galaxies, while the XLF curve for lenticular galaxies show a cut-off at $6 \times 10^{39}$ erg s$^{-1}$. There are 2–9 times more ULXs above $2 \times 10^{39}$ erg s$^{-1}$ per elliptical galaxy than per lenticular galaxy. When normalized by the surveyed blue light, the ULX density in the elliptical galaxies is 1–4 times higher than that in the lenticular galaxies. For less luminous sources, the $\pounds_B$ normalized source density in elliptical galaxies is about 2 times higher than that in the lenticular galaxies.

The XLF curves for spiral and subtype galaxies are plotted in Figure 11. The net non-nuclear source curve for the spiral galaxy sample extends down smoothly with a gradual bend down until it cuts off at $3 \times 10^{40}$ erg s$^{-1}$. Quantitative fitting to the differential curve shows that a broken power-law (as overplotted in Figure 11b) is slightly better than a single power-law on a 69% confidence level. For the subtypes, a broken power law fit is a significant improvement than a single power-law for Sab-Sb galaxies, while only a slight improvement for S0/a-Sa galaxies. However, it is not clear whether the power-law break is caused by the insufficient $\pounds_B$ correction. A single power law is a good fit for Sbc-Sc, Scd-Sd and Sdm-Sm galaxies, and no broken power law fits are tried due to the small number of X-ray sources for the latter two subtypes. For $L_X > 10^{39}$ erg s$^{-1}$, the XLF slopes are similar for S0/a

to Sc galaxies, but becomes flatter as the subtype goes later as shown in Figure 11b. Not surprisingly, there are more ULXs in late-type galaxies than in early-type galaxies. With better statistics from our large sample, we find that the number of ULXs per late-type galaxy is 2–4 times higher than the number per early-type galaxy for ULXs above $2 \times 10^{39}$ erg s$^{-1}$, and is 4–10 times higher for ULXs above $4 \times 10^{39}$ erg s$^{-1}$. The number of ULXs per surveyed galaxy peaks at Sbc-Sc galaxies, and the number of ULXs per $10^{10} L_{\odot}$ surveyed blue light peaks at later galaxy types, consistent with previous findings (Liu et al. 2006; Swartz et al. 2008).

The X-ray source density per surveyed stellar mass is compared among different host galaxy types. For ULXs above $2 \times 10^{39}$ erg s$^{-1}$, the cumulative source density ($U/L_B$ as listed in Table 2) is the highest for peculiars and irregulars, and decreases along the sequence of spirals, ellipticals and lenticulars. The highest cumulative source densities in peculiars and irregulars clearly indicate a link to their high SFR and young stellar populations. This cumulative source density is not always in agreement with the differential source density, because it also depends on the brightest source detected in the galaxy sample. To estimate the differential source density, we normalize the best-fit XLF models by the surveyed blue light, overplotted in Figure 12. At luminosities around $2 \times 10^{39}$ erg s$^{-1}$, the differential source density in irregular galaxies is the highest, which is 1.3 (2.4, 5.6, 20) times higher than in peculiar (spiral, elliptical, lenticular) galaxies. The trend is reversed at luminosities around $2 \times 10^{38}$ erg s$^{-1}$, and the differential source density in irregular galaxies becomes the lowest, while it is 1.37 (1.45, 1.55, 2.47) times higher in spiral (peculiar, lenticular, elliptical) galaxies. For spiral subtypes, the differential source density is lowest in Sdm-Sm galaxies at $2 \times 10^{38}$ erg s$^{-1}$, and increases for earlier and earlier subtypes. The trend is reversed at luminosities around $2 \times 10^{39}$ erg s$^{-1}$, except for that the source density in Sdm-Sm galaxies is lower than in Scd-Sd galaxies. However, the source density in Sdm-Sm galaxies does exceed that in Scd-Sd galaxies at luminosities above $7 \times 10^{39}$ erg s$^{-1}$. Note that the levels of significance for these differences are low due to the large uncertainties. Figure 13a displays the fitted XLF slopes in a quantitative way, which shows the flatting trend from early-type to late-type galaxies.

### 4.3. Galaxies with Different SFRs

The correlation between the XLF slope (also ULX density) and the galaxy type sequence suggests that X-ray source populations at high luminosities are linked to star formation activities (Ranalli et al. 2003; Grimm et al. 2003; Gilfanov et al. 2004a; Mineo et al. 2012), which are believed to be more prominent for later galaxy types. To quantify the relation between

star formation and the ULX phenomenon, we group the galaxies based on their SFRs. The SFR is calculated with SFR($M_\odot$/yr) $= 4.5 \times 10^{-44} \times L$ (60 $\mu$m) (Rosa-González et al. 2002). The flux densities at 60 $\mu$m are taken from the IRAS point source catalog (IPAC, 1986), with some nearby galaxies from Rice et al. (1988). For galaxies that are not detected, the $3\sigma$ upper limit is calculated by adopting noise levels of 8.5 mJy/arcmin$^2$ (Rice et al. 1988). The calculated rates are compared to the compilation of Grimm et al. (2003) for 11 galaxies, and are consistent with their rates within 50% without systematic biases. We put the galaxies into three groups based on the SFR from 60 $\mu$m emission, `sfrl02` for 208 galaxies with SFR upper limits or SFR $< 0.2$ $M_\odot$/yr, `sfrg02` for 90 galaxies with SFR $> 0.2$ $M_\odot$/yr but $< 2$ $M_\odot$/yr and an average of 0.76 $M_\odot$/yr, and `sfrg2` for 45 galaxies with SFR $> 2$ $M_\odot$/yr and an average of 6.6 $M_\odot$/yr. Note that a galaxy in `sfrg2` does not necessarily have a truly high star formation rate because the 60 $\mu$m emission may come from the AGN instead of the dust associated with star formation; indeed, 27 out of 45 galaxies in this group host AGNs. To construct a sample of galaxies with truly high SFRs, we build a group `Sbrst` of 15 galaxies identified as starburst galaxies in NED with an average SFR of 8.5 $M_\odot$/yr.

The cumulative and differential XLF curves are plotted in Figure 14 for galaxy samples with different SFRs. For galaxy samples with gradually higher SFRs, the luminosity of the most luminous sources becomes higher, and the XLF slope becomes flatter. For the `sfrl02` sample, a broken power-law with a break around $4 \times 10^{38}$ erg s$^{-1}$ fits the differential XLF better than a single power-law at a 90% confidence level. For all other three samples with higher star formation rates, the differential XLF curves can be well fitted with a single power-law with $\chi^2_\nu < 1$, with the slope decreasing from $\alpha \sim 1.2$ to $\alpha \sim 0.5$. As shown in Figure 12d, the $\pounds_B$-normalized XLFs reveal a higher source density above a few $10^{39}$ erg s$^{-1}$ for samples with gradually higher SFRs; the trend gets reversed at luminosities of a few $10^{38}$ erg s$^{-1}$ for all except for the `sfrg2` sample which lacks sources below $10^{39}$ erg s$^{-1}$. As listed in Table 2, the cumulative ULX rates become larger for samples with higher SFRs, albeit not in a linear way. For example, the SFR for `Sbrst` is 11 times higher than for `sfrg02`, but the number of ULXs above $2 \times 10^{39}$ erg s$^{-1}$ per surveyed galaxy is 4.5 times higher, and the $\pounds_B$-normalized ULX rate is 3.2 times higher. Figure 13b displays the fitted XLF slopes for galaxies with different SFRs, which clearly shows the flatting trend with increasing SFRs.

## 5. DISCUSSION

Some often-debated questions of XLFs for nearby galaxies could be addressed, with the large number of surveyed galaxies and resulting X-ray point sources, combined with the uniform procedures devised for this survey.

### 5.1. XLF Breaks

Different break luminosity may reflect the differences in the binary formation mechanisms (Voss et al. 2009), the binary configurations and consequently the accretion rates of the X-ray binaries in different types of galaxies. Some studies of X-ray point sources in early-type galaxies have identified an XLF shape that required two power-laws with a break around $3 \times 10^{38}$ erg s$^{-1}$ (Sarazin et al. 2000). However, such a break may result from biases affecting the detection threshold of the data (Kim & Fabbiano 2003). Kim & Fabbiano (2004) analyzed 14 early-type galaxies with varying sizes of point source samples and found that, although XLFs of individual galaxies may not require a broken power law, the combined differential XLF shows a statistically significant break around $L_b = (5 \pm 1.6) \times 10^{38}$ erg s$^{-1}$ with a slope of $\alpha = 1.8 \pm 0.2$ below $L_b$ and $\alpha = 2.8 \pm 0.6$ above $L_b$. Using a *Chandra* survey of LMXBs in 24 early-type galaxies, Humphrey & Buote (2008) acquired a best-fit power law for the composite XLF, with a break at $(2.21^{+0.65}_{-0.56}) \times 10^{38}$ erg s$^{-1}$, and slopes being $1.40^{+0.10}_{-0.13}$ and $2.84^{+0.39}_{-0.30}$ below and above it. It is suggested that the lower end of the XLF is mainly populated by neutron star X-ray binaries (e.g., ultracompact binaries that form predominantly in star clusters; Bildsten & Deloye 2004), while the upper end of the XLF is mainly populated by black hole X-ray binaries (Ivanova & Kalogera 2006). The break would correspond to the Eddington luminosity of massive neutron stars; if always true for individual galaxies, locating this break in the XLF for an early-type galaxy may allow us to determine the distance of the galaxy.

This survey confirms that the break is present in the composite XLFs for both early-type galaxies and late-type galaxies (e.g., Kim & Fabbiano 2004; Humphrey & Buote 2008). The composite differential XLF for 130 early-type galaxies shows a significant break around $L_b = (8.9 \pm 0.2) \times 10^{38}$ erg s$^{-1}$ (or 4.6 $L_{\rm Edd}$ of a 1.5 $M_\odot$ neutron star) with a slope of $\alpha = 1.0 \pm 0.03$ below $L_b$ and $\alpha = 2.3 \pm 0.2$ above $L_b$. The break is also present in the XLFs for the sample of 55 elliptical galaxies at a break luminosity of $L_b = (4.5 \pm 0.2) \times 10^{38}$ erg s$^{-1}$ and for the sample of 75 lenticular galaxies at a break luminosity of $L_b = (7.4 \pm 0.3) \times 10^{38}$ erg s$^{-1}$. The composite XLF for early-type galaxies in this survey are flatter than those in Kim & Fabbiano (2004) and Humphrey & Buote (2008), because we have excluded the background/foreground contaminating sources that are present in larger numbers at lower luminosities.

The higher break luminosity of early-type galaxies in this paper is examined. First, we study the systematic effect due to the observation bias since we are not dealing with a truly serendipitous survey. A simulation ($10^4$ runs) is performed that 100 galaxies are randomly selected from the 130 early-type galaxies and the composite XLF is fitted with a broken power law. Figure 15 shows the distribution of the fitting parameters compared to the results in

this paper. The $1\sigma$ systematic uncertainty is $0.08\times10^{38}$ erg s$^{-1}$ for the break luminosity, which is too small to affect the fitting results. Another possible bias is due to that there may be more nearby lower optical luminosity galaxies, which preferentially populate the low $L_X$ part of the XLF, while the higher optical luminosity galaxies contribute more higher $L_X$ objects. For distant galaxies ($D \gtrsim$ 30–50 Mpc), sometimes *Chandra* resolution becomes insufficient and only the total luminosity of the galaxy can be measured (Gilfanov et al. 2004c). To examine this bias, we divide the early-type galaxies into three samples as 0-20 Mpc (68 galaxies), 10-30 Mpc (95 galaxies), and 20-40 Mpc (62 galaxies), then perform the XLF fittings. The fitted breaks are $8.1\times10^{38}$, $9.8\times10^{38}$, and $1.3\times10^{39}$ erg s$^{-1}$, respectively. A small bias does exist, however, it can not explain the discrepancy between this paper and previous studies. Actually, both the samples in Kim et al. (2004) and Humphrey & Buote (2008) included galaxies with different distances, and these studies may also suffer from this bias. Therefore, we think the higher break luminosity in this paper is real. Finally, we investigate the bias induced by the $B$-band luminosity correction. One elliptical sample (NGC1399, NGC1407, NGC3379, NGC4365, NGC4374, NGC4472, NGC4621, NGC4636, NGC4649, and NGC4697) and one spiral sample (NGC253, NGC628, NGC891, NGC2403, NGC3031, NGC3628, NGC4631, NGC4945, NGC6946, and NGC7793) are chosen to produce a composite XLF, respectively. Both of the XLFs are corrected by the $B$-band and $K$-band luminosity, and then fitted with a broken power law. The $K$-band luminosity for these galaxies are from Jarrett et al. (2003) and Kim & Fabbiano (2004). The fitted break luminosity is $2.1\times10^{38}$ erg s$^{-1}$ for the ellipticals with $B$-band correction, below that ($2.7\times10^{38}$ erg s$^{-1}$) with $K$-band correction. For the spirals, the break luminosities are $7.2 \times 10^{38}$ and $1.2 \times 10^{39}$ erg s$^{-1}$ for the XLFs with $B$- and $K$-band luminosity correction, respectively. These suggest that the blue light correction may be slightly insufficient for correcting the XLF in the low luminosity side.

The dependency of the break luminosity on galaxy age is then examined. We collect (averaged) ages of elliptical galaxies from previous studies (Trager et al. 2000; Terlevich & Forbes 2002; Thomas et al. 2005; Sánchez-Blázquez et al. 2006; Annibali et al. 2007), and obtain seven young ($<$ 5 Gyr) and twenty old ($\geq$ 5 Gyr) elliptical samples with detection thresholds below $10^{38}$ erg s$^{-1}$. The fitted break luminosity is $7.08\times10^{38}$ and $4.67\times10^{38}$ erg s$^{-1}$ for the young and old elliptical samples, respectively. The age effect indicates possible presence of binaries with massive neutron stars or He-enriched neutron stars (Podsiadlowski et al. 2002; Kim & Fabbiano 2004) in young elliptical galaxies. This may account for the higher break luminosity in this paper, since there are a group of young early-type galaxies in our sample, while in previous studies, few such galaxies were included. In addition, Fragos et al. (2008) reported at early times ($<$ 5–6 Gyr) of one galaxy, the XLF receives notable contributions from intermediate-mass X-ray binaries, and that more luminous sources at earlier

times makes the shape of the XLF flatter.

The composite differential XLF for 213 late-type galaxies shows a break, although less significant, around $L_b = (6.3 \pm 0.3) \times 10^{38}$ erg s$^{-1}$ with a slope of $\alpha = 0.6 \pm 0.03$ below $L_b$ and $\alpha = 1 \pm 0.05$ above $L_b$. Note that these breaks are the results of combining galaxies with different XLFs, and are not necessarily present in individual galaxies, even if the break is universal and the composite XLF is representative of the sample XLF. For instance, a galaxy may not sample the population enough (i.e., too few sources) to unveil the break. In this sense, this break can not be used to determine the distance of host galaxies.

### 5.2. XLF Normalizations and Slopes

The large number of surveyed galaxies in this study allows to reveal how the XLFs change over different galaxy types of different galaxy properties. In Section 4.2, we normalize the best-fit XLF models by the surveyed blue light to estimate the differential source density, and one obvious trend shown in Figure 12 is that the $\pounds_B$ normalized X-ray point source density at luminosities below $10^{38}$ erg s$^{-1}$ decreases from elliptical to lenticular, to spiral, to peculiar and to irregular galaxies. For instance, the source density around $10^{38}$ erg s$^{-1}$ are 1.99±0.35/1.51±0.65/1.07±0.14/ 1.06±0.75/0.60±0.14 for these galaxies. While the blue light $\pounds_B$ is intended as a mass indicator, there is a trend for the mass-to-blue light ratio to decrease along the sequence of galaxy types because the stars in these galaxies become progressively younger, bluer, and brighter on average. In addition, the same amount of mass corresponds to decreasing number of stars/binaries along the sequence because the stars in these galaxies become progressively more massive on average. Another contributing factor is the globular cluster (GC) specific frequency, which decreases from elliptical to spiral galaxies. This leads to less X-ray binaries along the sequence because large fractions (20%-70%) of X-ray binaries are formed through stellar interactions in GCs as confirmed by observations (e.g., Sarazin et al. 2003).

Another obvious trend revealed in this study is that the XLF slopes become flatter from early-type to late-type galaxies, as already revealed by previous studies of smaller samples. For example, Kilgard et al. (2002) presented a comparison of XLFs of four nonstarburst spiral galaxies and three starburst galaxies, with the slopes determined from ∼1.3 to 0.5. Using *Chandra* observations of 32 nearby spiral and elliptical galaxies, Colbert et al. (2004) determined the power-law index as ∼1.4 for elliptical galaxies, and 0.6-0.8 for spiral and starburst galaxies. The large number of galaxies in this study also allows to confirm this trend for subtypes of galaxies, that is, the XLF slope flattens from lenticular ($\alpha \sim 1.50 \pm 0.07$) to elliptical ($\sim 1.21 \pm 0.02$), to spirals ($\sim 0.80 \pm 0.02$) of S0/a-Sa ($\sim 0.98 \pm 0.03$), Sab-Sb

($\sim 0.78 \pm 0.03$), Sbc-Sc ($\sim 0.70 \pm 0.04$), Scd-Sd ($\sim 0.54 \pm 0.04$) to Sdm-Sm ($\sim 0.34 \pm 0.17$) subtypes, to peculiars ($\sim 0.55 \pm 0.30$), and to irregulars ($\sim 0.26 \pm 0.10$).

A flatter XLF slope means a larger population of X-ray sources at high luminosities (i.e., a larger ULX population), and such an XLF slope evolution suggests a connection between the ULX population and the star formation activities, which are believed to be more prominent in later type/subtype galaxies (Zezas et al. 1999; Roberts & Warwick 2000; Fabbiano et al. 2001; Colbert et al. 2004). Most ULXs found in regions of star formation are HMXBs (King 2004), and a significant correlation has been found between these ULXs and young OB associations (Swartz et al. 2009). Indeed, studies of galaxy samples with different SFRs do show a monotonic increase of the ULX rate with the SFR (Mineo et al. 2013), and the XLF slope becomes monotonically flatter for higher SFRs. Different shape of XLFs (e.g., breaks) of HMXBs and LMXBs can be used to diagnose on-going star formation, while non-detection of luminous sources immediately constrains the star formation rate of the galaxy (Gilfanov 2004). The XLF evolution with different galaxy types may reflect a flatter mass distribution for the compact objects in later type galaxies, meaning more massive black holes in later type galaxies. Alternatively, this may reflect more binaries at higher Eddington luminosities in later type galaxies, due to higher accretion rates from more massive and younger secondaries in later type galaxies.

### 5.3. Radial Dependency

As mentioned in Section 3.3, for each galaxy, we determine XLFs for sources within elliptical annuli of the galaxy from galactic center to $2D_{25}$ in steps of 0.1 elliptical radii, which can be used to study the radial dependency of XLF for different galaxy types.

Figure 16 presents the cumulative curves for sources in various parts of early-type and late-type galaxies. Only galaxies with most of the $2D_{25}$ region having been observed are used, and this leads to a sample of 101 early-type and 189 late-type galaxies. It seems that the XLF slopes of late-type galaxies are similar for different parts of galaxies. In contrast, The XLF slopes of early-type galaxies become flatter for sources between $D_{25}$ and $2D_{25}$, indicating a larger proportion of bright sources in the outer part of elliptical galaxies. The cumulative curves are fitted with a single power-law of $N(> L) = AL_{39}^{-\alpha}$, with results shown in Figure 16b.

The radial distribution of sources, which is normalized to the actually observed area of each individual annulus in unit of pixel, is determined for different galaxy types (Figure 17). Here we select the galaxies with detection thresholds below $10^{38}$ erg s$^{-1}$, and use the sources

brighter than $10^{38}$ erg s$^{-1}$ to avoid selection effects. Also, only galaxies with most of the $2D_{25}$ region having been observed are used, and this leads to a sample of 66 early-type and 120 late-type galaxies. The radial distribution of X-ray sources in early-type galaxies is slightly flatter than the $B$-band surface brightness. Previous studies showed that in elliptical galaxies, the spatial distribution of GC LMXBs is more extended than field LMXBs (Kim et al. 2006; Kundu et al. 2007), and the surface density of (blue) GC LMXBs exceeds the stellar surface brightness when the radius increases (Paolillo et al. 2011). Therefore, the slight excess of X-ray surface brightness in Figure 17a may suffer from the GC LMXBs (Mineo et al. 2014a). Another feature is that the distribution of luminous sources ($10^{39} \leq L_X < 10^{49}$ erg s$^{-1}$) is nearly uniform, which is quite different with less luminous ones. Because GCs host relatively more bright sources than filed LMXBs (Kim et al. 2009; Peacock & Zepf 2016), we conclude the XLF slopes in the outer region of early-type galaxies are dominated by GC LMXBs (Irwin 2005). For late-type galaxies, the X-ray surface brightness significantly extends past the optical, suggesting strong effects from bright young populations.

### 5.4. Age and Luminosity Dependency of Luminous X-ray Sources

Kim & Fabbiano (2010) showed that young (< 5 Gyr) ellipticals host a larger fraction of luminous X-ray sources than old ellipticals. With the young and old elliptical samples (Section 5.1), we define the fraction ($F_{LX}$) of luminous X-ray sources (within the $D_{25}$ ellipse) following Kim & Fabbiano (2010),

$$F_{LX} = N(L_X > 5 \times 10^{38} \text{ erg s}^{-1})/N(L_X > 10^{38} \text{ erg s}^{-1}). \quad (1)$$

The luminous X-ray source fractions ($F_{LX}$) are 0.32±0.04 (68 out of 211) and 0.18±0.02 (199 out of 1085) for young and old ellipticals, respectively. Therefore, the number of luminous X-ray sources is higher by a factor of $\sim$ 1.8 in the young sample compared to the old sample, similar to that ($\sim$ 2) of Kim & Fabbiano (2010). In addition, no dependency of $F_{LX}$ on the stellar luminosity of the galaxy is found (Figure 18b), which is in agreement with Kim & Fabbiano (2010).

A further examination, about the radial distribution of X-ray sources in young and old ellipticals, is given in Figure 19. As shown in Brassington et al. (2008, 2009), the radial distribution of X-ray sources follows that of the optical light, especially for old ellipticals. No clear discrepancy is found for the young and old elliptical samples. Although young early-type galaxies contain more bright field LMXBs and flatter field-LMXB XLFs, there is no significant difference of the (GC-LMXB and field-LMXB) combined XLFs between young and old early-type galaxies (Lehmer et al. 2014).

### 5.5. Stellar Mass and SFR Indicators

Previous studies of nearby passive early-type galaxies and star-forming late-type galaxies have shown that the X-ray point-source emission from old LMXBs and younger HMXBs correlates well with galaxy stellar mass and SFR, respectively (Colbert et al. 2004). The total number of LMXBs and their combined luminosity are proportional to the stellar mass of the host galaxy, and the X-ray luminosity of a galaxy due to LMXBs can be used as an independent stellar mass indicator (Gilfanov 2004); on the other hand, the number of HMXBs and their collective luminosity scale with the SFR, therefore HMXBs are a good tracer of the recent star-formation activity in the host galaxy (Bauer et al. 2002; Grimm et al. 2003; Gilfanov et al. 2004a,b; Lehmer et al. 2008; Mineo et al. 2012, 2014b,c). This is explained by that at high X-ray energies (2–10 keV), the emission power from young stars and hot interstellar gas decreases steeply, while HMXBs start to dominate the galaxy-wide X-ray intensity and therefore correlate strongly with SFR (Persic & Rephaeli 2002; Persic et al. 2004; Persic & Rephaeli 2007; Ranalli et al. 2003; Lehmer et al. 2010).

Here we make a simple examination on the population of X-ray binaries and its relation to the stellar mass and SFR of the host galaxy. The masses of galaxies in our sample is collected from Tully (2015), which are calculated from the $K$-band luminosity with assumed light to mass conversion factor. Galaxies with detection thresholds below $10^{37}$ erg s$^{-1}$ are selected, and sources with luminosities $L_X > 10^{37}$ erg s$^{-1}$ are chosen following Gilfanov (2004). However, early-type galaxies typically have higher detection threshold/completeness limit, therefore few early-type galaxies are selected. Figure 20 displays the number of sources with luminosities $L_X > 10^{37}$ erg s$^{-1}$ and their collective X-ray luminosity versus stellar mass. A clear trend can be seen, but the distribution is more diffuse than that reported by Gilfanov (2004). This could be due to two reasons: (1) the masses of the inner part of galaxies (e.g., galaxy nucleus) are not excluded, while nuclear X-ray sources have been excluded; (2) more late-type galaxies are included in the sample, which contains a number of HMXBs and therefore causes some scatter. Figure 21 displays the number of sources with luminosities $L_X > 2 \times 10^{38}$ erg s$^{-1}$ and their collective X-ray luminosity versus SFR. Only galaxies with SFR above 0.2 $M_\odot$/yr are plotted. The trend is clear, but more diffuse than those from previous studies (e.g., Gilfanov et al. 2004a). These AGNs (e.g., LINERS, Seyfert galaxies) in our sample may partly contribute to the diffuse distribution (Ranalli et al. 2003; Lehmer et al. 2010).

### 5.6. ULXs in Elliptical Galaxies

This study, with its large number of galaxies and X-ray sources, also reveals some highly significant new results. The radial distribution of the ULXs detected in elliptical galaxies in this paper and previous studies (Liu & Mirabel 2005; Swartz et al. 2011) is presented in Figure 22. The ULXs have a wide distribution in galaxies, although more ULXs above $10^{39}$ erg s$^{-1}$ are detected between 0.7 $D_{25}$ and $D_{25}$ isophote. The normalized radial distribution (Figure 22b) shows a second peak located out of the 0.5 $D_{25}$ isophote, which may indicate a different population compared with the ULXs in the inner parts of galaxies.

Previous studies suggested that there are very few ULXs in early-type galaxies, e.g., $0.1 \pm 0.1$ ULXs per surveyed early-type galaxy in a *ROSAT* HRI survey of nearby galaxies (Liu et al. 2006), and most ULXs above $2 \times 10^{39}$ erg s$^{-1}$ in early-type galaxies are probably foreground or background objects not physically associated with the host galaxies (Irwin et al. 2004). Recently, Swartz et al. (2011) reported a ULX rate of 0.23 ULXs per elliptical galaxy, but only on a $2\sigma$ confidence level. This study, with the foreground/background objects and galactic nuclear sources carefully removed, finds a total of 49 ULXs above $2 \times 10^{39}$ erg s$^{-1}$ from the stitched survey of 130 early-type galaxies. Given 17.3 foreground/background objects predicted for the stitched survey of these galaxies, the ULX rate is $0.24 \pm 0.05$ per surveyed early-type galaxy, which is in good agreement with Swartz et al. (2011); this is five (4∼7) times lower than the rate for late-type galaxies, but nonetheless a $5\sigma$ non-zero result. There is still a significant population of ULXs above $4 \times 10^{39}$ erg s$^{-1}$, with 17 ULXs and 7.3 foreground/background objects, and a ULX rate of $0.07 \pm 0.03$ ULXs per surveyed early-type galaxy. Most of these ULXs reside in elliptical galaxies, which has a ULX rate 3-9 times higher than lenticular galaxies, consistent with a much steeper and lower XLF for lenticular galaxies as shown in Figure 12b. Given the old ages of the stellar populations in early-type galaxies, these ULXs must have rather old and low mass companions to their primary black holes, similar to the ULXs located in the bulges of early-type spirals (Swartz et al. 2009). Such systems have low accretion rates, and are most likely soft X-ray transients with small duty cycles for outbursts (King 2002).

An examination of the age dependency of ULXs is also performed using the young and old elliptical examples. The fraction ($F_{ULX}$) of ULXs (within the $D_{25}$ ellipse) is defined as,

$$F_{ULX} = N(L_X > 2 \times 10^{39} \text{ erg s}^{-1})/N(L_X > 10^{38} \text{ erg s}^{-1}). \quad (2)$$

Kim & Fabbiano (2010) showed that young (< 5 Gyr) elliptical galaxies hosts more (∼ 5 times) ULX type LMXBs ($L_X > 2 \times 10^{39}$ erg s$^{-1}$) than old (> 7 Gyr) elliptical galaxies. The ULX fractions ($F_{ULX}$) are 0.06±0.03 (3 out of 52) and 0.03±0.01 (19 out of 763) for young and old ellipticals, respectively. Compared to Kim & Fabbiano (2010), a weaker relation

is seen between $F_{ULX}$ and age (Figure 23a). Also, no dependency of $F_{ULX}$ on the stellar luminosity of the galaxy is found (Figure 23b).

### 5.7. ULX Classification from A New XLF Break

The multitude of ULXs from this survey has enabled detailed studies of XLFs at the high luminosity end. In a previous study of the X-ray point sources in nearby galaxies with *ROSAT*/HRI, the XLF in late-type galaxies is shown to be a smooth power-law with a break at $10^{40}$ erg s$^{-1}$ (Liu et al. 2006). Such a break was also present in a study of X-ray point sources in star forming galaxies (Grimm et al. 2003). This break, if real, suggests that ULXs below $10^{40}$ erg s$^{-1}$ belong to the same population of stellar mass black hole binaries, while the handful ULXs above $10^{40}$ erg s$^{-1}$ belong to another population of IMBHs with different binary formation mechanisms. However, this break may be an artifact caused by the scarcity of ULXs above $10^{40}$ erg s$^{-1}$ in these studies. Indeed, with 75 ULXs above $10^{40}$ erg s$^{-1}$ from this survey, the XLFs extend smoothly to $4 \times 10^{40}$ erg s$^{-1}$ without any breaks at $10^{40}$ erg s$^{-1}$ for the all-galaxy sample, the late-type galaxy sample, and the spiral-galaxy sample, confirming that the XLF break at $10^{40}$ erg s$^{-1}$ from previous studies are simply caused by small number of ULXs above $10^{40}$ erg s$^{-1}$. There is a break around $4 \times 10^{40}$ erg s$^{-1}$ in the new XLFs from this survey as shown in Figure 9a. Again, this break may be the dividing line between the population of the stellar mass black hole binaries and another population of IMBH binaries. Note that this break luminosity would correspond to massive stellar black holes (as massive as 30 $M_{\odot}$ as in the case of IC 10 X-1; Silverman & Filippenko 2008) with mildly super-Eddington radiation (King 2009), while the best IMBH candidate HLX-1 can have luminosities as low as a few $\times 10^{40}$ erg s$^{-1}$ (Farrell et al. 2009). This break may also be an artifact caused by the small number (three) of ULXs above $4 \times 10^{40}$ erg s$^{-1}$ in this survey. To test whether the break is real, we are carrying out another *Chandra*/ACIS survey of $\sim$ 1800 galaxies within 200 Mpc, the results of which will be reported in another paper.

## 6. SUMMARY

The properties of XLFs and the ULX populations are studied with uniform procedures for different galaxy samples in this work utilizing the recently finished *Chandra* ACIS survey of X-ray point sources in nearby galaxies. This study makes use of the largest sample of extragalactic X-ray point sources within 343 nearby galaxies, an order of magnitude increase in number as compared to other XLF and ULX studies. As an archive study, the observations

used were from different programs with different exposure times. However, all observations were reduced and analyzed with uniform procedures, and the detection threshold can be well quantified for X-ray sources with different OAAs and background levels as described in Section 2.1. The foreground stars and background AGN/QSOs projected into the nearby galaxies are seriously contaminating the samples of ordinary X-ray binaries in these galaxies, especially so for a large survey like this one. In this work, such contamination is meticulously estimated and removed with both the log$N$-log$S$ relations and the scaled source counts from the blank fields void of nearby galaxies. In addition, galactic nuclear sources are identified for the surveyed galaxies, and removed to construct clean samples of ordinary X-ray binaries.

With the surveyed galaxies, we have studied the XLFs and ULX properties across different host galaxy types, and confirm with good statistics that the XLF slope flattens from lenticular ($\alpha \sim 1.50 \pm 0.07$) to elliptical ($\sim 1.21 \pm 0.02$), to spirals ($\sim 0.80 \pm 0.02$) of S0/a-Sa ($\sim 0.98 \pm 0.03$), Sab-Sb ($\sim 0.78 \pm 0.03$), Sbc-Sc ($\sim 0.70 \pm 0.04$), Scd-Sd ($\sim 0.54 \pm 0.04$) to Sdm-Sm ($\sim 0.34 \pm 0.17$) subtypes, to peculiars ($\sim 0.55 \pm 0.30$), and to irregulars ($\sim 0.26 \pm 0.10$). The XLF break dividing the neutron star and black hole binaries is also confirmed, albeit at quite different break luminosities for different types of galaxies. The higher break luminosity than previous studies for early-type galaxies may be due to the presence of binaries with massive neutron stars or He-enriched neutron stars, since these systems could be existing in young early-type galaxies in our sample, while in previous studies, few young early-type galaxies were included. A radial dependency is found for ellipticals, with a flatter XLF slope for sources located between $D_{25}$ and $2D_{25}$. The radial distribution of luminous sources ($10^{39} \leq L_X < 10^{49}$ erg s$^{-1}$) shows different feature with fainter ones, further suggesting the XLF slopes in the out region of early-type galaxies are dominated by GC LMXBs. The age dependency is confirmed that young ($< 5$ Gyr) ellipticals host a larger fraction of luminous X-ray sources than old ellipticals, which is consistent with previous studies. The relations between the X-ray population and galaxy stellar mass and SFR are also confirmed, although they are more diffuse than those from previous studies.

This study shows that the ULX rate in early-type galaxies is $0.24 \pm 0.05$ ULXs per surveyed galaxy, a $5\sigma$ non-zero result, confirming the existence of ULXs in early-type galaxies. With a large number of ULXs in this survey, the XLF break at $10^{40}$ erg s$^{-1}$ seen in previous studies is proved to be an artifact caused by small number statistics. It is found that the XLF for late-type galaxies extends smoothly until it drops abruptly around $4 \times 10^{40}$ erg s$^{-1}$. If this break at $4 \times 10^{40}$ erg s$^{-1}$ is real and not due to low number statistics, it will suggest that ULXs below $4 \times 10^{40}$ erg s$^{-1}$ belong to the stellar black hole population possibly including 30 $M_\odot$ black holes with mildly super-Eddington radiation, while the handful ULXs above $4 \times 10^{40}$ erg s$^{-1}$ belong to another population of IMBHs with different binary formation mechanisms.

We especially thank the anonymous referee for his/her thorough report and helpful comments and suggestions that have significantly improved the paper. This research has made use of data obtained from the *Chandra* Data Archive. The authors acknowledge support from the National Science Foundation of China under grants NSFC-11273028 and NSFC-11333004, and support from the National Astronomical Observatories, Chinese Academy of Sciences under the Young Researcher Grant.

## REFERENCES

Annibali, F., Bressan, A., Rampazzo, R., Zeilinger, W. W., & Danese, L. 2007, A&A, 463, 455

Bauer, F. E., Alexander, D. M., Brandt, W. N., et al. 2002, AJ, 124, 2351

Bell, E., & De Jong, R., 2001, ApJ, 550, 212

Bildsten, L., & Deloye, C. J. 2004, ApJ, 607, L119

Brassington, N. J., Fabbiano, G., Kim, D.-W., et al. 2008, ApJS, 179, 142

Brassington, N. J., Fabbiano, G., Kim, D.-W., et al. 2009, ApJS, 181, 605

Colbert, E. J. M., Heckman, T. M., Ptak, A. F., Strickland, D. K., & Weaver, K. A. 2004, ApJ, 602, 231

de Vaucouleurs, G., de Vaucouleurs, A., Corwin, H., et al. 1991, *Third Reference Catalogue of Bright Galaxies* Vol. I, Vol. II, Vol. III (New York: Springer)

Evans, I. N., Primini, F. A., Glotfelty, K. J., et al. 2010, ApJS, 189, 37-82

Fabbiano, G. 1989, ARA&A, 27, 87

Fabbiano, G. 2005, Science, 307, 533

Fabbiano, G. 2006, ARA&A, 44, 323

Fabbiano, G., & White, N. E. 2006, in Compact Stellar X-ray Sources in Normal Galaxies, ed. W. H. G. Lewin, & M. van der Klis (Cambridge: Cambridge Univ. Press), 475

Fabbiano, G., Zezas, A., & Murray, S. S. 2001, ApJ, 554, 1035

Farrell, S., Webb, N., Barret, D., et al. 2009, Nature, 460, 73

Fragos, T., Kalogera, V., Belczynski, K., et al. 2008, ApJ, 683, 346-356

Freedman, W. L., Hughes, S. M., Madore, B. F., et al. 1994, ApJ, 427, 628

Giacconi, R., Rosati, P., Tozzi, P., et al. 2001, ApJ, 551, 624

Gilfanov, M. 2004, MNRAS, 349, 146

Gilfanov, M., Grimm, H.-J., & Sunyaev, R. 2004, MNRAS, 347, L57

Gilfanov, M., Grimm, H.-J., & Sunyaev, R. 2004, Nuclear Physics B Proceedings Supplements, 132, 369

Gilfanov, M., Grimm, H.-J., & Sunyaev, R. 2004, MNRAS, 351, 1365

Graham, A., 2001, AJ, 121, 820

Grimm, H.-J., Gilfanov, M., & Sunyaev, R. 2002, A&A, 391, 923

Grimm, H.-J., Gilfanov, M., & Sunyaev, R. 2003, MNRAS, 339, 793

Hasinger, G., Burg, R., Giacconi, R., et al. 1993, A&A, 275, 1

Heger, A., & Woosley, S. E. 2002, ApJ, 567, 532

Humphrey, P. J., & Buote, D. A. 2008, ApJ, 689, 983-1004

Irwin, J. A. 2005, ApJ, 631, 511

Irwin, J., Bregman, J., & Athey, A. 2004, ApJ, 601, 143

Ivanova, N., & Kalogera, V. 2006, ApJ, 636, 985

Jarrett, T. H., Chester, T., Cutri, R., Schneider, S. E., & Huchra, J. P. 2003, AJ, 125, 525

Jeltema, T. E., Canizares, C. R., Buote, D. A., & Garmire, G. P. 2003, ApJ, 585, 756

Kilgard, R., Kaaret, P., Krauss, M., et al. 2002, ApJ, 573, 138

Kim, D.-W., Cameron, R., Drake, J., et al. 2004, ApJS, 150, 19

Kim, D.-W., & Fabbiano, G. 2003, ApJ, 586, 826

Kim, D.-W., & Fabbiano, G. 2004, ApJ, 611, 846

Kim, D.-W., & Fabbiano, G. 2010, ApJ, 721, 1523

Kim, D.-W., Fabbiano, G., Brassington, N. J., et al. 2009, ApJ, 703, 829

Kim, D.-W., Fabbiano, G., Kalogera, V., et al. 2006, ApJ, 652, 1090

King, A. R. 2002, MNRAS, 335, L13

King, A. R. 2004, MNRAS, 347, L18

King, A. R. 2009, MNRAS, 393, L41

King, A. R., Davies, M. B., Ward, M. J., Fabbiano, G., & Elvis, M. 2001, ApJ, 552, L109

Kong, A., Di Stefano, R., Garcia, M., & Greiner, J., 2003, ApJ, 585, 298

Kundu, A., Maccarone, T. J., & Zepf, S. E. 2007, ApJ, 662, 525

Lehmer, B. D., Alexander, D. M., Bauer, F. E., et al. 2010, ApJ, 724, 559

Lehmer, B. D., Berkeley, M., Zezas, A., et al. 2014, ApJ, 789, 52

Lehmer, B. D., Brandt, W. N., Alexander, D. M., et al. 2008, ApJ, 681, 1163-1182

Liu, J. 2011, ApJS, 192, 10

Liu, J., Bregman, J., & Irwin, J. 2006, ApJ, 642, 171

Liu, Q. Z., & Mirabel, I. F. 2005, A&A, 429, 1125

Long, K. S., & van Speybroeck, L. P. 1983, Accretion-Driven Stellar X-ray Sources, ed. W. H. G. Lewin & E. P. J. van den Heuvel (Cambridge: Cambridge Univ. Press), 117

Makishima, K., Kubota, A., Mizuno, T., et al. 2000, ApJ, 535, 632

McDonald, M., Courteau, S., Tully, R. B., & Roediger, J. 2011, MNRAS, 414, 2055

Miller, M. C., & Colbert, E. 2004, IJMPD, 13, 1

Mineo, S., Fabbiano, G., D'Abrusco, R., et al. 2014, ApJ, 780, 132

Mineo, S., Gilfanov, M., Lehmer, B. D., Morrison, G. E., & Sunyaev, R. 2014, MNRAS, 437, 1698

Mineo, S., Gilfanov, M., & Sunyaev, R. 2012, MNRAS, 419, 2095

Mineo, S., Rappaport, S., Levine, A., et al. 2014, ApJ, 797, 91

Mineo, S., Rappaport, S., Steinhorn, B., et al. 2013, ApJ, 771, 133

Mushotzky, R., Cowie, L., Barger, A., & Arnaud, K. 2000, Nature, 404, 459

Paolillo, M., Puzia, T. H., Goudfrooij, P., et al. 2011, ApJ, 736, 90

Peacock, M. B., & Zepf, S. E. 2016, ApJ, 818, 33

Persic, M., & Rephaeli, Y. 2002, A&A, 382, 843

Persic, M., & Rephaeli, Y. 2007, A&A, 463, 481

Persic, M., Rephaeli, Y., Braito, V., et al. 2004, A&A, 419, 849

Podsiadlowski, P., Rappaport, S., & Pfahl, E. D. 2002, ApJ, 565, 1107

Postnov, K. A., & Kuranov, A. G. 2005, Astronomy Letters, 31, 7

Primini, F. A., Houck, J. C., Davis, J. E., et al. 2011, ApJS, 194, 37

Ranalli, P., Comastri, A., & Setti, G. 2003, A&A, 399, 39

Rice, W., Lonsdale, C, Soifer, B., et al. 1988, ApJS, 68, 91

Roberts, T. P., & Warwick, R. S. 2000, MNRAS, 315, 98

Rosa-González, D., Terlevich, E., & Terlevich, R., 2002, MNRAS, 332, 283

Sánchez-Blázquez, P., Gorgas, J., Cardiel, N., & González, J. J. 2006, A&A, 457, 809

Sarazin, C. L., Irwin, J. A., & Bregman, J. N. 2000, ApJ, 544, L101

Sarazin, C. L., Irwin, J. A., & Bregman, J. N. 2001, ApJ, 556, 533

Sarazin, C. L., Kundu, A., Irwin, J. A., et al. 2003, ApJ, 595, 743

Sell, P., Pooley, D., Zezas, A., et al. 2011, ApJ, 735, 26

Silverman, J., & Filippenko, A. 2008, ApJ, 678, 17

Swartz, D., Soria, R., & Tennant, A. 2008, ApJ, 684, 282

Swartz, D. A., Soria, R., Tennant, A. F., & Yukita, M. 2011, ApJ, 741, 49

Swartz, D. A., Tennant, A. F., & Soria, R. 2009, ApJ, 703, 159

Terlevich, A. I., & Forbes, D. A. 2002, MNRAS, 330, 547

Thomas, D., Maraston, C., Bender, R., & Mendes de Oliveira, C. 2005, ApJ, 621, 673

Trager, S. C., Faber, S. M., Worthey, G., & González, J. J. 2000, AJ, 120, 165

Tully, R. B. 2015, AJ, 149, 171

Voss, R., Gilfanov, M., Sivakoff, G. R., et al. 2009, ApJ, 701, 471

Zezas, A., & Fabbiano, G. 2002, ApJ, 577, 726

Zezas, A. L., Georgantopoulos, I., & Ward, M. J. 1999, MNRAS, 308, 302

## A. LIGHT PROFILES OF SURVEYED GALAXIES

The light profile for a galaxy is computed from the total blue light $\pounds_B$ and the effective radius $R_e$ that encloses 50% of the total light. The effective radii are taken from RC3 for two thirds of the survey galaxies, with an average $R_e$ of $0.15D_{25}$, while for the rest galaxies without $R_e$ from RC3, the $R_e$ is assumed as $0.15D_{25}$. The blue magnitudes of these survey galaxies are drawn from the RC3 catalog, and converted to blue light $\pounds_B$ in unit of $L_\odot$ with $M_{B\odot} = 5.46$ mag (Liu et al. 2006).

The light profiles are expressed by different forms for early-type galaxies and late-type galaxies. For the former one, it is usually described by the de Vaucouleurs $R^{1/4}$ law, $I(R) = I_e 10^{3.33-3.33(R/R_e)^{1/4}}$, with $R$ as the elliptical radius and $I_e$ as the surface brightness at the effective radius $R_e$. The light profile can therefore be computed as $I(R) = \frac{\pounds_B}{7.22\pi R_e^2} 10^{3.33-3.33(R/R_e)^{1/4}}$, with the total light expressed as $\pounds_B = 7.22\pi R_e^2 I_e$. For the latter one, the light profile can be decomposed into a de Vaucouleurs bulge in the form of $I(R) = I_e 10^{3.33-3.33(R/r_e)^{1/4}}$, and an exponential disk in the form of $I(R) = I_0 e^{-R/h}$, where $h$ is the scale height, and $I_0$ is the surface brightness at the galactic center. The total light of the disk can be expressed as $2\pi h^2 I_0$. The relative prominence of the two components, which changes with the Hubble type T and the bulge-to-disk ($B/D$) ratios, is taken from Graham (2001) and interpolated if necessary. In general, the relative prominence decreases toward later galaxy types (from 25% at T=0 to 1% at T=10). The $r_e/h$ ratio is quite constant despite the variation in bulge-to-disk ratios, and it is adopted as 0.2 following Graham (2001). With the assumption that the effective radius $R_e$ from RC3 encloses 50% of the disk light, we find $h = R_e/1.7$, $r_e = R_e/8.5$. This is reasonable for most surveyed galaxies with $B/D \ll 1$, while for galaxies with nonnegligible bulges, the $r_e$ and $h$ may be slightly overestimated. The $I_0$ and $I_e$ can be computed from $\pounds_B$ and $R_e$, with $I_0 = \frac{\pounds_B}{1+B/D} \frac{1.7^2}{2\pi R_e^2}$, and

This preprint was prepared with the AAS LaTeX macros v5.2.

$I_e = \frac{\pounds_B}{D/B+1} \frac{8.5^2}{7.22\pi R_e^2}$. Finally, the light profile for late-type galaxies can be calculated with $I(R) = I_e 10^{3.33-3.33(R/r_e)^{1/4}} + I_0 e^{-R/h}$.

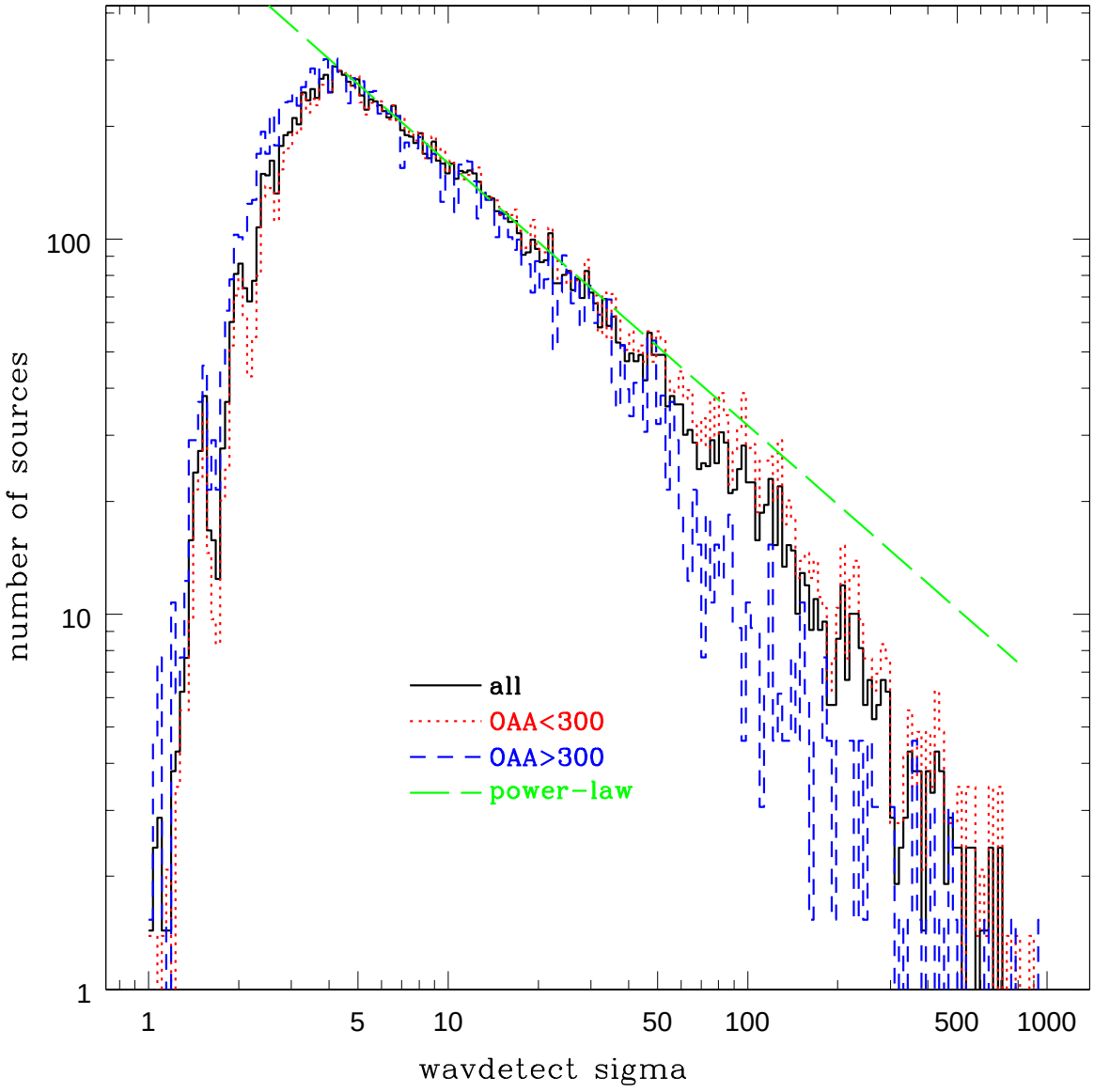



Fig. 1.— Distribution of detection significance for all sources detected in 626 ACIS observations. As the detection significance decreases, the source number increases in a power-law form till $\sigma \approx 4$, from where on the source number drops sharply from the expected power-law form. The detected number is about 55% at $3\sigma$ and 15% at $2\sigma$ of that from the expected power-law.

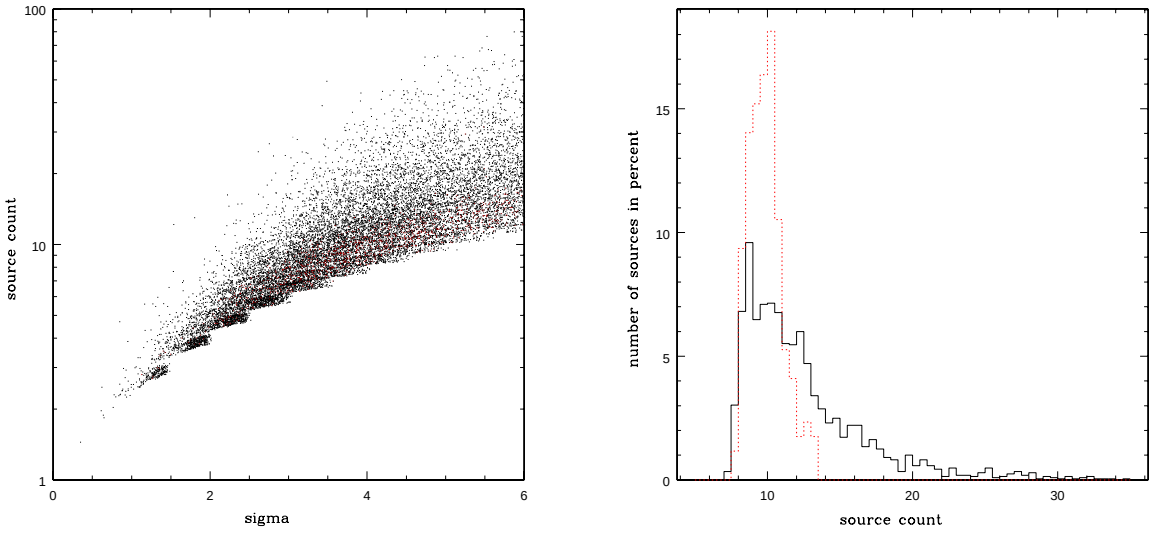



Fig. 2.— (a) Source counts versus detection significance for all sources (black dots) and for a subset of sources with OAA $\leq 2'$ and background level between 0.01 and 0.03 count pixel$^{-1}$ (red dots). (b) The source count histograms for sources with detection significance $3.8 \leq \sigma \leq 4.2$ (solid black) and for its subset with OAA $\leq 2'$ and background level between 0.01 and 0.03 count pixel$^{-1}$ (dotted red).

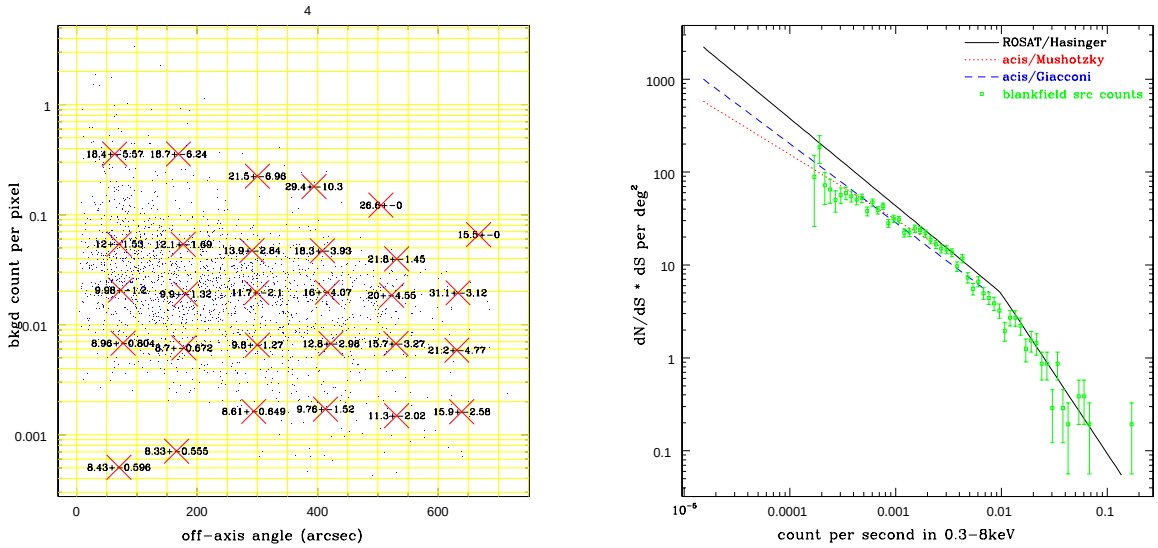



Fig. 3.— The detection thresholds for $4\sigma$ for different combinations of OAAs and background levels. The numbers are the detection thresholds and errors computed by averaging the detected sources with $3.8 \leq \sigma \leq 4.2$ (blue dots) around the red crosses.

Fig. 4.— The numbers of foreground/background sources per deg$^2$ versus equivalent ACIS-S3 count rates expected from the log$N$-log$S$ relations derived by Hasinger et al. (1993), Mushotzky et al. (2000), and Giacconi et al. (2001). Overplotted are the detected sources outside $2D_{25}$ isophotes of all galaxies as a direct foreground/background estimate for our survey.

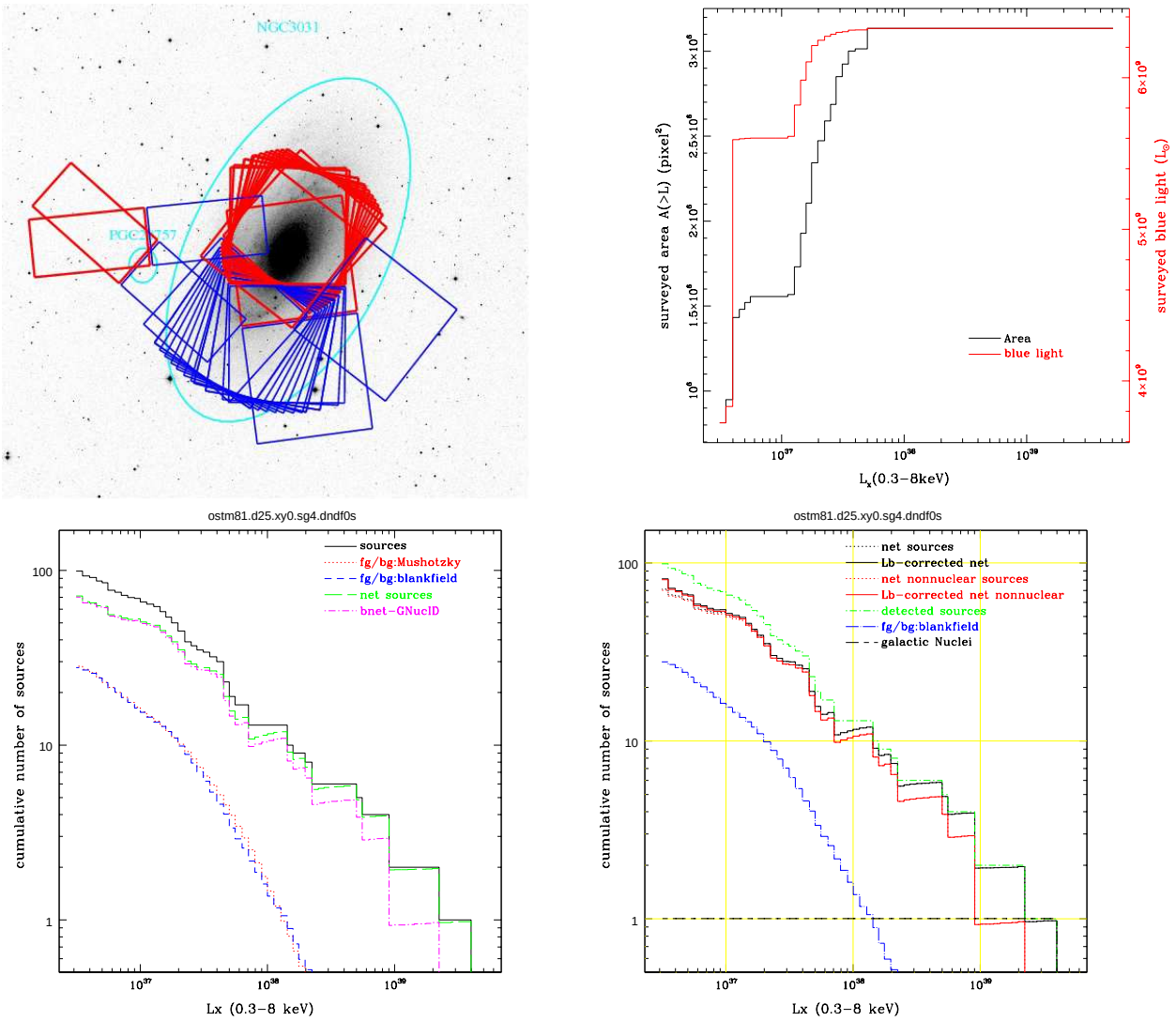



Fig. 5.— (a) DSS image for NGC 3031 (M81) with the fields of view for 19 ACIS observations overlayed. The red/blue squares are for S3/S2 chips, and the cyan ellipses denote the isophotes for NGC 3031 and PGC 23757 (Holmberg IX). (b) The surveyed sky area curve $A(>L)$ (black solid) and the surveyed blue light curve $\pounds_B(>L)$ for the stitched deep survey out of 19 ACIS observations. (c) The cumulative curves for detected sources above $4\sigma$ (black solid), for expected background/foreground objects based on the Mushotzky et al. (2000) log$N$-log$S$ relation (red dotted) and based on the source counts in blank fields (blue dashed), for "net" sources (green long-dashed), and for "net" non-nuclear sources (purple dot-dashed). (d) The cumulative curve for "net" sources in comparison to the $\pounds_b$-corrected "net" sources.

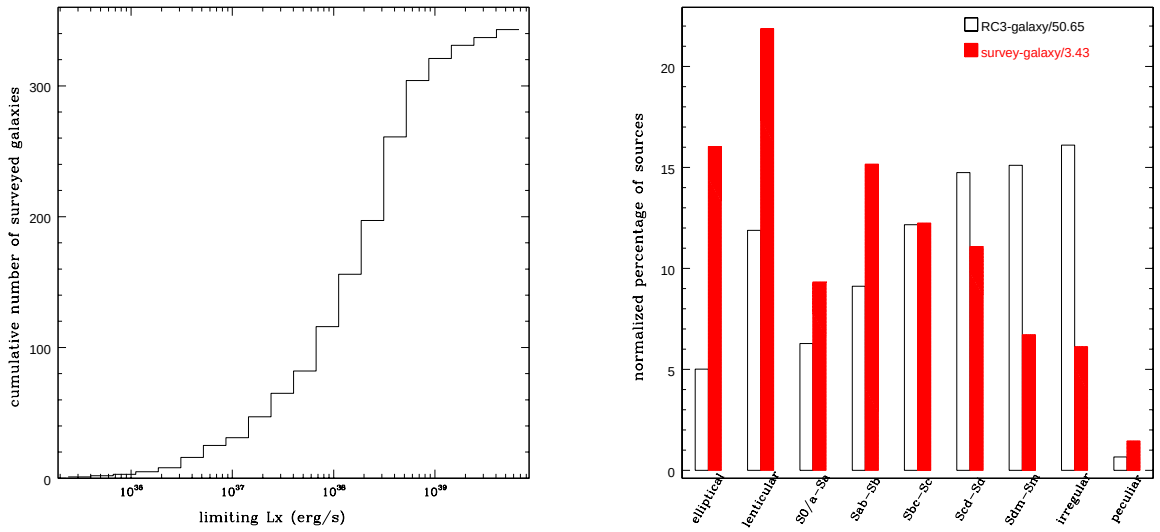



Fig. 6.— (a) Histogram for the limiting $L_X$ of 343 surveyed galaxies. (b) The galaxy type distribution of 343 surveyed galaxies in comparison to the RC3 galaxies within 40Mpc.

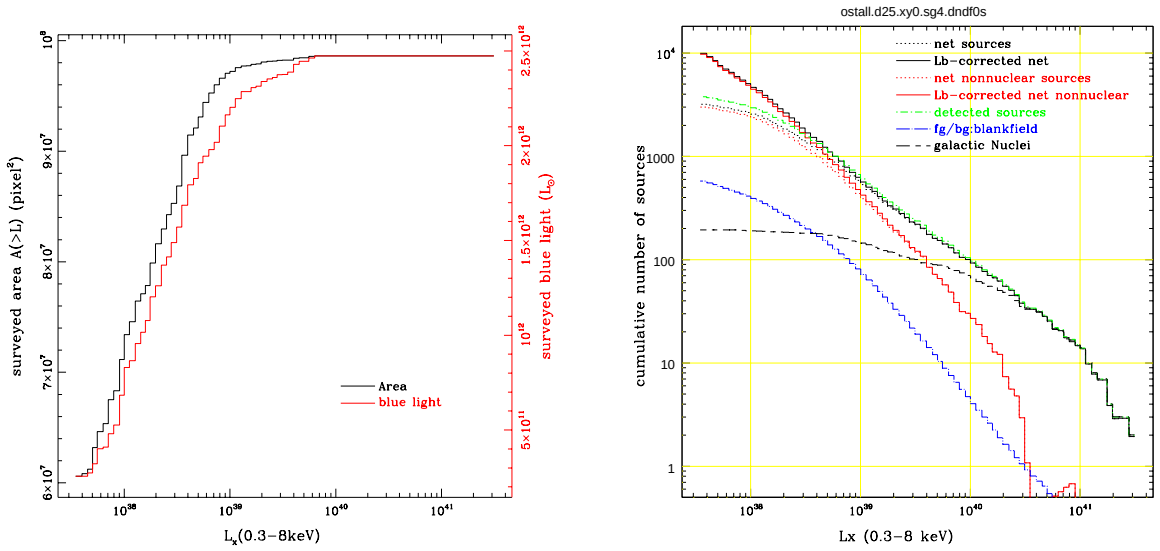



Fig. 7.— (a) The surveyed sky area curve $A(> L)$ (black solid) and the surveyed blue light curve $\pounds_B(> L)$ for the stitched deep survey of all 343 galaxies. (b) Cumulative histograms for the numbers of the detected sources, the estimated background/foreground objects, the ($\pounds_B$-corrected) net sources, the identified galactic nuclei, and the ($\pounds_B$-corrected) net nonnuclear sources.

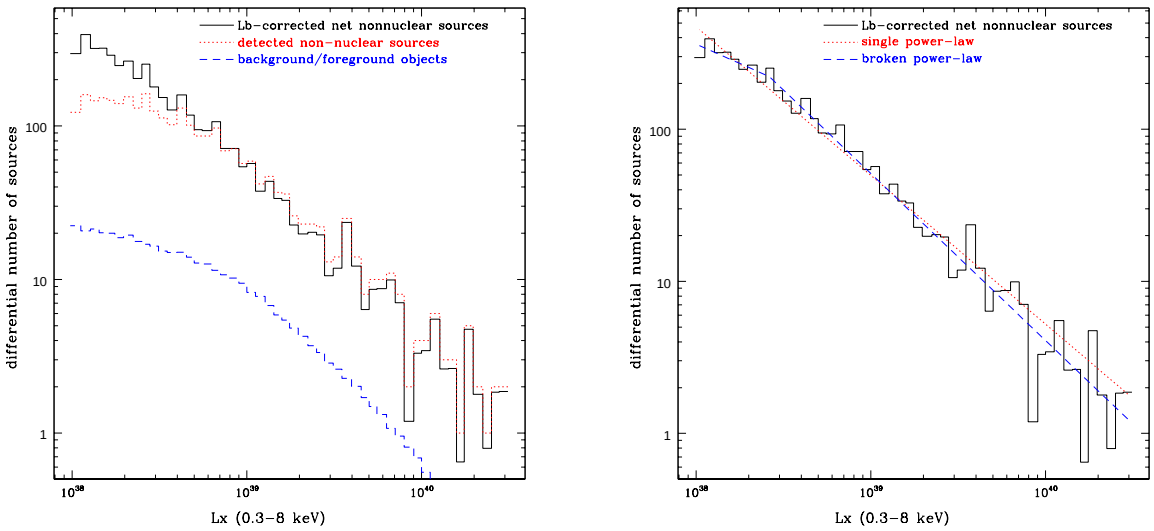



Fig. 8.— (a) The differential curves for the numbers of detected non-nuclear sources, predicted background/foreground objects, and the $\pounds_B$-corrected net nonnuclear sources for the total survey of 343 galaxies. (b) The differential curve for the $\pounds_B$-corrected net nonnuclear sources, the single power-law fit, and the broken power-law fit.

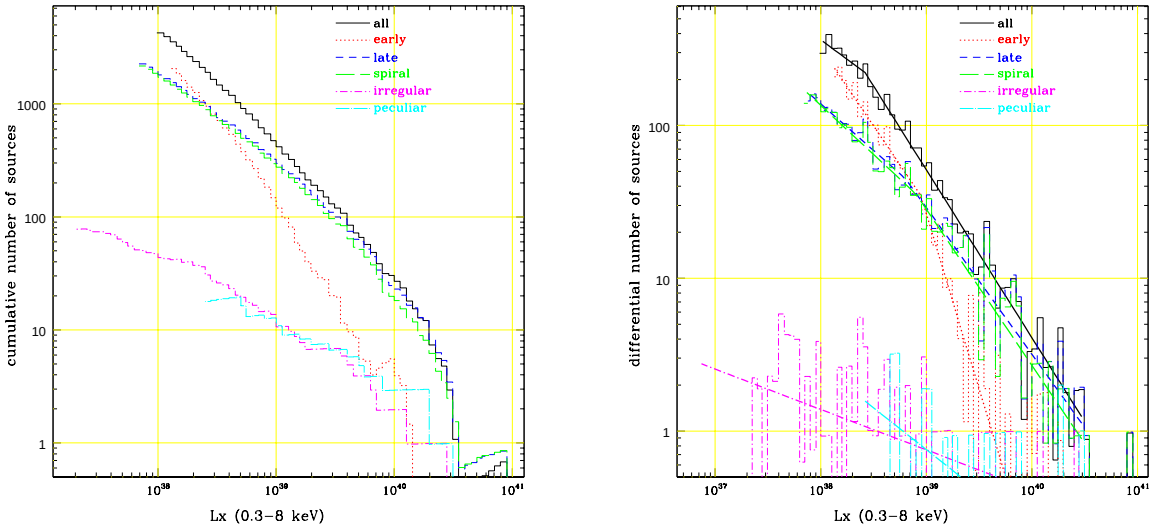



Fig. 9.— (a) the cumulative curves for the $\pounds_B$-corrected net nonnuclear sources for samples of early-type galaxies, late-type galaxies, spiral galaxies, irregular galaxies and peculiar galaxies. The curves are all above the luminosity at which $\pounds_B$ is 50% of the total surveyed blue light for the sample. (b) The differential curves and the best-fit XLF models for the $\pounds_B$-corrected net nonnuclear sources. It is obvious that the XLF is much steeper for early-type galaxies than for late-type galaxies.

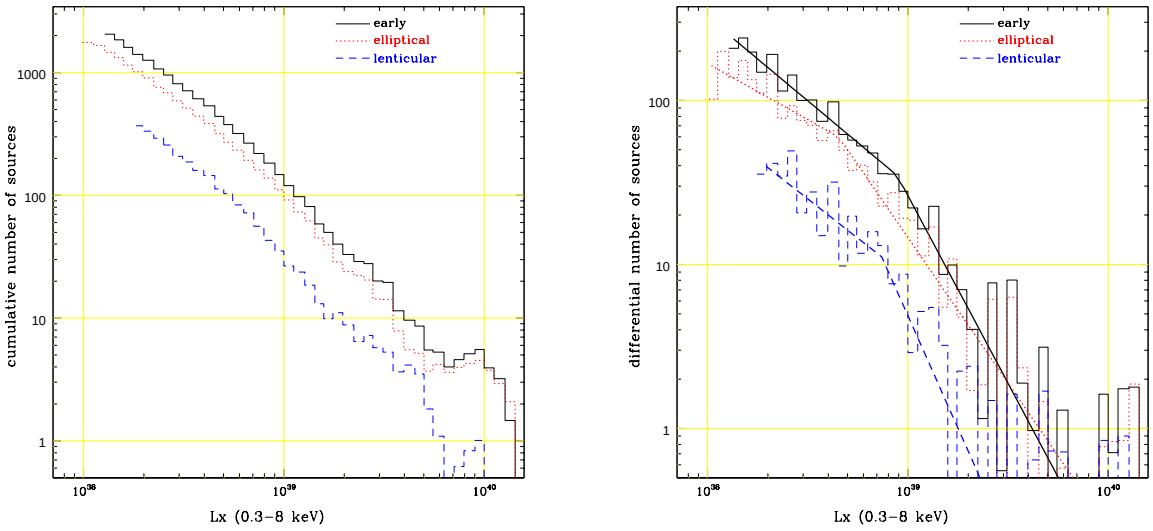



Fig. 10.— (a) the cumulative curves for the $\pounds_B$-corrected net nonnuclear sources for samples of early-type galaxies, elliptical galaxies and lenticular galaxies. (b) The differential curves and the best-fit XLF models for the $\pounds_B$-corrected net nonnuclear sources.

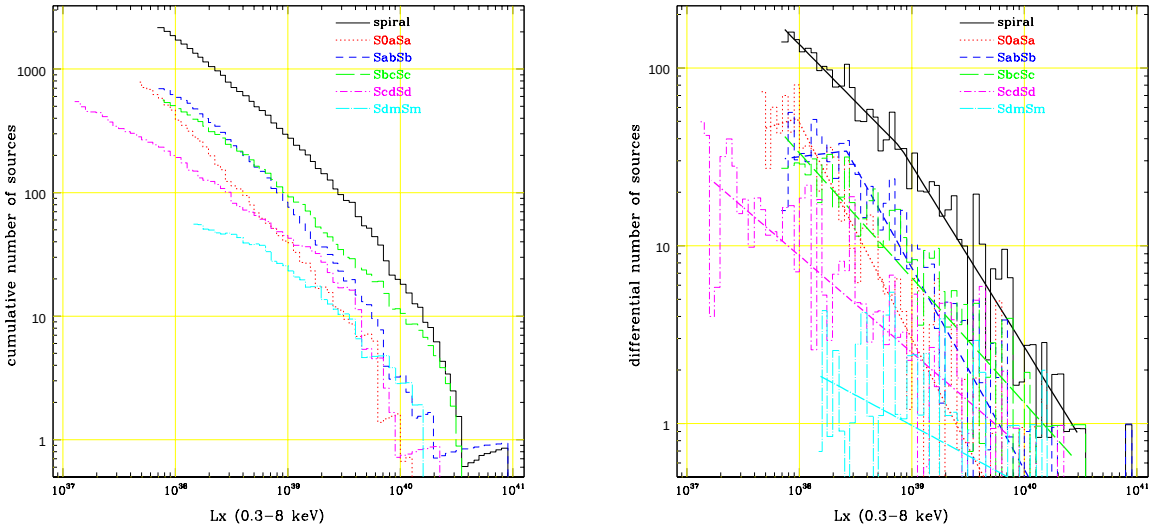



Fig. 11.— (a) the cumulative curves for the $\pounds_B$-corrected net nonnuclear sources for samples of spiral and subtype galaxies. (b) The differential curves and the best-fit XLF models for the $\pounds_B$-corrected net nonnuclear sources.

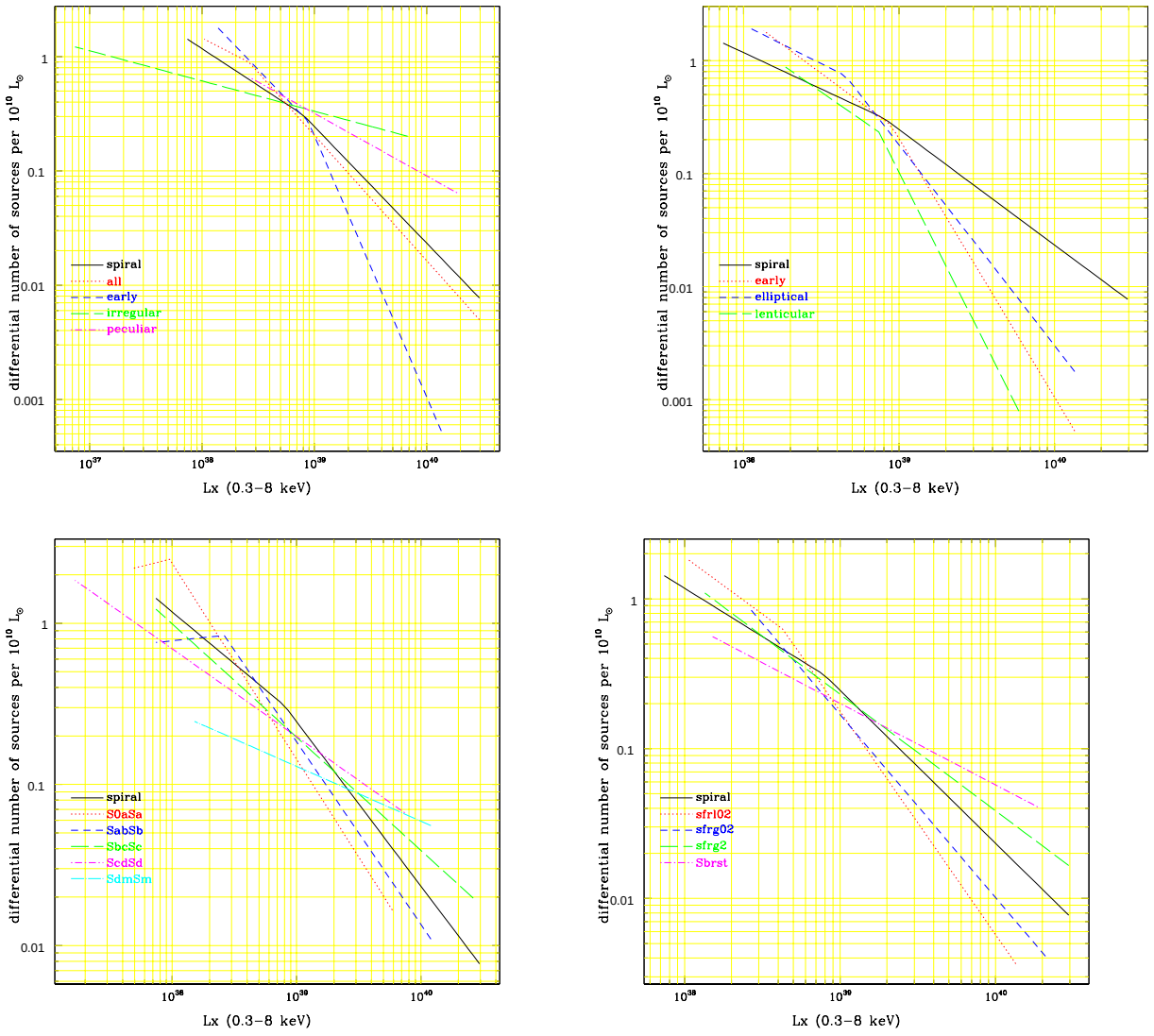



Fig. 12.— The $\mathcal{L}_B$ normalized power-law fits to the net nonnuclear sources in different galaxy samples. (a) Fits for all, early, spiral, peculiar, and irregular galaxies. (b) Fits for early and subtype galaxies. (c) Fits for spiral and subtype galaxies. (d) Fits for spiral, starburst galaxies and galaxies with different SFRs. The same black solid line is used for the power-law fit for spiral in all four panels.

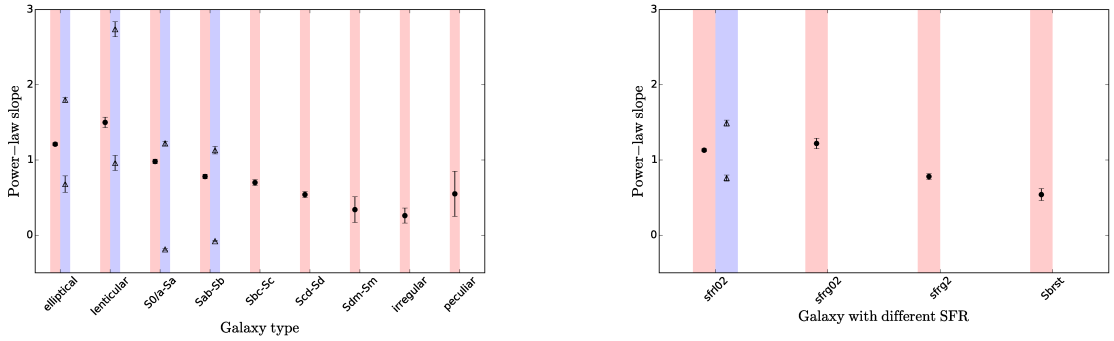



Fig. 13.— (a) The fitted XLF slopes for galaxies with different types. The solid circles in the red bar shows the results from single power fits, while the open triangles in the blue bar shows the results from broken power fits. It is obvious that the XLF slopes become flatter from early-type to late-type galaxies. (b) The fitted XLF slopes for galaxies with different SFRs. The solid circles in the red bar shows the results from single power fits, while the open triangles in the blue bar shows the results from broken power fits. It also shows the flatting trend of the XLF slopes with increasing SFRs.

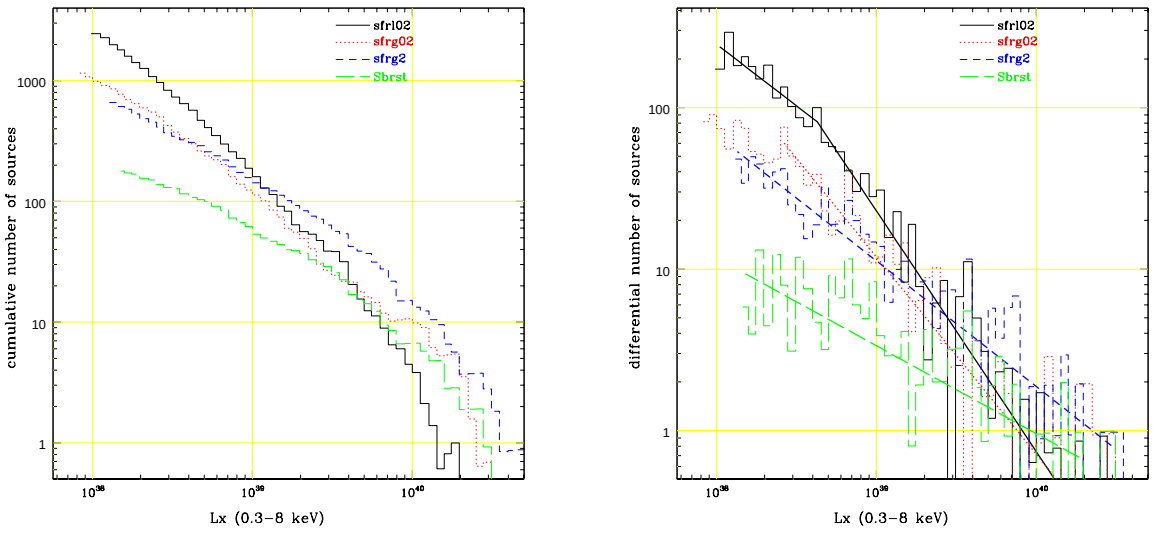



Fig. 14.— (a) The cumulative curves for the $\pounds_B$-corrected net nonnuclear sources for galaxies with different SFRs. (b) The differential curves and the best-fit XLF models for the $\pounds_B$-corrected net nonnuclear sources.

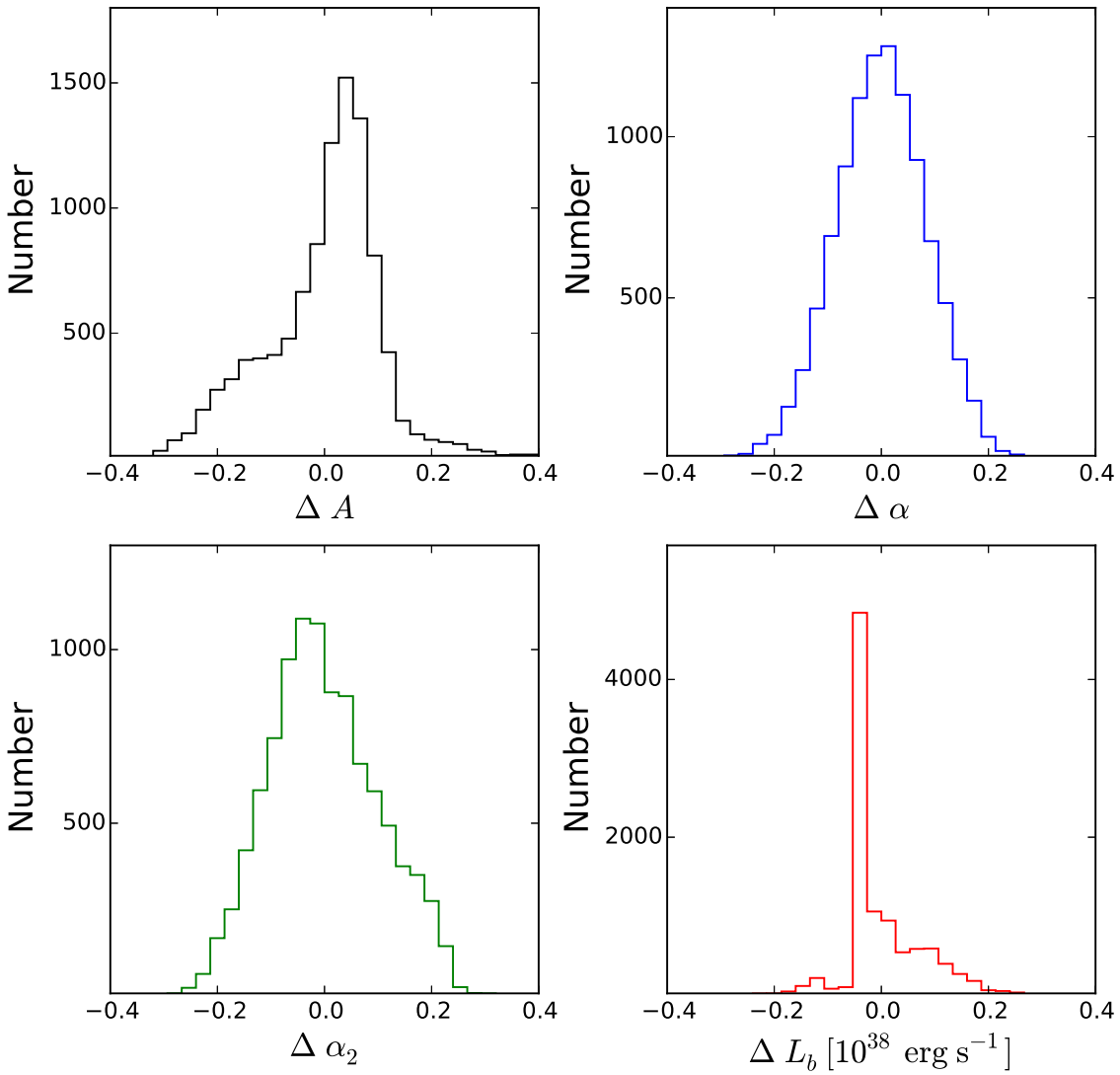



Fig. 15.— The distribution of the fitting parameters ($A$, $\alpha$, $\alpha_2$ and $L_b$) compared to the results in this paper. The simulation ($10^4$ runs) is performed for early-type galaxies and the composite XLF is fitted with a broken power law.

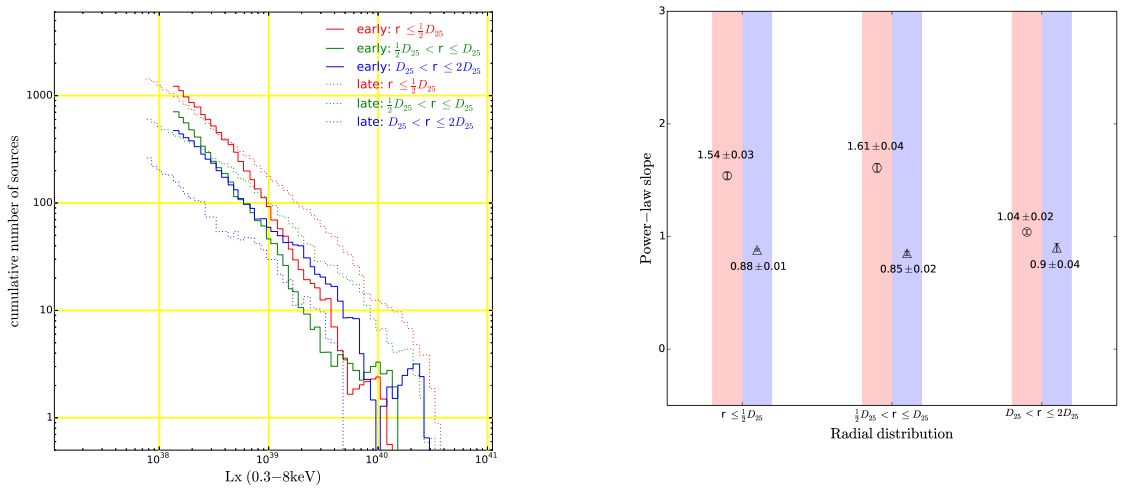



Fig. 16.— (a) The cumulative curves for sources in various parts of early-type and late-type galaxies. (b) The fitted XLF slopes for sources in various parts of early-type (circles) and late-type galaxies (triangles). It seems that the XLF slopes of late-type galaxies are similar for different parts of galaxies, while the XLF slopes of early-type galaxies become flatter for sources between $D_{25}$ and $2D_{25}$ isophote.

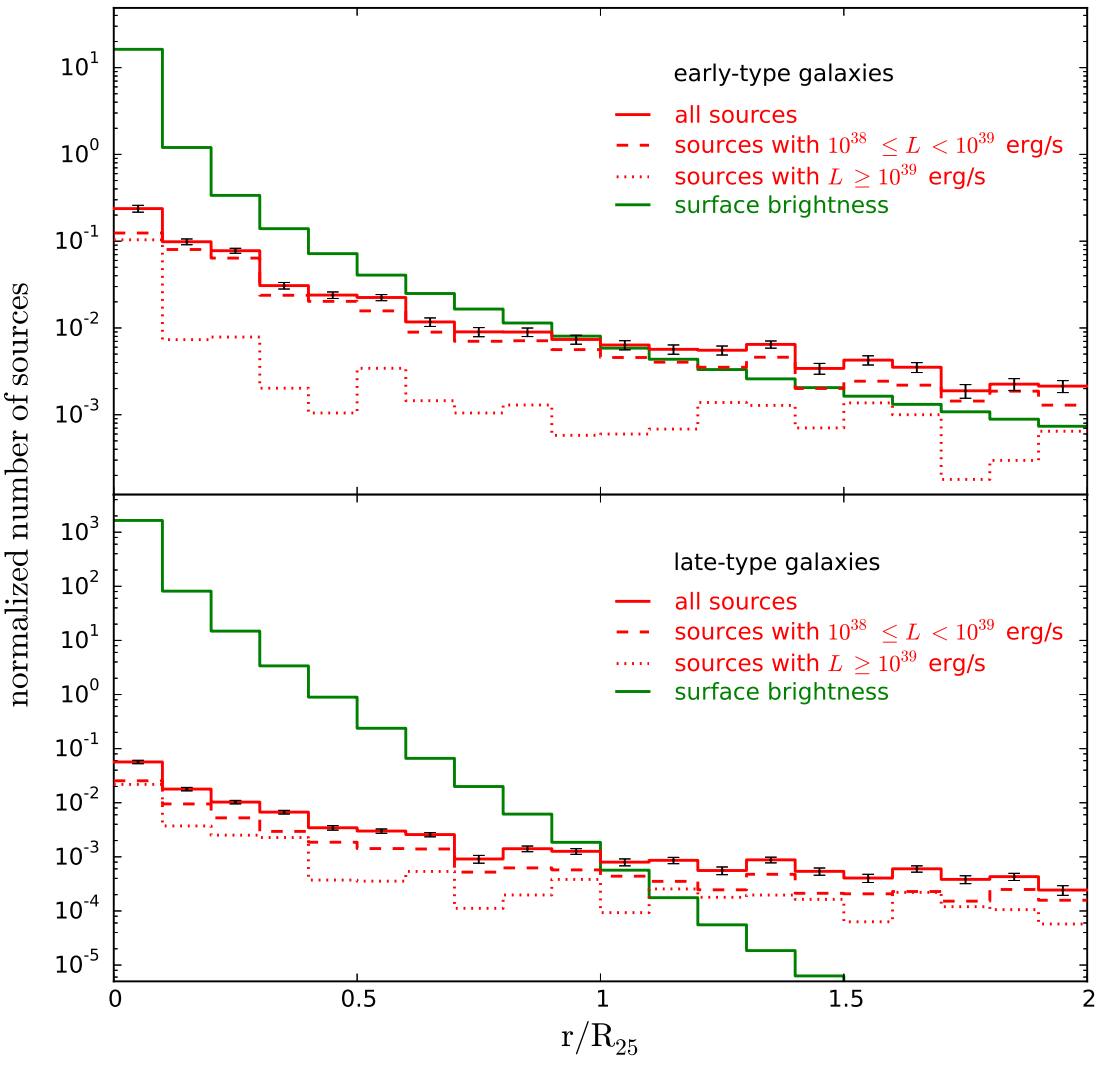



Fig. 17.— The radial distribution of normalized number of sources for early-type and late-type galaxies. The green line reprensents the radial distribution of B-band surface brightness, while the red lines represent the radial distribution of normalized number of X-ray sources.

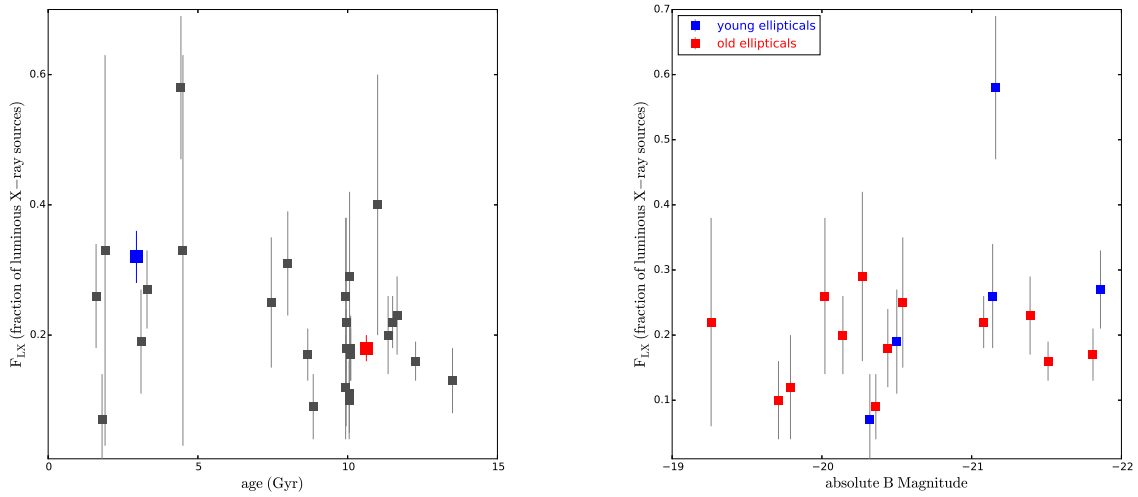



Fig. 18.— Fraction ($F_{LX}$) of luminous ($L_X > 5 \times 10^{38}$ erg s$^{-1}$) X-ray sources against age and absolute $B$-band magnitude. The number of luminous X-ray sources is higher by a factor of $\sim 1.8$ in the young sample compared to the old sample, while no dependency of $F_{LX}$ on the stellar luminosity of the galaxy is found.

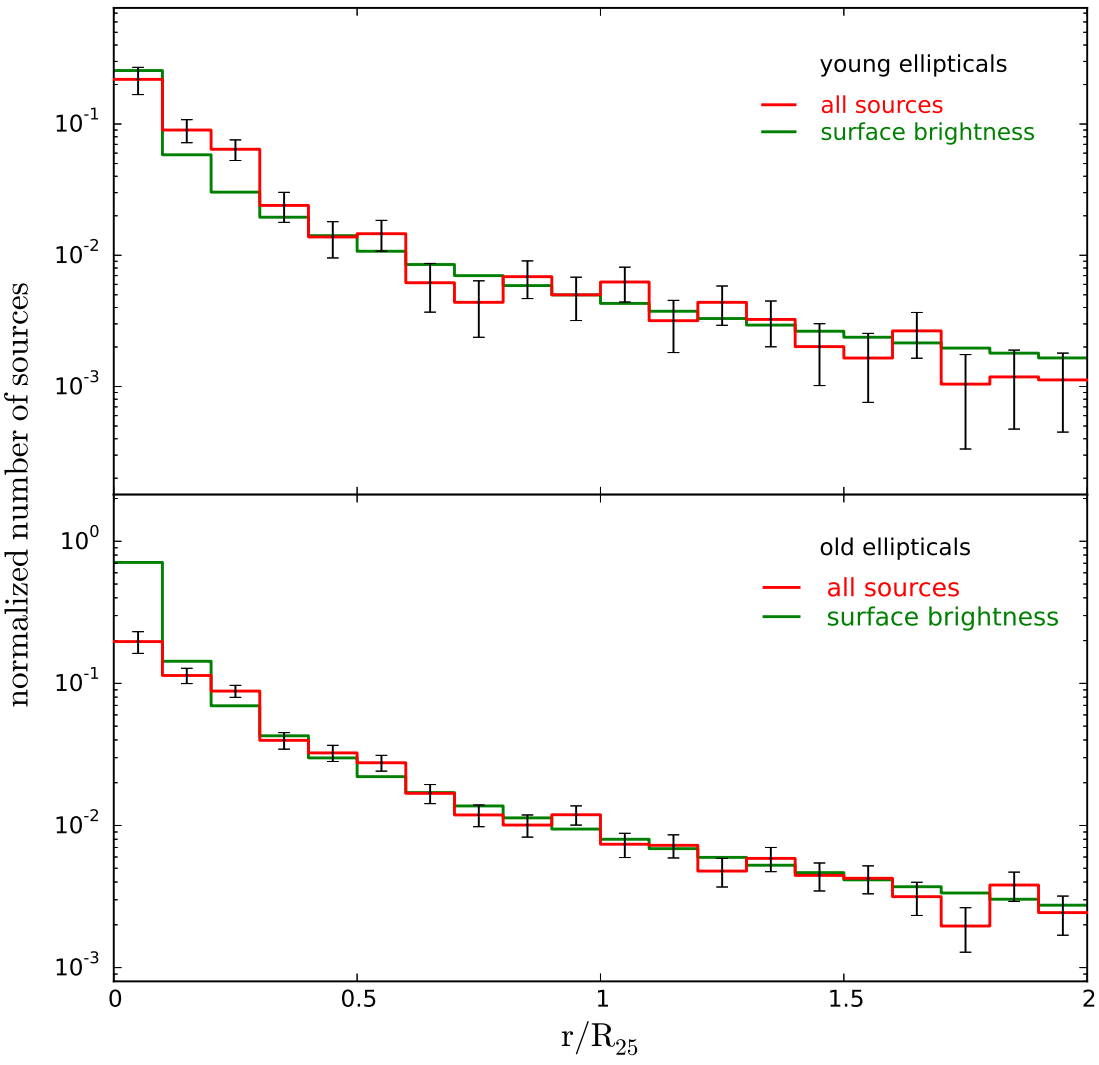



Fig. 19.— The radial distribution of normalized number of sources for young and old elliptical galaxies. The green line reprensents the radial distribution of B-band surface brightness, while the red line represents the radial distribution of normalized number of X-ray sources.

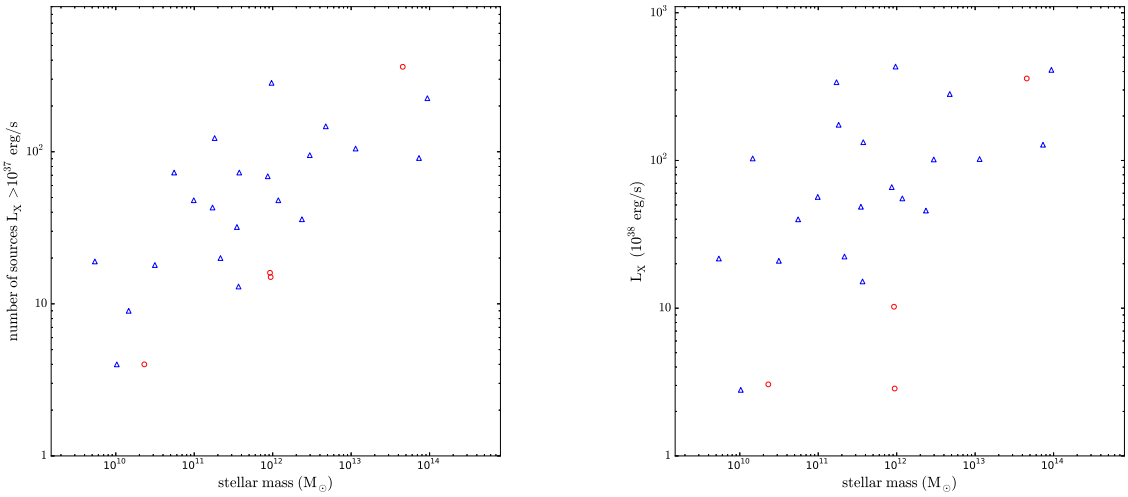



Fig. 20.— (a) Number of sources with luminosities $L_X > 10^{37}$ erg s$^{-1}$ versus stellar mass. The data for galaxies are shown by circles and triangles for early- and late-type galaxies respectively. (b) The collective X-ray luminosity verse stellar mass. A clear trend can be seen, but the distribution is more diffuse than that reported by Gilfanov (2004).

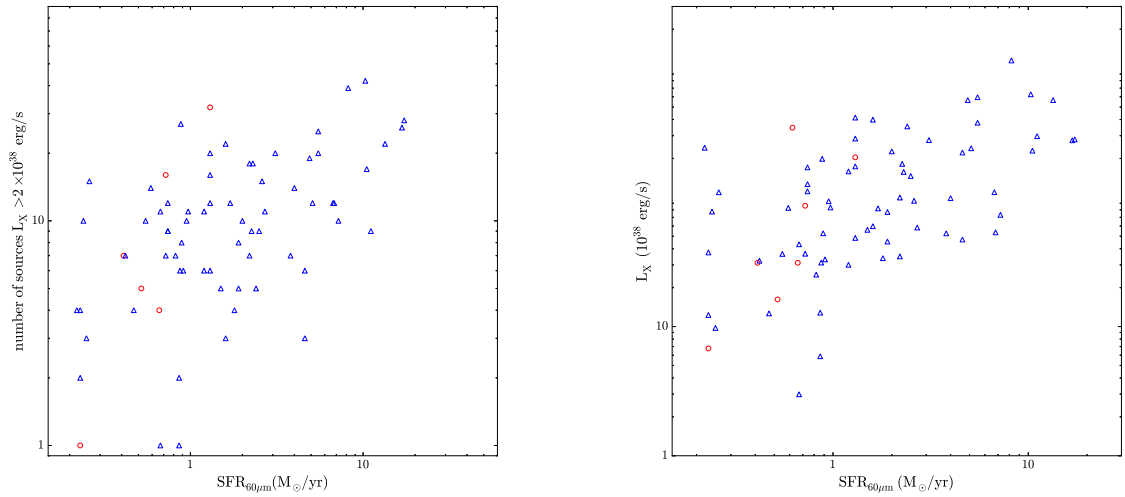



Fig. 21.— (a) Number of sources with luminosities exceeding $2 \times 10^{38}$ erg s$^{-1}$ versus SFR for galaxies. The data for galaxies are shown by circles and triangles for early- and late-type galaxies respectively. (b) The collective X-ray luminosity verse SFR. The trend is clear, but more diffuse than those from previous studies (e.g., Gilfanov et al. 2004a).

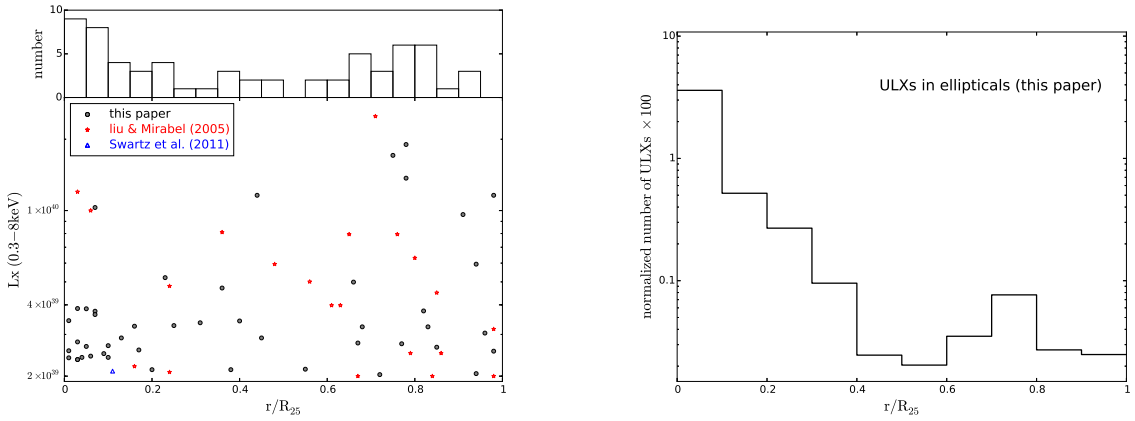



Fig. 22.— (a) The radial distribution of ULXs in elliptical galaxies detected in this paper and previous studies (Liu & Mirabel 2005; Swartz et al. 2011). The ULXs have a wide distribution in galaxies, although more ULXs above $10^{39}$ erg s$^{-1}$ are detected between 0.7 $D_{25}$ and $D_{25}$ isophote. (b) The radial distribution of normalized number of ULXs for elliptical galaxies. It is clear that a second peak is located out of the 0.5 $D_{25}$ isophote.

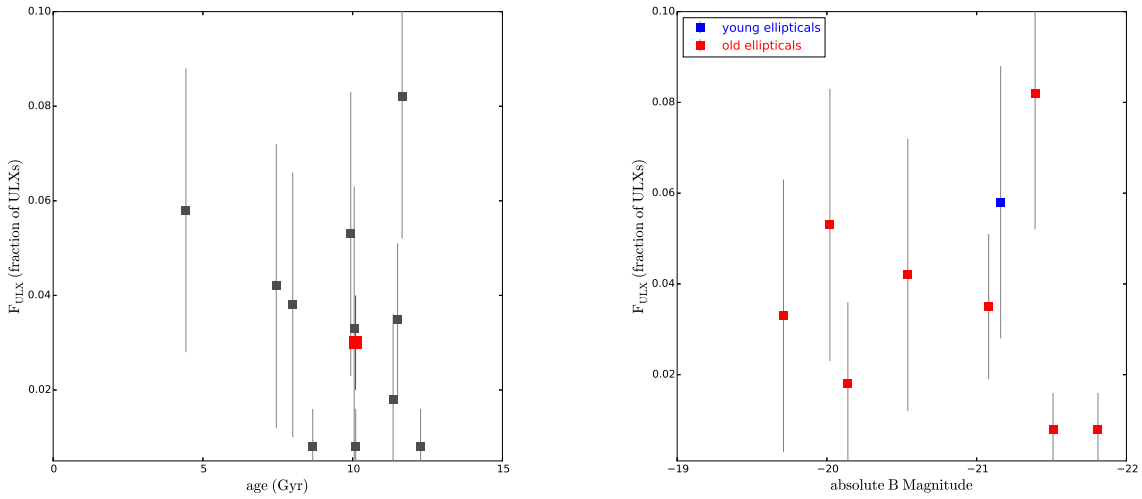



Fig. 23.— Fraction ($F_{ULX}$) of luminous ($L_X > 2 \times 10^{39}$ erg s$^{-1}$) X-ray sources against age and absolute $B$-band magnitude. A weak relation is seen between $F_{ULX}$ and age, while no dependency of $F_{ULX}$ on the stellar luminosity of the galaxy is found.

Table 1. X-ray Point Source Populations in 343 Nearby Galaxies

| Galaxy (1) | $N_{obs}$ (2) | $N^a_{src}$ (3) | $N^t_X$ (4) | $f_{Cov}$ (5) | lg $L_{X,lim}$ (6) | $N_X$ (7) | $N_{b/f}$ (8) | $N^a_U$ (9) | $n_U$ (10) | $n_{b/f}$ (11) | GType (12) | $L_B$ (13) | GArea (14) | Dist. (15) | $SFR_{60\mu m}$ (16) | activity (17) |
|---|---|---|---|---|---|---|---|---|---|---|---|---|---|---|---|---|
| NGC5813 | 1 | 20 | 19 | 1.00 | 38.57 | 19 | 1.88 | 5 | 4.57 | 0.43 | elliptical | 4.3e+10 | 9.87 | 32.21 | <0.12 | LINER |
| NGC1407 | 1 | 73 | 72 | 1.00 | 38.38 | 66 | 3.43 | 5 | 4.49 | 0.51 | elliptical | 6.7e+10 | 15.40 | 28.84 | 0.052 | - |
| NGC1399 | 11 | 129 | 117 | 1.00 | 37.98 | 117 | 8.58 | 5 | 2.53 | 0.47 | elliptical | 4.1e+10 | 35.11 | 19.95 | <0.16 | - |
| NGC3557 | 1 | 8 | 7 | 0.93 | 39.02 | 7 | 1.29 | 3 | 2.26 | 0.74 | elliptical | 1.6e+11 | 9.48 | 45.71 | 0.23 | - |
| NGC4494 | 2 | 18 | 18 | 1.00 | 38.13 | 17 | 2.14 | 2 | 1.89 | 0.11 | elliptical | 2.7e+10 | 13.29 | 17.06 | 0.028 | LINER |
| IC1459 | 1 | 48 | 47 | 0.99 | 38.22 | 47 | 4.83 | 2 | 1.41 | 0.59 | elliptical | 6.1e+10 | 15.64 | 29.24 | 0.18 | LINER |
| NGC3125 | 1 | 2 | 2 | 1.00 | 38.42 | 2 | 0.03 | 1 | 1.00 | 0.00 | elliptical | 1.2e+09 | 0.63 | 11.5 | 0.3 | - |
| NGC3379 | 6 | 69 | 43 | 1.00 | 37.22 | 43 | 7.28 | 1 | 0.95 | 0.05 | elliptical | 1.5e+10 | 20.28 | 10.57 | <0.026 | LINER |
| NGC3226 | 1 | 2 | 2 | 0.41 | 39.22 | 2 | 0.08 | 1 | 0.94 | 0.06 | elliptical | 9.0e+09 | 7.00 | 23.55 | <0.045 | LINER |
| NGC5198 | 1 | 4 | 4 | 0.68 | 38.98 | 4 | 0.27 | 1 | 0.86 | 0.14 | elliptical | 1.9e+10 | 2.91 | 39.0 | <0.051 | - |
| NGC1427 | 1 | 23 | 23 | 1.00 | 38.13 | 23 | 1.77 | 1 | 0.85 | 0.15 | elliptical | 1.6e+10 | 7.03 | 23.55 | <0.045 | - |
| NGC3078 | 1 | 2 | 2 | 1.00 | 39.32 | 2 | 0.23 | 1 | 0.77 | 0.23 | elliptical | 3.2e+10 | 4.16 | 35.16 | <0.061 | - |
| NGC720 | 5 | 47 | 35 | 1.00 | 38.32 | 35 | 2.09 | 3 | 0.71 | 0.29 | elliptical | 4.2e+10 | 8.82 | 27.67 | <0.076 | - |
| NGC5044 | 1 | 4 | 4 | 1.00 | 38.93 | 4 | 0.69 | 1 | 0.70 | 0.30 | elliptical | 3.2e+10 | 6.88 | 31.19 | 0.061 | - |
| NGC4125 | 1 | 25 | 25 | 0.97 | 38.02 | 25 | 4.41 | 1 | 0.70 | 0.30 | elliptical | 4.7e+10 | 14.30 | 23.88 | 0.15 | LINER |
| NGC3923 | 1 | 23 | 23 | 0.98 | 38.47 | 23 | 2.39 | 1 | 0.67 | 0.33 | elliptical | 4.6e+10 | 17.92 | 22.91 | <0.11 | - |
| NGC4374 | 4 | 58 | 38 | 1.00 | 38.02 | 38 | 6.12 | 5 | 0.66 | 0.34 | elliptical | 5.2e+10 | 28.51 | 18.37 | 0.076 | LINER |
| NGC6868 | 1 | 5 | 5 | 0.98 | 38.93 | 5 | 0.95 | 1 | 0.57 | 0.43 | elliptical | 4.9e+10 | 7.84 | 35.5 | 0.26 | - |
| NGC4261 | 1 | 23 | 21 | 1.00 | 38.47 | 20 | 2.59 | 1 | 0.50 | 0.50 | elliptical | 4.4e+10 | 11.66 | 31.62 | <0.13 | LINER |
| NGC4472 | 3 | 132 | 129 | 0.99 | 37.98 | 127 | 13.02 | 1 | 0.43 | 0.57 | elliptical | 7.6e+10 | 66.91 | 16.29 | <0.2 | Sy2 |
| PGC13452 | 11 | 0 | 0 | 1.00 | 37.63 | 0 | 0.21 | 0 | -0.00 | 0.00 | elliptical | 8.1e+07 | 0.95 | 12.0 | <0.0016 | - |
| NGC855 | 1 | 0 | 0 | 1.00 | 38.72 | 0 | 0.03 | 0 | -0.00 | 0.00 | elliptical | 1.0e+09 | 1.99 | 9.73 | 0.047 | - |
| NGC4627 | 1 | 0 | 0 | 0.95 | 36.98 | 0 | 1.11 | 0 | -0.00 | 0.00 | elliptical | 5.2e+08 | 3.61 | 7.2 | <0.0021 | - |
| NGC4467 | 3 | 1 | 0 | 0.90 | 38.57 | 0 | 0.05 | 0 | -0.01 | 0.01 | elliptical | 6.9e+08 | 0.87 | 16.8 | <0.0028 | - |
| NGC4283 | 7 | 3 | 3 | 1.00 | 37.57 | 3 | 0.65 | 0 | -0.01 | 0.01 | elliptical | 2.8e+09 | 1.77 | 15.70 | <0.005 | - |
| IC3773 | 1 | 0 | 0 | 1.00 | 38.57 | 0 | 0.06 | 0 | -0.01 | 0.01 | elliptical | 8.7e+08 | 1.10 | 14.5 | <0.0026 | - |
| NGC4168 | 1 | 2 | 2 | 0.53 | 38.68 | 2 | 0.15 | 0 | -0.02 | 0.02 | elliptical | 6.5e+09 | 4.99 | 16.8 | <0.017 | Sy1.9 |
| NGC3605 | 1 | 1 | 0 | 1.00 | 38.38 | 0 | 0.17 | 0 | -0.02 | 0.02 | elliptical | 4.2e+09 | 1.23 | 20.70 | <0.006 | - |
| NGC7173 | 1 | 4 | 4 | 0.93 | 38.47 | 4 | 0.17 | 0 | -0.03 | 0.03 | elliptical | 1.3e+10 | 0.82 | 31.33 | <0.0093 | - |
| NGC4564 | 1 | 4 | 4 | 1.00 | 38.13 | 4 | 0.56 | 0 | -0.03 | 0.03 | elliptical | 5.7e+09 | 4.11 | 15.00 | <0.01 | - |
| NGC3641 | 1 | 0 | 0 | 1.00 | 38.93 | 0 | 0.07 | 0 | -0.03 | 0.03 | elliptical | 2.8e+09 | 0.92 | 26.67 | <0.0074 | - |
| NGC3377 | 1 | 18 | 18 | 0.99 | 37.57 | 17 | 2.75 | 0 | -0.03 | 0.03 | elliptical | 7.2e+09 | 12.43 | 11.22 | 0.0079 | - |
| IC3019 | 1 | 0 | 0 | 1.00 | 39.02 | 0 | 0.07 | 0 | -0.03 | 0.03 | elliptical | 2.0e+09 | 1.47 | 24.1 | <0.0099 | - |
| NGC4589 | 1 | 6 | 6 | 0.46 | 38.42 | 6 | 0.43 | 0 | -0.05 | 0.05 | elliptical | 1.6e+10 | 6.35 | 21.98 | 0.046 | LINER |
| NGC4473 | 1 | 19 | 19 | 1.00 | 37.98 | 17 | 1.67 | 0 | -0.06 | 0.06 | elliptical | 1.5e+10 | 8.76 | 15.70 | <0.024 | - |
| NGC821 | 7 | 15 | 9 | 1.00 | 38.22 | 9 | 0.73 | 0 | -0.07 | 0.07 | elliptical | 1.8e+10 | 3.28 | 24.10 | <0.022 | - |
| NGC2434 | 1 | 16 | 15 | 1.00 | 38.32 | 15 | 0.72 | 0 | -0.07 | 0.07 | elliptical | 1.7e+10 | 4.44 | 21.58 | <0.023 | - |
| NGC1052 | 2 | 35 | 34 | 1.00 | 37.93 | 32 | 1.36 | 0 | -0.07 | 0.07 | elliptical | 1.7e+10 | 4.93 | 19.41 | 0.15 | Sy2 LINER |
| NGC3610 | 1 | 2 | 2 | 1.00 | 38.87 | 2 | 0.27 | 0 | -0.08 | 0.08 | elliptical | 1.7e+10 | 4.88 | 21.38 | <0.025 | - |
| NGC4697 | 1 | 64 | 63 | 1.00 | 37.52 | 63 | 6.54 | 0 | -0.09 | 0.09 | elliptical | 2.0e+10 | 26.61 | 11.75 | 0.029 | - |
| NGC4278 | 7 | 116 | 84 | 1.00 | 37.57 | 83 | 4.56 | 1 | -0.09 | 0.09 | elliptical | 1.6e+10 | 12.18 | 16.07 | 0.065 | Sy1 LINER |
| NGC3608 | 1 | 9 | 9 | 1.00 | 38.32 | 9 | 1.11 | 0 | -0.12 | 0.12 | elliptical | 1.7e+10 | 6.35 | 22.91 | <0.038 | LINER |
| NGC1404 | 11 | 20 | 1 | 1.00 | 38.27 | 1 | 1.32 | 1 | -0.12 | 0.12 | elliptical | 2.8e+10 | 7.72 | 20.99 | <0.04 | - |
| NGC3585 | 1 | 22 | 22 | 1.00 | 38.13 | 19 | 1.96 | 0 | -0.13 | 0.13 | elliptical | 3.4e+10 | 9.48 | 20.04 | 0.029 | - |
| NGC2986 | 1 | 1 | 1 | 1.00 | 39.63 | 1 | 0.13 | 0 | -0.13 | 0.13 | elliptical | 3.7e+10 | 6.85 | 32.3 | <0.08 | HII |

Table 1—Continued

| Galaxy (1) | $N_{obs}$ (2) | $N^a_{src}$ (3) | $N^t_X$ (4) | $f_{Cov}$ (5) | lg $L_{X,lim}$ (6) | $N_X$ (7) | $N_{b/f}$ (8) | $N^a_U$ (9) | $n_U$ (10) | $n_{b/f}$ (11) | GType (12) | $L_B$ (13) | GArea (14) | Dist. (15) | $SFR_{60\mu m}$ (16) | activity (17) |
|---|---|---|---|---|---|---|---|---|---|---|---|---|---|---|---|---|
| NGC4636 | 4 | 81 | 56 | 1.00 | 37.87 | 55 | 4.47 | 0 | -0.14 | 0.14 | elliptical | 2.2e+10 | 22.13 | 14.66 | 0.014 | LINER |
| NGC4552 | 1 | 68 | 67 | 1.00 | 37.72 | 64 | 5.15 | 0 | -0.14 | 0.14 | elliptical | 2.1e+10 | 18.74 | 15.35 | 0.017 | LINER HII |
| NGC4621 | 1 | 27 | 27 | 0.98 | 38.13 | 26 | 2.92 | 0 | -0.18 | 0.18 | elliptical | 3.2e+10 | 15.72 | 18.28 | <0.06 | - |
| NGC1199 | 1 | 5 | 5 | 1.00 | 38.63 | 4 | 0.68 | 0 | -0.18 | 0.18 | elliptical | 2.2e+10 | 3.58 | 33.11 | <0.045 | - |
| NGC2865 | 1 | 2 | 2 | 1.00 | 38.72 | 2 | 0.67 | 0 | -0.22 | 0.22 | elliptical | 3.0e+10 | 3.52 | 37.84 | 0.12 | - |
| NGC4649 | 1 | 126 | 111 | 0.91 | 38.02 | 107 | 6.07 | 1 | -0.27 | 0.27 | elliptical | 5.8e+10 | 35.20 | 16.83 | 0.099 | - |
| NGC4406 | 2 | 15 | 14 | 0.82 | 38.38 | 13 | 3.04 | 0 | -0.29 | 0.29 | elliptical | 5.8e+10 | 40.35 | 17.14 | 0.015 | - |
| NGC3640 | 1 | 3 | 3 | 1.00 | 38.93 | 3 | 0.71 | 0 | -0.29 | 0.29 | elliptical | 3.8e+10 | 9.88 | 27.04 | <0.082 | - |
| NGC4365 | 6 | 100 | 74 | 1.00 | 38.02 | 73 | 6.27 | 1 | -0.36 | 0.36 | elliptical | 4.1e+10 | 27.28 | 20.42 | <0.13 | - |
| NGC4696 | 7 | 9 | 8 | 1.00 | 38.52 | 8 | 2.69 | 1 | -0.63 | 0.63 | elliptical | 8.9e+10 | 11.35 | 35.48 | 0.057 | - |
| NGC4150 | 1 | 3 | 3 | 1.00 | 38.87 | 3 | 0.06 | 2 | 1.98 | 0.02 | lenticular | 3.2e+09 | 2.98 | 13.74 | 0.1 | - |
| NGC1316 | 1 | 56 | 56 | 0.79 | 38.27 | 55 | 10.30 | 2 | 1.03 | 0.97 | lenticular | 1.2e+11 | 80.24 | 21.48 | 0.62 | LINER |
| NGC4612 | 1 | 1 | 1 | 1.00 | 38.72 | 1 | 0.19 | 1 | 0.97 | 0.03 | lenticular | 4.9e+09 | 3.79 | 16.8 | <0.012 | - |
| NGC3384 | 6 | 6 | 5 | 0.75 | 38.13 | 5 | 0.76 | 1 | 0.97 | 0.03 | lenticular | 1.0e+10 | 10.89 | 11.59 | <0.017 | - |
| NGC7743 | 1 | 2 | 2 | 0.42 | 38.42 | 2 | 0.35 | 1 | 0.96 | 0.04 | lenticular | 9.0e+09 | 6.12 | 20.70 | 0.15 | Sy2 |
| NGC1389 | 11 | 2 | 2 | 0.99 | 38.22 | 2 | 0.51 | 1 | 0.95 | 0.05 | lenticular | 7.7e+09 | 2.49 | 21.68 | <0.014 | - |
| NGC4762 | 1 | 2 | 2 | 0.57 | 38.63 | 2 | 0.41 | 1 | 0.94 | 0.06 | lenticular | 1.7e+10 | 11.34 | 16.8 | <0.037 | LINER |
| NGC5128 | 10 | 389 | 248 | 0.99 | 36.77 | 240 | 76.01 | 2 | 0.89 | 0.11 | lenticular | 3.3e+10 | 402.47 | 4.21 | 1.3 | Sy2 |
| NGC4526 | 1 | 31 | 30 | 1.00 | 37.93 | 29 | 3.04 | 1 | 0.88 | 0.12 | lenticular | 2.7e+10 | 13.65 | 16.90 | 0.72 | - |
| NGC1553 | 1 | 26 | 26 | 1.00 | 38.13 | 26 | 1.88 | 1 | 0.88 | 0.12 | lenticular | 4.2e+10 | 9.88 | 18.54 | 0.074 | LINER |
| NGC5838 | 1 | 2 | 2 | 0.78 | 38.68 | 2 | 0.51 | 1 | 0.87 | 0.13 | lenticular | 2.6e+10 | 4.84 | 28.5 | 0.27 | LINER |
| NGC3665 | 1 | 2 | 2 | 0.80 | 38.98 | 2 | 0.32 | 1 | 0.84 | 0.16 | lenticular | 3.4e+10 | 3.94 | 32.4 | 0.9 | - |
| NGC4382 | 1 | 42 | 39 | 0.99 | 37.98 | 38 | 7.11 | 1 | 0.64 | 0.36 | lenticular | 5.3e+10 | 30.58 | 18.45 | 0.023 | - |
| PGC13449 | 11 | 0 | 0 | 1.00 | 37.93 | 0 | 0.13 | 0 | -0.00 | 0.00 | lenticular | 1.4e+08 | 1.08 | 11.0 | <0.0015 | - |
| NGC5102 | 1 | 3 | 3 | 1.00 | 36.72 | 3 | 3.97 | 0 | -0.00 | 0.00 | lenticular | 2.5e+09 | 19.27 | 4.00 | 0.0059 | - |
| NGC4310 | 1 | 1 | 1 | 1.00 | 38.52 | 1 | 0.05 | 0 | -0.00 | 0.00 | lenticular | 8.5e+08 | 2.11 | 9.7 | 0.034 | - |
| NGC404 | 2 | 1 | 1 | 1.00 | 36.63 | 1 | 1.79 | 0 | -0.00 | 0.00 | lenticular | 7.1e+08 | 9.40 | 3.27 | 0.01 | LINER |
| NGC3413 | 1 | 1 | 1 | 1.00 | 38.57 | 1 | 0.02 | 0 | -0.00 | 0.00 | lenticular | 6.7e+08 | 1.54 | 8.6 | 0.033 | - |
| NGC2787 | 2 | 14 | 14 | 1.00 | 37.32 | 14 | 0.96 | 0 | -0.00 | 0.00 | lenticular | 2.0e+09 | 5.06 | 7.48 | 0.016 | LINER |
| NGC1705 | 1 | 1 | 1 | 1.00 | 36.87 | 1 | 0.57 | 0 | -0.00 | 0.00 | lenticular | 5.2e+08 | 2.09 | 6.0 | 0.014 | HII |
| IC3260 | 1 | 0 | 0 | 1.00 | 37.77 | 0 | 0.13 | 0 | -0.00 | 0.00 | lenticular | 5.3e+08 | 0.69 | 12.5 | <0.0013 | - |
| IC3256 | 1 | 3 | 3 | 1.00 | 37.47 | 3 | 0.13 | 0 | -0.00 | 0.00 | lenticular | 6.9e+08 | 0.60 | 10.0 | <0.00068 | - |
| IC1473 | 1 | 0 | 0 | 1.00 | 38.57 | 0 | 0.05 | 0 | -0.00 | 0.00 | lenticular | 7.6e+08 | 1.67 | 11.2 | 0.033 | - |
| NGC4623 | 1 | 0 | 0 | 1.00 | 38.72 | 0 | 0.06 | 0 | -0.01 | 0.01 | lenticular | 2.3e+09 | 1.27 | 16.8 | <0.0041 | - |
| NGC4550 | 1 | 0 | 0 | 0.42 | 38.98 | 0 | 0.02 | 0 | -0.01 | 0.01 | lenticular | 4.4e+09 | 2.45 | 15.85 | 0.016 | LINER |
| NGC4309 | 2 | 0 | 0 | 1.00 | 38.38 | 0 | 0.09 | 0 | -0.01 | 0.01 | lenticular | 7.1e+08 | 1.58 | 11.6 | 0.056 | - |
| NGC4143 | 1 | 1 | 1 | 0.58 | 38.83 | 1 | 0.05 | 0 | -0.01 | 0.01 | lenticular | 6.8e+09 | 2.64 | 15.92 | <0.0076 | LINER |
| NGC4138 | 1 | 1 | 1 | 0.54 | 38.42 | 1 | 0.13 | 0 | -0.01 | 0.01 | lenticular | 4.2e+09 | 3.44 | 13.80 | <0.0075 | Sy1.9 |
| NGC4026 | 1 | 5 | 5 | 0.43 | 38.02 | 5 | 0.31 | 0 | -0.01 | 0.01 | lenticular | 6.6e+09 | 5.27 | 13.61 | 0.0083 | - |
| NGC3998 | 1 | 5 | 3 | 0.51 | 38.08 | 3 | 0.33 | 0 | -0.01 | 0.01 | lenticular | 7.8e+09 | 4.75 | 14.13 | 0.04 | Sy1 LINER |
| NGC1481 | 1 | 0 | 0 | 1.00 | 38.42 | 0 | 0.09 | 0 | -0.01 | 0.01 | lenticular | 1.4e+09 | 0.54 | 23.1 | 0.086 | - |
| PGC13343 | 2 | 1 | 1 | 1.00 | 38.47 | 1 | 0.13 | 0 | -0.02 | 0.02 | lenticular | 9.2e+08 | 0.95 | 22.1 | <0.0053 | - |
| NGC7465 | 1 | 1 | 1 | 1.00 | 39.27 | 1 | 0.03 | 0 | -0.02 | 0.02 | lenticular | 6.7e+09 | 0.78 | 27.2 | 1.3 | Sy2 |
| NGC5355 | 1 | 0 | 0 | 1.00 | 39.52 | 0 | 0.02 | 0 | -0.02 | 0.02 | lenticular | 4.0e+09 | 0.68 | 31.3 | <0.0075 | - |
| NGC4340 | 1 | 0 | 0 | 0.33 | 38.87 | 0 | 0.09 | 0 | -0.02 | 0.02 | lenticular | 6.8e+09 | 7.84 | 16.8 | 0.011 | - |

Table 1—Continued

| Galaxy (1) | $N_{obs}$ (2) | $N^a_{src}$ (3) | $N^t_X$ (4) | $f_{Cov}$ (5) | lg $L_{X,lim}$ (6) | $N_X$ (7) | $N_{b/f}$ (8) | $N^a_U$ (9) | $n_U$ (10) | $n_{b/f}$ (11) | GType (12) | $L_B$ (13) | GArea (14) | Dist. (15) | $SFR_{60\mu m}$ (16) | activity (17) |
|---|---|---|---|---|---|---|---|---|---|---|---|---|---|---|---|---|
| NGC4111 | 1 | 7 | 7 | 0.98 | 38.08 | 6 | 0.51 | 0 | -0.02 | 0.02 | lenticular | 7.9e+09 | 3.53 | 15.00 | <0.0091 | LINER HII |
| NGC3489 | 1 | 1 | 1 | 1.00 | 38.83 | 1 | 0.09 | 0 | -0.02 | 0.02 | lenticular | 7.8e+09 | 5.67 | 12.08 | <0.0092 | Sy2 |
| NGC3412 | 1 | 3 | 3 | 1.00 | 38.02 | 3 | 0.58 | 0 | -0.02 | 0.02 | lenticular | 5.8e+09 | 5.83 | 11.32 | <0.0086 | - |
| PGC20551 | 1 | 3 | 3 | 1.00 | 38.47 | 3 | 0.24 | 0 | -0.03 | 0.03 | lenticular | 1.4e+10 | 1.64 | 24.0 | 1.1 | - |
| NGC5354 | 1 | 0 | 0 | 0.76 | 39.57 | 0 | 0.03 | 0 | -0.03 | 0.03 | lenticular | 2.1e+10 | 1.49 | 34.3 | 0.22 | LINER |
| NGC4570 | 1 | 0 | 0 | 1.00 | 38.72 | 0 | 0.17 | 0 | -0.03 | 0.03 | lenticular | 8.3e+09 | 3.40 | 16.8 | <0.011 | - |
| NGC4350 | 1 | 3 | 3 | 1.00 | 38.72 | 3 | 0.17 | 0 | -0.03 | 0.03 | lenticular | 7.4e+09 | 3.42 | 16.8 | 0.05 | - |
| NGC3458 | 2 | 0 | 0 | 1.00 | 39.47 | 0 | 0.02 | 0 | -0.03 | 0.03 | lenticular | 7.2e+09 | 0.95 | 29.5 | <0.0094 | - |
| NGC3115 | 1 | 43 | 42 | 0.99 | 37.42 | 42 | 3.18 | 0 | -0.03 | 0.03 | lenticular | 1.8e+10 | 13.99 | 9.68 | <0.015 | - |
| NGC1386 | 1 | 6 | 6 | 1.00 | 38.18 | 6 | 0.50 | 0 | -0.03 | 0.03 | lenticular | 6.0e+09 | 3.40 | 16.52 | 0.66 | Sy2 |
| NGC1382 | 2 | 1 | 1 | 1.00 | 38.38 | 1 | 0.25 | 0 | -0.03 | 0.03 | lenticular | 2.5e+09 | 1.58 | 22.59 | <0.0092 | - |
| NGC7457 | 1 | 3 | 3 | 1.00 | 38.27 | 3 | 0.64 | 0 | -0.04 | 0.04 | lenticular | 5.3e+09 | 7.63 | 13.24 | 0.0087 | - |
| NGC5353 | 1 | 0 | 0 | 0.94 | 39.68 | 0 | 0.04 | 0 | -0.04 | 0.04 | lenticular | 3.6e+10 | 1.88 | 37.8 | 0.19 | - |
| NGC4435 | 1 | 2 | 2 | 1.00 | 38.22 | 2 | 0.59 | 0 | -0.04 | 0.04 | lenticular | 9.9e+09 | 4.34 | 16.8 | 0.23 | LINER HII |
| NGC4036 | 1 | 2 | 2 | 0.31 | 38.52 | 2 | 0.26 | 0 | -0.04 | 0.04 | lenticular | 2.4e+10 | 5.69 | 24.6 | 0.14 | LINER |
| NGC1482 | 1 | 1 | 1 | 1.00 | 38.18 | 1 | 0.51 | 0 | -0.04 | 0.04 | lenticular | 3.7e+09 | 2.67 | 19.6 | 5.5 | HII |
| NGC5866 | 2 | 23 | 22 | 1.00 | 37.87 | 20 | 1.61 | 0 | -0.05 | 0.05 | lenticular | 1.7e+10 | 7.20 | 15.35 | 0.52 | LINER HII |
| NGC5273 | 1 | 1 | 1 | 1.00 | 38.98 | 1 | 0.14 | 0 | -0.05 | 0.05 | lenticular | 4.7e+09 | 5.46 | 16.52 | 0.11 | Sy1.9 |
| NGC4459 | 1 | 4 | 4 | 1.00 | 38.38 | 4 | 0.66 | 0 | -0.05 | 0.05 | lenticular | 1.3e+10 | 7.45 | 16.14 | 0.2 | LINER HII |
| NGC4203 | 1 | 1 | 1 | 1.00 | 38.93 | 1 | 0.18 | 0 | -0.05 | 0.05 | lenticular | 8.0e+09 | 8.39 | 15.14 | 0.062 | LINER |
| NGC1023 | 1 | 9 | 9 | 0.98 | 38.08 | 9 | 1.73 | 0 | -0.05 | 0.05 | lenticular | 1.9e+10 | 20.09 | 11.43 | <0.03 | - |
| NGC5507 | 2 | 0 | 0 | 1.00 | 39.13 | 0 | 0.09 | 0 | -0.06 | 0.06 | lenticular | 8.6e+09 | 1.26 | 34.3 | <0.017 | - |
| NGC524 | 1 | 2 | 2 | 0.46 | 38.57 | 2 | 0.34 | 0 | -0.06 | 0.06 | lenticular | 3.0e+10 | 5.98 | 23.99 | 0.19 | - |
| NGC3564 | 1 | 1 | 1 | 0.89 | 38.87 | 1 | 0.14 | 0 | -0.06 | 0.06 | lenticular | 2.0e+10 | 1.06 | 37.6 | 0.33 | - |
| NGC3245 | 1 | 3 | 3 | 1.00 | 38.57 | 3 | 0.45 | 0 | -0.07 | 0.07 | lenticular | 1.5e+10 | 4.53 | 20.89 | 0.41 | LINER HII |
| NGC1387 | 2 | 9 | 9 | 0.88 | 38.18 | 9 | 1.05 | 0 | -0.07 | 0.07 | lenticular | 1.3e+10 | 6.25 | 20.32 | 0.41 | - |
| NGC4754 | 1 | 4 | 3 | 0.99 | 38.77 | 3 | 0.38 | 0 | -0.08 | 0.08 | lenticular | 1.3e+10 | 8.85 | 16.83 | <0.029 | - |
| NGC4596 | 1 | 6 | 6 | 1.00 | 38.42 | 6 | 0.86 | 0 | -0.08 | 0.08 | lenticular | 1.1e+10 | 9.25 | 16.8 | 0.062 | LINER |
| NGC4578 | 1 | 1 | 1 | 1.00 | 38.77 | 1 | 0.36 | 0 | -0.08 | 0.08 | lenticular | 7.2e+09 | 6.41 | 18.54 | <0.025 | - |
| NGC4233 | 1 | 2 | 2 | 0.67 | 38.87 | 2 | 0.19 | 0 | -0.08 | 0.08 | lenticular | 1.3e+10 | 2.07 | 35.1 | 0.11 | - |
| NGC3414 | 1 | 4 | 4 | 0.48 | 38.57 | 4 | 0.47 | 0 | -0.09 | 0.09 | lenticular | 1.8e+10 | 7.12 | 25.23 | 0.054 | - |
| NGC7049 | 1 | 1 | 1 | 0.98 | 39.77 | 1 | 0.10 | 1 | -0.10 | 0.10 | lenticular | 3.3e+10 | 9.84 | 29.92 | 0.21 | - |
| NGC3065 | 1 | 1 | 1 | 1.00 | 39.22 | 1 | 0.12 | 0 | -0.10 | 0.10 | lenticular | 1.1e+10 | 2.22 | 31.3 | 0.66 | - |
| NGC1332 | 2 | 32 | 30 | 1.00 | 38.08 | 30 | 1.35 | 0 | -0.10 | 0.10 | lenticular | 2.7e+10 | 5.29 | 22.91 | 0.12 | - |
| NGC6278 | 1 | 1 | 1 | 0.90 | 38.93 | 1 | 0.24 | 0 | -0.11 | 0.11 | lenticular | 1.2e+10 | 1.92 | 37.2 | <0.031 | - |
| NGC6861 | 1 | 2 | 2 | 1.00 | 38.72 | 2 | 0.50 | 0 | -0.13 | 0.13 | lenticular | 2.1e+10 | 4.03 | 28.05 | 0.3 | - |
| NGC3607 | 1 | 9 | 8 | 1.00 | 38.38 | 8 | 1.49 | 0 | -0.18 | 0.18 | lenticular | 3.9e+10 | 9.47 | 22.80 | <0.056 | - |
| NGC2300 | 1 | 1 | 1 | 1.00 | 38.72 | 1 | 0.63 | 0 | -0.20 | 0.20 | lenticular | 2.9e+10 | 4.52 | 31.0 | <0.052 | - |
| NGC1550 | 4 | 3 | 1 | 1.00 | 39.08 | 1 | 0.56 | 2 | -0.35 | 0.35 | lenticular | 3.4e+10 | 3.45 | 49.5 | <0.097 | - |
| NGC474 | 1 | 5 | 5 | 0.99 | 38.87 | 5 | 4.25 | 0 | -1.72 | 1.72 | lenticular | 2.7e+10 | 35.14 | 32.5 | <0.43 | - |
| NGC3034 | 9 | 56 | 28 | 1.00 | 36.87 | 28 | 7.08 | 3 | 2.99 | 0.01 | irregular | 7.9e+09 | 37.54 | 5.2 | 13.4 | Sbrst HII |
| PGC23324 | 1 | 1 | 1 | 0.31 | 37.57 | 1 | 0.58 | 1 | 1.00 | 0.00 | irregular | 1.4e+09 | 39.29 | 4.5 | 0.01 | - |
| NGC4485 | 3 | 3 | 3 | 1.00 | 37.42 | 3 | 0.65 | 1 | 1.00 | 0.00 | irregular | 1.7e+09 | 2.93 | 9.3 | 0.09 | HII |
| NGC1427A | 1 | 8 | 6 | 1.00 | 37.83 | 6 | 0.69 | 1 | 0.98 | 0.02 | irregular | 2.2e+09 | 2.72 | 16.9 | 0.027 | - |
| IC3583 | 2 | 1 | 1 | 1.00 | 39.27 | 1 | 0.02 | 1 | 0.98 | 0.02 | irregular | 2.2e+09 | 1.92 | 16.8 | 0.062 | - |

Table 1—Continued

| Galaxy (1) | $N_{obs}$ (2) | $N^a_{src}$ (3) | $N^t_X$ (4) | $f_{Cov}$ (5) | lg $L_{X,lim}$ (6) | $N_X$ (7) | $N_{b/f}$ (8) | $N^a_U$ (9) | $n_U$ (10) | $n_{b/f}$ (11) | GType (12) | $L_B$ (13) | GArea (14) | Dist. (15) | $SFR_{60\mu m}$ (16) | activity (17) |
|---|---|---|---|---|---|---|---|---|---|---|---|---|---|---|---|---|
| PGC28757 | 19 | 1 | 1 | 0.97 | 37.42 | 1 | 0.14 | 0 | -0.00 | 0.00 | irregular | 4.2e+07 | 4.04 | 3.42 | <0.00053 | - |
| PGC24175 | 1 | 3 | 3 | 1.00 | 37.77 | 3 | 0.27 | 0 | -0.00 | 0.00 | irregular | 1.8e+09 | 1.86 | 10.5 | <0.0023 | Sbrst |
| NGC4449 | 1 | 22 | 22 | 1.00 | 36.52 | 21 | 3.99 | 0 | -0.00 | 0.00 | irregular | 1.5e+09 | 21.09 | 3.0 | <0.0022 | HII |
| NGC3077 | 1 | 15 | 15 | 0.98 | 36.57 | 15 | 4.72 | 0 | -0.00 | 0.00 | irregular | 1.4e+09 | 18.93 | 4.04 | 0.1 | HII |
| NGC2337 | 1 | 1 | 1 | 1.00 | 38.57 | 1 | 0.04 | 0 | -0.00 | 0.00 | irregular | 1.1e+09 | 2.92 | 8.2 | 0.051 | - |
| NGC1800 | 1 | 1 | 1 | 0.84 | 37.13 | 1 | 0.36 | 0 | -0.00 | 0.00 | irregular | 6.0e+08 | 1.73 | 7.4 | 0.019 | HII |
| NGC1569 | 2 | 11 | 11 | 1.00 | 35.77 | 11 | 1.30 | 0 | -0.00 | 0.00 | irregular | 6.7e+08 | 5.09 | 1.6 | 0.052 | Sy1 Sbrst |
| NGC1156 | 1 | 0 | 0 | 1.00 | 38.32 | 0 | 0.09 | 0 | -0.00 | 0.00 | irregular | 1.7e+09 | 6.41 | 6.4 | 0.096 | - |
| NGC1023A | 1 | 0 | 0 | 0.50 | 37.98 | 0 | 0.03 | 0 | -0.00 | 0.00 | irregular | 3.8e+08 | 0.64 | 9.9 | <0.00071 | - |
| IC3647 | 1 | 0 | 0 | 1.00 | 38.13 | 0 | 0.05 | 0 | -0.00 | 0.00 | irregular | 1.8e+08 | 1.04 | 8.5 | <0.00088 | - |
| NGC5195 | 5 | 16 | 7 | 0.83 | 37.38 | 7 | 2.54 | 0 | -0.01 | 0.01 | irregular | 6.0e+09 | 20.72 | 7.66 | 0.42 | LINER |
| NGC4214 | 3 | 23 | 14 | 1.00 | 36.68 | 14 | 8.00 | 0 | -0.01 | 0.01 | irregular | 1.7e+09 | 44.30 | 3.5 | 0.099 | HII |
| NGC3239 | 1 | 4 | 4 | 1.00 | 38.52 | 4 | 0.17 | 0 | -0.01 | 0.01 | irregular | 2.4e+09 | 13.09 | 8.1 | 0.1 | - |
| NGC14 | 1 | 0 | 0 | 1.00 | 38.57 | 0 | 0.18 | 0 | -0.02 | 0.02 | irregular | 2.4e+09 | 4.65 | 12.8 | 0.053 | - |
| NGC7715 | 1 | 1 | 1 | 0.90 | 38.47 | 1 | 0.23 | 0 | -0.05 | 0.05 | irregular | 5.4e+09 | 1.01 | 36.3 | <0.015 | - |
| NGC3396 | 1 | 6 | 5 | 0.93 | 38.42 | 5 | 0.39 | 1 | -0.05 | 0.05 | irregular | 8.6e+09 | 2.87 | 21.8 | <0.016 | - |
| NGC3256 | 2 | 26 | 11 | 1.00 | 38.83 | 11 | 1.02 | 16 | 5.60 | 0.40 | peculiar | 3.0e+10 | 6.39 | 37.4 | 55.4 | Sbrst HII |
| NGC520 | 1 | 10 | 10 | 1.00 | 38.32 | 10 | 1.50 | 2 | 1.79 | 0.21 | peculiar | 1.5e+10 | 6.38 | 27.8 | 11.1 | - |
| PGC35286 | 1 | 2 | 2 | 1.00 | 36.18 | 2 | 0.10 | 0 | 0.00 | 0.00 | peculiar | 4.8e+06 | 0.93 | 1.4 | 0.00034 | - |
| NGC5253 | 3 | 18 | 13 | 1.00 | 36.32 | 13 | 2.10 | 0 | -0.00 | 0.00 | peculiar | 1.0e+09 | 7.73 | 3.221 | 0.14 | Sbrst HII |
| NGC1036 | 1 | 0 | 0 | 1.00 | 38.57 | 0 | 0.03 | 0 | -0.00 | 0.00 | peculiar | 6.1e+08 | 1.18 | 11.2 | 0.068 | - |
| NGC2782 | 1 | 16 | 16 | 1.00 | 38.72 | 15 | 1.33 | 7 | 6.56 | 0.44 | S0/a-Sa | 3.4e+10 | 6.96 | 37.3 | 5.4 | Sy1 Sbrst |
| NGC2993 | 1 | 4 | 4 | 1.00 | 38.47 | 4 | 0.20 | 2 | 1.96 | 0.04 | S0/a-Sa | 1.2e+10 | 0.97 | 30.5 | 4.6 | HII |
| NGC4691 | 1 | 6 | 6 | 0.87 | 38.63 | 6 | 0.44 | 2 | 1.92 | 0.08 | S0/a-Sa | 1.8e+10 | 5.09 | 22.5 | 3.2 | HII |
| NGC4670 | 1 | 1 | 1 | 1.00 | 38.57 | 1 | 0.04 | 1 | 1.00 | 0.00 | S0/a-Sa | 1.3e+09 | 1.24 | 11.0 | 0.14 | - |
| NGC1012 | 1 | 4 | 4 | 1.00 | 38.63 | 4 | 0.09 | 1 | 0.99 | 0.01 | S0/a-Sa | 4.0e+09 | 2.18 | 14.4 | 0.46 | - |
| NGC7013 | 1 | 4 | 4 | 1.00 | 38.72 | 4 | 0.15 | 1 | 0.98 | 0.02 | S0/a-Sa | 1.6e+10 | 4.44 | 14.2 | 0.17 | LINER |
| NGC3955 | 1 | 4 | 4 | 1.00 | 38.38 | 4 | 0.31 | 1 | 0.97 | 0.03 | S0/a-Sa | 1.0e+10 | 2.13 | 20.6 | 1.6 | HII |
| NGC3169 | 1 | 2 | 2 | 0.40 | 39.22 | 2 | 0.07 | 1 | 0.95 | 0.05 | S0/a-Sa | 2.5e+10 | 9.45 | 19.7 | 1.4 | LINER |
| NGC1808 | 1 | 19 | 19 | 0.98 | 37.52 | 19 | 4.29 | 1 | 0.95 | 0.05 | S0/a-Sa | 1.2e+10 | 19.79 | 10.8 | 4.6 | Sy2 |
| NGC5506 | 2 | 2 | 2 | 1.00 | 38.93 | 2 | 0.16 | 1 | 0.94 | 0.06 | S0/a-Sa | 1.6e+10 | 1.90 | 28.7 | 3.2 | Sy1.9 |
| NGC3623 | 1 | 4 | 4 | 0.99 | 38.83 | 4 | 0.40 | 1 | 0.91 | 0.09 | S0/a-Sa | 3.2e+10 | 22.12 | 12.3 | 0.2 | LINER |
| NGC7727 | 1 | 10 | 9 | 1.00 | 38.47 | 8 | 1.91 | 1 | 0.72 | 0.28 | S0/a-Sa | 2.6e+10 | 13.08 | 23.3 | <0.081 | - |
| NGC5358 | 1 | 0 | 0 | 0.39 | 39.68 | 0 | 0.00 | 0 | -0.00 | 0.00 | S0/a-Sa | 3.3e+09 | 0.29 | 32.0 | <0.0034 | - |
| NGC4491 | 1 | 0 | 0 | 1.00 | 38.27 | 0 | 0.02 | 0 | -0.00 | 0.00 | S0/a-Sa | 3.5e+08 | 1.15 | 6.6 | 0.055 | - |
| NGC3593 | 1 | 0 | 0 | 1.00 | 38.13 | 0 | 0.15 | 0 | -0.00 | 0.00 | S0/a-Sa | 1.2e+09 | 7.98 | 5.5 | 0.25 | Sy2 HII |
| NGC4419 | 2 | 4 | 4 | 1.00 | 38.52 | 4 | 0.14 | 0 | -0.01 | 0.01 | S0/a-Sa | 6.4e+09 | 2.92 | 13.49 | 0.66 | LINER HII |
| NGC4245 | 1 | 0 | 0 | 1.00 | 38.57 | 0 | 0.11 | 0 | -0.01 | 0.01 | S0/a-Sa | 2.3e+09 | 4.93 | 9.7 | 0.033 | HII |
| NGC3600 | 1 | 0 | 0 | 1.00 | 38.57 | 0 | 0.07 | 0 | -0.01 | 0.01 | S0/a-Sa | 3.2e+09 | 2.76 | 10.8 | 0.068 | - |
| NGC4772 | 1 | 1 | 1 | 0.46 | 38.63 | 1 | 0.13 | 0 | -0.02 | 0.02 | S0/a-Sa | 7.2e+09 | 4.51 | 16.3 | <0.014 | LINER |
| NGC4314 | 3 | 14 | 12 | 1.00 | 37.72 | 11 | 1.77 | 0 | -0.02 | 0.02 | S0/a-Sa | 4.9e+09 | 12.09 | 9.7 | 0.16 | LINER |
| NGC4594 | 3 | 142 | 132 | 1.00 | 37.38 | 131 | 6.05 | 2 | -0.05 | 0.05 | S0/a-Sa | 6.5e+10 | 24.19 | 9.77 | 0.13 | Sy1.9 LINER |
| NGC4457 | 1 | 7 | 7 | 1.00 | 37.93 | 7 | 1.11 | 0 | -0.05 | 0.05 | S0/a-Sa | 1.1e+10 | 4.88 | 17.4 | 0.67 | LINER |
| NGC2798 | 1 | 2 | 2 | 1.00 | 39.02 | 2 | 0.12 | 0 | -0.06 | 0.06 | S0/a-Sa | 1.2e+10 | 1.99 | 27.1 | 6.3 | - |
| NGC1291 | 2 | 75 | 51 | 1.00 | 37.52 | 51 | 9.99 | 0 | -0.07 | 0.07 | S0/a-Sa | 2.1e+10 | 62.52 | 8.6 | 0.06 | - |

Table 1—Continued

| Galaxy (1) | $N_{obs}$ (2) | $N^a_{src}$ (3) | $N^t_X$ (4) | $f_{Cov}$ (5) | lg $L_{X,lim}$ (6) | $N_X$ (7) | $N_{b/f}$ (8) | $N^a_U$ (9) | $n_U$ (10) | $n_{b/f}$ (11) | GType (12) | $L_B$ (13) | GArea (14) | Dist. (15) | $SFR_{60\mu m}$ (16) | activity (17) |
|---|---|---|---|---|---|---|---|---|---|---|---|---|---|---|---|---|
| NGC2681 | 2 | 19 | 17 | 1.00 | 37.68 | 15 | 3.52 | 1 | -0.09 | 0.09 | S0/a-Sa | 2.0e+10 | 9.49 | 17.22 | 0.95 | Sy |
| NGC3190 | 1 | 6 | 6 | 1.00 | 38.38 | 6 | 0.85 | 0 | -0.10 | 0.10 | S0/a-Sa | 2.1e+10 | 5.27 | 22.4 | 0.72 | LINER |
| NGC660 | 2 | 4 | 4 | 1.00 | 38.57 | 4 | 0.97 | 0 | -0.11 | 0.11 | S0/a-Sa | 8.0e+09 | 20.65 | 14.0 | 6.2 | LINER HII |
| NGC7172 | 1 | 1 | 1 | 0.93 | 38.72 | 1 | 0.38 | 0 | -0.12 | 0.12 | S0/a-Sa | 1.7e+10 | 2.67 | 33.9 | 2.9 | Sy2 |
| NGC2992 | 1 | 2 | 2 | 1.00 | 38.52 | 2 | 0.58 | 0 | -0.12 | 0.12 | S0/a-Sa | 2.0e+10 | 3.06 | 30.5 | <0.033 | Sy1 |
| NGC4438 | 1 | 14 | 14 | 0.98 | 38.08 | 14 | 3.35 | 0 | -0.18 | 0.18 | S0/a-Sa | 2.8e+10 | 21.14 | 16.8 | 0.55 | LINER |
| IC5267 | 1 | 19 | 19 | 1.00 | 38.02 | 18 | 4.07 | 0 | -0.25 | 0.25 | S0/a-Sa | 2.1e+10 | 15.97 | 21.0 | 0.17 | - |
| NGC1371 | 1 | 9 | 8 | 1.00 | 38.57 | 8 | 2.11 | 0 | -0.37 | 0.37 | S0/a-Sa | 2.4e+10 | 17.13 | 23.4 | 0.049 | - |
| NGC1365 | 7 | 40 | 31 | 0.91 | 38.27 | 30 | 6.11 | 6 | 4.51 | 0.49 | Sab-Sb | 5.0e+10 | 54.28 | 17.38 | 10.3 | Sy1.8 Sbrst |
| NGC1672 | 1 | 28 | 28 | 0.97 | 37.77 | 28 | 6.39 | 4 | 3.83 | 0.17 | Sab-Sb | 2.6e+10 | 28.41 | 14.5 | 3.1 | Sy2 Sbrst |
| NGC2146 | 6 | 21 | 13 | 1.00 | 38.52 | 13 | 1.33 | 4 | 2.84 | 0.16 | Sab-Sb | 2.7e+10 | 15.98 | 17.2 | 17.3 | Sbrst |
| NGC4565 | 2 | 39 | 39 | 0.86 | 37.77 | 38 | 6.31 | 3 | 2.77 | 0.23 | Sab-Sb | 1.1e+11 | 26.62 | 17.46 | 1.3 | Sy3 |
| PGC50779 | 4 | 21 | 19 | 1.00 | 37.27 | 19 | 1.35 | 3 | 2.00 | 0.00 | Sab-Sb | 1.1e+10 | 16.41 | 4.2 | 2.0 | Sy2 |
| NGC4579 | 2 | 19 | 18 | 0.55 | 37.87 | 18 | 2.44 | 2 | 1.90 | 0.10 | Sab-Sb | 3.3e+10 | 21.61 | 16.8 | 0.74 | Sy1.9 LINER |
| NGC7174 | 1 | 5 | 4 | 0.88 | 38.63 | 4 | 0.40 | 2 | 1.89 | 0.11 | Sab-Sb | 1.0e+10 | 2.21 | 35.5 | <0.032 | - |
| NGC4501 | 2 | 19 | 18 | 0.91 | 38.27 | 18 | 2.23 | 2 | 1.84 | 0.16 | Sab-Sb | 5.0e+10 | 20.22 | 16.8 | 2.3 | Sy2 |
| NGC1068 | 3 | 41 | 36 | 0.98 | 37.77 | 34 | 7.26 | 3 | 1.82 | 0.18 | Sab-Sb | 5.2e+10 | 33.47 | 14.4 | 16.8 | Sy1 |
| NGC5678 | 1 | 2 | 2 | 1.00 | 39.38 | 2 | 0.21 | 2 | 1.79 | 0.21 | Sab-Sb | 4.2e+10 | 4.22 | 35.6 | 5.4 | LINER |
| NGC1097 | 2 | 19 | 17 | 0.97 | 38.57 | 17 | 2.73 | 2 | 1.61 | 0.39 | Sab-Sb | 4.7e+10 | 46.36 | 16.8 | 6.0 | Sy1 |
| NGC891 | 2 | 50 | 47 | 0.94 | 37.02 | 47 | 9.05 | 2 | 0.97 | 0.03 | Sab-Sb | 1.9e+10 | 26.68 | 8.36 | 1.9 | HII |
| NGC3031 | 19 | 122 | 104 | 0.73 | 36.52 | 99 | 27.75 | 1 | 0.97 | 0.03 | Sab-Sb | 2.0e+10 | 298.53 | 3.42 | 0.24 | Sy1.8 LINER |
| NGC3627 | 1 | 9 | 9 | 0.99 | 38.57 | 9 | 0.44 | 1 | 0.96 | 0.04 | Sab-Sb | 2.6e+10 | 29.80 | 8.75 | 1.9 | Sy2 LINER |
| NGC4698 | 1 | 9 | 9 | 1.00 | 37.98 | 9 | 1.59 | 1 | 0.93 | 0.07 | Sab-Sb | 1.4e+10 | 7.69 | 16.8 | 0.033 | Sy2 |
| NGC3628 | 4 | 32 | 31 | 0.86 | 37.38 | 31 | 7.30 | 1 | 0.93 | 0.07 | Sab-Sb | 3.3e+10 | 34.41 | 10.6 | 2.5 | LINER |
| NGC4750 | 1 | 2 | 2 | 1.00 | 39.08 | 2 | 0.17 | 1 | 0.91 | 0.09 | Sab-Sb | 1.7e+10 | 2.98 | 26.1 | 1.4 | LINER |
| NGC3675 | 1 | 1 | 1 | 1.00 | 39.08 | 1 | 0.22 | 1 | 0.90 | 0.10 | Sab-Sb | 2.5e+10 | 14.22 | 16.1 | 1.3 | LINER |
| NGC7714 | 1 | 7 | 7 | 1.00 | 38.52 | 7 | 0.53 | 1 | 0.87 | 0.13 | Sab-Sb | 1.9e+10 | 2.09 | 36.9 | 6.7 | LINER HII |
| NGC6870 | 1 | 4 | 4 | 1.00 | 38.98 | 4 | 0.27 | 1 | 0.86 | 0.14 | Sab-Sb | 1.8e+10 | 2.57 | 35.5 | 0.33 | - |
| NGC3898 | 1 | 20 | 20 | 1.00 | 38.02 | 20 | 2.41 | 1 | 0.84 | 0.16 | Sab-Sb | 2.2e+10 | 8.77 | 21.9 | 0.091 | LINER HII |
| NGC4151 | 3 | 9 | 7 | 1.00 | 38.22 | 7 | 3.87 | 2 | 0.71 | 0.29 | Sab-Sb | 3.3e+10 | 22.07 | 20.3 | 1.2 | Sy1.5 |
| NGC4312 | 1 | 0 | 0 | 1.00 | 37.27 | 0 | 0.06 | 0 | -0.00 | 0.00 | Sab-Sb | 1.1e+08 | 4.03 | 2.0 | 0.0038 | - |
| NGC949 | 1 | 0 | 0 | 1.00 | 38.72 | 0 | 0.04 | 0 | -0.01 | 0.01 | Sab-Sb | 3.8e+09 | 2.41 | 11.27 | 0.21 | - |
| NGC4448 | 1 | 0 | 0 | 1.00 | 38.57 | 0 | 0.09 | 0 | -0.01 | 0.01 | Sab-Sb | 4.5e+09 | 4.35 | 9.7 | 0.059 | - |
| NGC4343 | 1 | 1 | 0 | 1.00 | 38.52 | 0 | 0.07 | 0 | -0.01 | 0.01 | Sab-Sb | 3.2e+09 | 1.42 | 13.5 | 0.098 | - |
| NGC278 | 2 | 8 | 6 | 1.00 | 37.72 | 6 | 0.62 | 1 | -0.01 | 0.01 | Sab-Sb | 1.2e+10 | 3.23 | 11.8 | 1.5 | - |
| NGC3982 | 1 | 2 | 2 | 0.62 | 38.38 | 2 | 0.23 | 0 | -0.02 | 0.02 | Sab-Sb | 9.5e+09 | 3.75 | 17.0 | 0.86 | Sy2 |
| NGC3245A | 1 | 0 | 0 | 1.00 | 39.02 | 0 | 0.04 | 0 | -0.02 | 0.02 | Sab-Sb | 4.0e+09 | 0.89 | 23.1 | <0.0055 | - |
| NGC2683 | 1 | 2 | 2 | 0.99 | 38.42 | 2 | 0.29 | 0 | -0.02 | 0.02 | Sab-Sb | 1.3e+10 | 15.99 | 7.73 | 0.25 | Sy2 LINER |
| NGC4826 | 1 | 2 | 2 | 0.98 | 38.32 | 2 | 0.82 | 0 | -0.03 | 0.03 | Sab-Sb | 2.6e+10 | 42.25 | 7.48 | 0.86 | Sy2 |
| NGC4274 | 1 | 0 | 0 | 1.00 | 38.63 | 0 | 0.24 | 0 | -0.03 | 0.03 | Sab-Sb | 8.5e+09 | 13.38 | 9.7 | 0.19 | - |
| NGC3507 | 1 | 12 | 12 | 1.00 | 37.57 | 12 | 1.81 | 0 | -0.03 | 0.03 | Sab-Sb | 4.8e+09 | 7.65 | 11.8 | <0.012 | LINER |
| NGC7463 | 1 | 0 | 0 | 0.85 | 39.47 | 0 | 0.04 | 0 | -0.04 | 0.04 | Sab-Sb | 1.8e+10 | 1.54 | 33.5 | <0.02 | - |
| NGC4102 | 1 | 2 | 2 | 1.00 | 38.72 | 2 | 0.20 | 0 | -0.04 | 0.04 | Sab-Sb | 1.0e+10 | 4.13 | 17.0 | 6.6 | LINER HII |
| NGC4013 | 2 | 15 | 15 | 1.00 | 37.72 | 15 | 1.37 | 0 | -0.04 | 0.04 | Sab-Sb | 1.4e+10 | 4.20 | 17.0 | 0.91 | LINER |
| NGC6500 | 1 | 1 | 1 | 1.00 | 39.83 | 1 | 0.05 | 1 | -0.05 | 0.05 | Sab-Sb | 2.6e+10 | 2.77 | 40.0 | 0.46 | LINER |

Table 1—Continued

| Galaxy (1) | $N_{obs}$ (2) | $N^a_{src}$ (3) | $N^t_X$ (4) | $f_{Cov}$ (5) | lg $L_{X,lim}$ (6) | $N_X$ (7) | $N_{b/f}$ (8) | $N^a_U$ (9) | $n_U$ (10) | $n_{b/f}$ (11) | GType (12) | $L_B$ (13) | GArea (14) | Dist. (15) | $SFR_{60\mu m}$ (16) | activity (17) |
|---|---|---|---|---|---|---|---|---|---|---|---|---|---|---|---|---|
| NGC4388 | 1 | 8 | 8 | 1.00 | 38.18 | 8 | 0.83 | 0 | -0.05 | 0.05 | Sab-Sb | 2.1e+10 | 5.65 | 16.8 | 1.3 | Sy2 |
| NGC4217 | 1 | 18 | 18 | 1.00 | 37.72 | 18 | 2.07 | 0 | -0.05 | 0.05 | Sab-Sb | 1.3e+10 | 6.34 | 17.0 | 1.2 | HII |
| NGC4216 | 1 | 4 | 3 | 0.51 | 38.68 | 3 | 0.32 | 0 | -0.05 | 0.05 | Sab-Sb | 4.6e+10 | 11.35 | 16.8 | 0.12 | LINER HII |
| NGC3351 | 3 | 28 | 18 | 1.00 | 37.42 | 16 | 6.44 | 0 | -0.05 | 0.05 | Sab-Sb | 1.1e+10 | 29.25 | 9.55 | 0.82 | Sbrst HII |
| NGC3368 | 2 | 3 | 3 | 1.00 | 38.63 | 1 | 0.55 | 0 | -0.06 | 0.06 | Sab-Sb | 1.8e+10 | 31.19 | 9.772 | 0.47 | Sy LINER |
| NGC7582 | 2 | 9 | 8 | 1.00 | 38.42 | 8 | 0.83 | 0 | -0.08 | 0.08 | Sab-Sb | 2.2e+10 | 8.28 | 17.6 | 6.8 | Sy2 |
| NGC2841 | 2 | 33 | 33 | 1.00 | 37.72 | 31 | 4.07 | 0 | -0.08 | 0.08 | Sab-Sb | 3.3e+10 | 22.58 | 12.0 | 0.19 | Sy1 LINER |
| NGC1055 | 2 | 4 | 4 | 1.00 | 38.52 | 4 | 0.79 | 0 | -0.08 | 0.08 | Sab-Sb | 1.4e+10 | 15.95 | 13.5 | 1.9 | LINER |
| NGC5347 | 1 | 1 | 1 | 1.00 | 38.68 | 1 | 0.38 | 0 | -0.11 | 0.11 | Sab-Sb | 1.2e+10 | 1.82 | 36.7 | 0.85 | Sy2 |
| NGC7331 | 1 | 39 | 39 | 0.61 | 37.87 | 39 | 3.82 | 0 | -0.12 | 0.12 | Sab-Sb | 5.8e+10 | 30.62 | 14.52 | 2.2 | LINER |
| NGC5350 | 1 | 1 | 1 | 0.90 | 39.63 | 1 | 0.14 | 2 | -0.14 | 0.14 | Sab-Sb | 3.5e+10 | 5.66 | 37.8 | 1.4 | Sbrst |
| NGC4725 | 2 | 33 | 32 | 0.98 | 37.72 | 31 | 10.69 | 0 | -0.21 | 0.21 | Sab-Sb | 2.6e+10 | 63.82 | 11.64 | 0.26 | Sy2 |
| NGC5746 | 1 | 16 | 15 | 0.86 | 38.63 | 15 | 1.07 | 0 | -0.25 | 0.25 | Sab-Sb | 1.2e+11 | 7.69 | 29.4 | 0.51 | - |
| NGC4569 | 2 | 23 | 23 | 1.00 | 37.98 | 22 | 6.45 | 1 | -0.28 | 0.28 | Sab-Sb | 5.3e+10 | 32.67 | 16.8 | 0.97 | Sy LINER |
| IC2560 | 2 | 4 | 4 | 1.00 | 38.63 | 4 | 1.18 | 0 | -0.34 | 0.34 | Sab-Sb | 4.0e+10 | 4.96 | 39.0 | 2.2 | Sy2 |
| NGC3310 | 1 | 21 | 21 | 1.00 | 37.93 | 21 | 1.46 | 9 | 8.93 | 0.07 | Sbc-Sc | 2.2e+10 | 5.84 | 18.7 | 4.9 | HII |
| NGC2276 | 1 | 14 | 14 | 1.00 | 38.63 | 13 | 1.33 | 5 | 5.62 | 0.38 | Sbc-Sc | 4.2e+10 | 5.98 | 36.8 | 7.3 | - |
| NGC5170 | 1 | 11 | 11 | 0.90 | 38.77 | 11 | 0.88 | 5 | 4.71 | 0.29 | Sbc-Sc | 1.1e+11 | 6.67 | 33.7 | 0.56 | - |
| NGC5775 | 1 | 24 | 23 | 1.00 | 38.18 | 23 | 0.90 | 4 | 2.90 | 0.10 | Sbc-Sc | 3.6e+10 | 3.27 | 26.7 | 5.5 | - |
| NGC3631 | 1 | 39 | 39 | 1.00 | 37.87 | 39 | 6.24 | 3 | 2.71 | 0.29 | Sbc-Sc | 2.9e+10 | 18.92 | 21.6 | 1.6 | - |
| NGC5194 | 5 | 99 | 67 | 0.90 | 37.22 | 64 | 12.67 | 2 | 1.95 | 0.05 | Sbc-Sc | 3.1e+10 | 60.98 | 7.7 | 0.88 | Sy2.5 HII |
| NGC4527 | 1 | 4 | 4 | 1.00 | 38.52 | 4 | 0.50 | 2 | 1.95 | 0.05 | Sbc-Sc | 1.5e+10 | 10.06 | 13.5 | 2.1 | LINER HII |
| NGC1073 | 1 | 9 | 9 | 0.95 | 38.57 | 9 | 0.83 | 2 | 1.90 | 0.10 | Sbc-Sc | 1.0e+10 | 17.16 | 15.2 | 0.15 | - |
| NGC5033 | 1 | 4 | 4 | 0.50 | 38.72 | 4 | 0.78 | 2 | 1.87 | 0.13 | Sbc-Sc | 2.9e+10 | 42.26 | 15.2 | 1.5 | Sy1.9 |
| NGC5426 | 1 | 3 | 2 | 0.70 | 39.08 | 2 | 0.24 | 3 | 1.85 | 0.15 | Sbc-Sc | 2.6e+10 | 3.77 | 35.9 | <0.056 | - |
| NGC7541 | 1 | 14 | 14 | 1.00 | 38.57 | 13 | 0.69 | 2 | 1.84 | 0.16 | Sbc-Sc | 4.1e+10 | 3.32 | 33.4 | 10.5 | HII |
| NGC5427 | 1 | 3 | 3 | 0.50 | 39.13 | 3 | 0.24 | 2 | 1.83 | 0.17 | Sbc-Sc | 4.5e+10 | 5.32 | 38.1 | 3.2 | Sy2 |
| PGC14617 | 2 | 2 | 2 | 1.00 | 37.87 | 2 | 0.41 | 1 | 0.98 | 0.02 | Sbc-Sc | 2.0e+09 | 1.62 | 18.2 | 0.03 | - |
| NGC3066 | 1 | 1 | 1 | 0.78 | 39.27 | 1 | 0.03 | 1 | 0.97 | 0.03 | Sbc-Sc | 8.0e+09 | 0.85 | 32.4 | 1.5 | - |
| NGC3877 | 5 | 20 | 13 | 1.00 | 37.98 | 12 | 1.14 | 1 | 0.95 | 0.05 | Sbc-Sc | 2.1e+10 | 5.53 | 17.0 | 0.74 | - |
| NGC4639 | 1 | 2 | 2 | 1.00 | 39.32 | 2 | 0.06 | 1 | 0.94 | 0.06 | Sbc-Sc | 1.2e+10 | 4.03 | 20.8 | 0.27 | Sy1.8 |
| NGC5055 | 2 | 54 | 52 | 0.96 | 37.42 | 51 | 11.51 | 2 | 0.93 | 0.07 | Sbc-Sc | 2.7e+10 | 71.53 | 8.5 | 1.3 | LINER HII |
| NGC4258 | 3 | 50 | 40 | 0.65 | 37.52 | 40 | 9.59 | 1 | 0.93 | 0.07 | Sbc-Sc | 3.6e+10 | 105.88 | 7.727 | 0.59 | Sy1.9 LINER |
| NGC5643 | 1 | 5 | 5 | 0.64 | 38.52 | 5 | 0.69 | 1 | 0.92 | 0.08 | Sbc-Sc | 3.6e+10 | 14.32 | 16.9 | 2.4 | Sy2 |
| NGC3079 | 1 | 25 | 24 | 1.00 | 38.08 | 23 | 1.71 | 1 | 0.91 | 0.09 | Sbc-Sc | 3.2e+10 | 8.98 | 17.3 | 6.7 | Sy2 LINER |
| NGC3521 | 1 | 24 | 24 | 0.98 | 38.13 | 24 | 3.71 | 1 | 0.86 | 0.14 | Sbc-Sc | 3.9e+10 | 44.07 | 11.5 | 2.6 | LINER |
| NGC5005 | 1 | 4 | 4 | 1.00 | 38.98 | 4 | 0.54 | 1 | 0.81 | 0.19 | Sbc-Sc | 5.9e+10 | 12.49 | 21.3 | 4.5 | Sy2 LINER |
| NGC4321 | 1 | 33 | 32 | 0.97 | 37.77 | 30 | 7.44 | 1 | 0.81 | 0.19 | Sbc-Sc | 3.1e+10 | 36.83 | 14.13 | 1.7 | LINER HII |
| NGC7090 | 2 | 14 | 10 | 1.00 | 37.27 | 10 | 1.26 | 0 | -0.00 | 0.00 | Sbc-Sc | 5.3e+09 | 7.34 | 6.6 | 0.12 | - |
| NGC5949 | 1 | 1 | 1 | 1.00 | 38.52 | 1 | 0.06 | 0 | -0.00 | 0.00 | Sbc-Sc | 2.2e+09 | 1.83 | 10.9 | 0.064 | - |
| NGC7640 | 1 | 1 | 1 | 0.97 | 38.47 | 1 | 0.18 | 0 | -0.01 | 0.01 | Sbc-Sc | 6.8e+09 | 16.46 | 7.0 | 0.037 | - |
| NGC1637 | 7 | 14 | 6 | 1.00 | 37.42 | 6 | 2.10 | 0 | -0.01 | 0.01 | Sbc-Sc | 3.9e+09 | 10.13 | 8.9 | 0.23 | - |
| NGC1058 | 2 | 7 | 5 | 1.00 | 37.83 | 5 | 0.60 | 0 | -0.01 | 0.01 | Sbc-Sc | 3.1e+09 | 6.69 | 9.1 | 0.097 | Sy2 |
| NGC5879 | 1 | 9 | 8 | 0.91 | 37.38 | 8 | 1.48 | 0 | -0.02 | 0.02 | Sbc-Sc | 6.5e+09 | 4.38 | 12.3 | 0.2 | LINER |
| NGC4136 | 2 | 8 | 7 | 1.00 | 37.68 | 7 | 1.88 | 1 | -0.02 | 0.02 | Sbc-Sc | 3.3e+09 | 11.63 | 9.7 | 0.059 | HII |

Table 1—Continued

| Galaxy (1) | $N_{obs}$ (2) | $N^a_{src}$ (3) | $N^t_X$ (4) | $f_{Cov}$ (5) | lg $L_{X,lim}$ (6) | $N_X$ (7) | $N_{b/f}$ (8) | $N^a_U$ (9) | $n_U$ (10) | $n_{b/f}$ (11) | GType (12) | $L_B$ (13) | GArea (14) | Dist. (15) | $SFR_{60\mu m}$ (16) | activity (17) |
|---|---|---|---|---|---|---|---|---|---|---|---|---|---|---|---|---|
| NGC3344 | 1 | 0 | 0 | 1.00 | 38.27 | 0 | 0.48 | 0 | -0.02 | 0.02 | Sbc-Sc | 3.6e+09 | 35.92 | 6.1 | 0.16 | - |
| NGC253 | 4 | 105 | 101 | 0.73 | 36.27 | 101 | 26.60 | 0 | -0.02 | 0.02 | Sbc-Sc | 2.0e+10 | 146.21 | 3.0 | 3.8 | Sbrst HII |
| NGC5236 | 2 | 106 | 102 | 0.85 | 36.77 | 101 | 20.11 | 0 | -0.03 | 0.03 | Sbc-Sc | 2.2e+10 | 116.13 | 4.7 | 2.7 | Sbrst HII |
| NGC4647 | 1 | 20 | 9 | 0.71 | 38.02 | 8 | 0.70 | 0 | -0.03 | 0.03 | Sbc-Sc | 8.2e+09 | 5.16 | 16.8 | 0.67 | - |
| NGC4096 | 1 | 2 | 2 | 1.00 | 38.77 | 2 | 0.14 | 0 | -0.03 | 0.03 | Sbc-Sc | 1.1e+10 | 9.23 | 11.2 | 0.43 | - |
| NGC4062 | 1 | 0 | 0 | 1.00 | 38.83 | 0 | 0.12 | 0 | -0.03 | 0.03 | Sbc-Sc | 8.6e+09 | 5.58 | 13.5 | 0.21 | HII |
| NGC3683 | 2 | 12 | 12 | 1.00 | 38.38 | 12 | 0.23 | 2 | -0.03 | 0.03 | Sbc-Sc | 1.3e+10 | 1.02 | 28.4 | 5.1 | - |
| NGC7537 | 1 | 3 | 3 | 1.00 | 38.63 | 3 | 0.21 | 0 | -0.06 | 0.06 | Sbc-Sc | 1.6e+10 | 1.02 | 35.3 | <0.015 | - |
| NGC4414 | 1 | 2 | 2 | 1.00 | 39.13 | 2 | 0.11 | 0 | -0.06 | 0.06 | Sbc-Sc | 2.6e+10 | 5.83 | 17.22 | 4.0 | LINER |
| NGC3486 | 1 | 0 | 0 | 1.00 | 38.77 | 0 | 0.60 | 0 | -0.12 | 0.12 | Sbc-Sc | 1.1e+10 | 29.14 | 12.3 | 0.42 | Sy2 |
| NGC628 | 4 | 56 | 51 | 1.00 | 37.38 | 51 | 18.82 | 1 | -0.15 | 0.15 | Sbc-Sc | 1.8e+10 | 78.69 | 9.7 | 0.89 | - |
| NGC4303 | 1 | 25 | 24 | 0.97 | 37.98 | 23 | 4.99 | 0 | -0.18 | 0.18 | Sbc-Sc | 3.2e+10 | 29.22 | 15.2 | 4.0 | Sy2 HII |
| NGC4490 | 3 | 36 | 30 | 1.00 | 37.27 | 30 | 3.38 | 4 | 3.98 | 0.02 | Scd-Sd | 1.1e+10 | 15.24 | 7.8 | 1.3 | - |
| NGC3395 | 1 | 8 | 7 | 0.87 | 38.63 | 7 | 0.25 | 4 | 3.94 | 0.06 | Scd-Sd | 1.7e+10 | 1.99 | 27.4 | 2.26 | - |
| NGC5457 | 26 | 251 | 199 | 0.87 | 36.87 | 186 | 125.86 | 5 | 2.64 | 0.36 | Scd-Sd | 3.8e+10 | 609.74 | 6.855 | 0.182 | - |
| NGC4559 | 3 | 9 | 8 | 0.88 | 37.38 | 8 | 2.20 | 2 | 1.98 | 0.02 | Scd-Sd | 6.5e+09 | 36.71 | 5.8 | 0.092 | HII |
| NGC925 | 1 | 6 | 6 | 0.92 | 38.57 | 6 | 0.65 | 2 | 1.94 | 0.06 | Scd-Sd | 1.3e+10 | 48.56 | 9.12 | 0.29 | HII |
| NGC7424 | 2 | 18 | 15 | 0.74 | 37.72 | 15 | 8.00 | 2 | 1.85 | 0.15 | Scd-Sd | 9.4e+09 | 60.84 | 11.5 | 0.071 | - |
| NGC7793 | 1 | 23 | 23 | 0.96 | 36.52 | 23 | 10.61 | 1 | 0.99 | 0.01 | Scd-Sd | 3.8e+09 | 46.36 | 3.7 | 0.055 | HII |
| NGC5585 | 1 | 6 | 6 | 0.98 | 37.87 | 6 | 1.03 | 1 | 0.99 | 0.01 | Scd-Sd | 2.9e+09 | 16.83 | 7.0 | 0.022 | HII |
| NGC5474 | 1 | 3 | 3 | 1.00 | 38.27 | 3 | 0.21 | 1 | 0.99 | 0.01 | Scd-Sd | 1.7e+09 | 15.99 | 6.0 | 0.021 | HII |
| NGC2500 | 1 | 2 | 2 | 1.00 | 38.57 | 2 | 0.12 | 1 | 0.99 | 0.01 | Scd-Sd | 2.5e+09 | 5.93 | 10.1 | 0.096 | - |
| NGC1313 | 7 | 16 | 15 | 1.00 | 36.87 | 15 | 6.21 | 1 | 0.99 | 0.01 | Scd-Sd | 4.1e+09 | 49.57 | 3.7 | 0.22 | HII |
| PGC44014 | 1 | 1 | 1 | 1.00 | 38.57 | 1 | 0.22 | 1 | 0.98 | 0.02 | Scd-Sd | 3.8e+09 | 4.53 | 14.2 | 0.051 | - |
| NGC4945 | 1 | 31 | 31 | 0.86 | 37.08 | 31 | 8.72 | 1 | 0.98 | 0.02 | Scd-Sd | 4.4e+10 | 59.57 | 5.2 | 7.2 | Sy2 |
| NGC4631 | 1 | 26 | 26 | 0.83 | 36.93 | 25 | 8.78 | 1 | 0.98 | 0.02 | Scd-Sd | 2.6e+10 | 32.83 | 6.9 | 1.8 | - |
| NGC6946 | 5 | 88 | 67 | 0.99 | 36.98 | 66 | 17.09 | 1 | 0.97 | 0.03 | Scd-Sd | 3.6e+10 | 88.18 | 5.5 | 0.74 | HII |
| NGC2541 | 1 | 1 | 1 | 1.00 | 38.77 | 1 | 0.24 | 1 | 0.96 | 0.04 | Scd-Sd | 4.6e+09 | 15.64 | 11.27 | 0.08 | LINER |
| NGC3495 | 1 | 1 | 1 | 1.00 | 38.83 | 1 | 0.20 | 1 | 0.95 | 0.05 | Scd-Sd | 2.4e+10 | 4.62 | 17.6 | 0.25 | - |
| NGC5774 | 1 | 7 | 6 | 0.93 | 38.22 | 6 | 1.31 | 2 | 0.84 | 0.16 | Scd-Sd | 1.1e+10 | 5.83 | 26.8 | 0.18 | - |
| NGC598 | 28 | 434 | 292 | 0.53 | 35.38 | 255 | 237.18 | 0 | 0.00 | 0.00 | Scd-Sd | 5.2e+09 | 2318.71 | 0.8166 |  | HII |
| NGC4020 | 1 | 0 | 0 | 1.00 | 38.47 | 0 | 0.02 | 0 | -0.00 | 0.00 | Scd-Sd | 7.5e+08 | 1.50 | 8.0 | <0.0011 | - |
| NGC3274 | 1 | 1 | 1 | 1.00 | 38.22 | 1 | 0.03 | 0 | -0.00 | 0.00 | Scd-Sd | 4.5e+08 | 1.71 | 5.9 | 0.015 | - |
| NGC7320 | 1 | 3 | 3 | 0.97 | 37.98 | 3 | 0.31 | 0 | -0.01 | 0.01 | Scd-Sd | 2.8e+09 | 2.01 | 13.8 | <0.0044 | HII |
| NGC672 | 2 | 1 | 1 | 1.00 | 38.42 | 1 | 0.22 | 0 | -0.01 | 0.01 | Scd-Sd | 5.3e+09 | 14.56 | 7.4 | 0.076 | HII |
| NGC6503 | 2 | 6 | 6 | 1.00 | 37.42 | 6 | 1.50 | 0 | -0.01 | 0.01 | Scd-Sd | 5.2e+09 | 13.35 | 6.1 | 0.17 | LINER HII |
| NGC4713 | 1 | 2 | 2 | 1.00 | 38.32 | 2 | 0.20 | 0 | -0.01 | 0.01 | Scd-Sd | 3.3e+09 | 3.60 | 10.9 | 0.23 | LINER |
| NGC4244 | 1 | 5 | 5 | 0.81 | 36.63 | 5 | 4.94 | 0 | -0.01 | 0.01 | Scd-Sd | 5.3e+09 | 24.77 | 4.2 | 0.004 | HII |
| NGC6690 | 1 | 1 | 1 | 1.00 | 38.68 | 1 | 0.11 | 0 | -0.02 | 0.02 | Scd-Sd | 4.2e+09 | 3.76 | 12.8 | 0.051 | - |
| NGC5068 | 1 | 3 | 3 | 0.97 | 37.87 | 3 | 1.89 | 0 | -0.02 | 0.02 | Scd-Sd | 6.4e+09 | 35.82 | 6.7 | 0.1 | - |
| NGC3556 | 1 | 31 | 30 | 0.99 | 37.18 | 28 | 4.06 | 0 | -0.02 | 0.02 | Scd-Sd | 1.3e+10 | 15.31 | 8.6 | 0.87 | - |
| NGC1493 | 1 | 3 | 3 | 1.00 | 38.08 | 3 | 0.81 | 0 | -0.02 | 0.02 | Scd-Sd | 3.9e+09 | 8.75 | 11.3 | 0.13 | - |
| NGC1003 | 1 | 2 | 2 | 1.00 | 38.57 | 2 | 0.17 | 0 | -0.02 | 0.02 | Scd-Sd | 5.8e+09 | 8.03 | 9.9 | 0.11 | - |
| NGC2403 | 5 | 82 | 55 | 0.83 | 36.42 | 54 | 32.96 | 1 | -0.03 | 0.03 | Scd-Sd | 6.4e+09 | 211.36 | 3.133 | 0.23 | HII |
| NGC7741 | 1 | 0 | 0 | 1.00 | 38.63 | 0 | 0.34 | 0 | -0.04 | 0.04 | Scd-Sd | 6.6e+09 | 10.07 | 12.6 | 0.16 | - |

Table 1—Continued

| Galaxy (1) | $N_{obs}$ (2) | $N^a_{src}$ (3) | $N^t_X$ (4) | $f_{Cov}$ (5) | lg $L_{X,lim}$ (6) | $N_X$ (7) | $N_{b/f}$ (8) | $N^a_U$ (9) | $n_U$ (10) | $n_{b/f}$ (11) | GType (12) | $L_B$ (13) | GArea (14) | Dist. (15) | $SFR_{60\mu m}$ (16) | activity (17) |
|---|---|---|---|---|---|---|---|---|---|---|---|---|---|---|---|---|
| IC5332 | 2 | 27 | 22 | 1.00 | 37.18 | 21 | 9.98 | 0 | -0.04 | 0.04 | Scd-Sd | 4.7e+09 | 37.54 | 8.4 | 0.026 | - |
| NGC3184 | 2 | 37 | 36 | 1.00 | 37.22 | 34 | 10.51 | 0 | -0.05 | 0.05 | Scd-Sd | 8.5e+09 | 40.33 | 8.7 | 0.082 | HII |
| NGC4701 | 1 | 1 | 1 | 1.00 | 38.63 | 1 | 0.43 | 0 | -0.07 | 0.07 | Scd-Sd | 6.6e+09 | 4.64 | 20.5 | 0.51 | - |
| NGC4654 | 1 | 2 | 2 | 1.00 | 38.72 | 2 | 0.51 | 0 | -0.09 | 0.09 | Scd-Sd | 2.2e+10 | 10.85 | 16.8 | 1.8 | - |
| NGC988 | 1 | 3 | 3 | 1.00 | 38.77 | 3 | 0.49 | 0 | -0.10 | 0.10 | Scd-Sd | 2.2e+10 | 8.85 | 18.3 | 0.35 | - |
| NGC4038 | 7 | 44 | 17 | 0.91 | 38.18 | 17 | 2.95 | 13 | 5.71 | 0.29 | Sdm-Sm | 5.7e+10 | 12.68 | 25.5 | 8.2 | Sbrst |
| NGC4039 | 7 | 26 | 10 | 0.66 | 38.18 | 10 | 0.65 | 7 | 2.94 | 0.06 | Sdm-Sm | 5.1e+10 | 3.85 | 25.3 | 5.5 | Sbrst |
| PGC71926 | 1 | 2 | 2 | 1.00 | 39.32 | 2 | 0.27 | 2 | 1.73 | 0.27 | Sdm-Sm | 4.5e+09 | 4.84 | 35.1 | <0.067 | - |
| NGC5204 | 13 | 8 | 5 | 0.91 | 36.63 | 5 | 1.64 | 1 | 1.00 | 0.00 | Sdm-Sm | 7.3e+08 | 11.91 | 4.3 | 0.019 | HII |
| NGC4561 | 1 | 3 | 3 | 1.00 | 38.57 | 3 | 0.06 | 1 | 0.99 | 0.01 | Sdm-Sm | 1.7e+09 | 1.55 | 12.3 | 0.082 | - |
| PGC48179 | 2 | 1 | 1 | 1.00 | 38.93 | 1 | 0.19 | 1 | 0.93 | 0.07 | Sdm-Sm | 7.4e+09 | 3.54 | 22.7 | 0.18 | - |
| NGC625 | 1 | 5 | 5 | 0.98 | 36.47 | 5 | 2.44 | 0 | -0.00 | 0.00 | Sdm-Sm | 7.7e+08 | 8.60 | 3.9 | 0.035 | HII |
| NGC55 | 2 | 51 | 51 | 0.86 | 35.83 | 47 | 21.05 | 0 | -0.00 | 0.00 | Sdm-Sm | 3.0e+09 | 142.83 | 1.48 | 0.076 | - |
| NGC4625 | 1 | 1 | 1 | 1.00 | 38.57 | 1 | 0.04 | 0 | -0.00 | 0.00 | Sdm-Sm | 7.4e+08 | 3.25 | 8.2 | 0.036 | - |
| NGC3985 | 1 | 0 | 0 | 1.00 | 38.52 | 0 | 0.01 | 0 | -0.00 | 0.00 | Sdm-Sm | 7.4e+08 | 0.82 | 8.3 | 0.043 | - |
| NGC1507 | 1 | 1 | 1 | 1.00 | 38.57 | 1 | 0.05 | 0 | -0.00 | 0.00 | Sdm-Sm | 2.9e+09 | 2.46 | 10.0 | 0.068 | - |
| NGC959 | 1 | 0 | 0 | 1.00 | 38.68 | 0 | 0.05 | 0 | -0.01 | 0.01 | Sdm-Sm | 2.0e+09 | 2.65 | 10.6 | 0.056 | - |
| NGC4204 | 1 | 1 | 1 | 1.00 | 38.42 | 1 | 0.15 | 0 | -0.01 | 0.01 | Sdm-Sm | 7.9e+08 | 8.29 | 7.9 | 0.02 | - |
| NGC2552 | 1 | 0 | 0 | 1.00 | 38.08 | 0 | 0.47 | 0 | -0.01 | 0.01 | Sdm-Sm | 1.9e+09 | 6.20 | 10.0 | 0.028 | - |
| IC3259 | 1 | 0 | 0 | 1.00 | 38.38 | 0 | 0.15 | 0 | -0.01 | 0.01 | Sdm-Sm | 1.5e+09 | 1.26 | 18.9 | <0.0051 | - |
| IC2574 | 1 | 6 | 5 | 0.59 | 37.02 | 4 | 3.17 | 0 | -0.01 | 0.01 | Sdm-Sm | 1.4e+09 | 55.48 | 3.5 | 0.013 | - |
| IC1727 | 2 | 0 | 0 | 1.00 | 38.32 | 0 | 0.22 | 0 | -0.01 | 0.01 | Sdm-Sm | 1.9e+09 | 16.85 | 6.4 | 0.011 | LINER |
| NGC4395 | 5 | 12 | 12 | 0.81 | 36.77 | 12 | 7.43 | 0 | -0.02 | 0.02 | Sdm-Sm | 1.2e+09 | 113.45 | 3.6 | 0.014 | Sy1.8 LINER |
| NGC3432 | 1 | 1 | 1 | 1.00 | 38.83 | 1 | 0.14 | 0 | -0.03 | 0.03 | Sdm-Sm | 9.6e+09 | 7.86 | 12.7 | 0.62 | LINER HII |
| NGC45 | 3 | 7 | 7 | 0.99 | 37.47 | 7 | 5.96 | 0 | -0.04 | 0.04 | Sdm-Sm | 3.8e+09 | 39.48 | 8.1 | 0.012 | - |
| NGC4234 | 1 | 0 | 0 | 0.85 | 39.42 | 0 | 0.04 | 0 | -0.04 | 0.04 | Sdm-Sm | 8.3e+09 | 1.33 | 32.9 | 0.73 | - |
| NGC3445 | 1 | 0 | 0 | 0.93 | 39.47 | 0 | 0.06 | 1 | -0.06 | 0.06 | Sdm-Sm | 1.2e+10 | 1.88 | 32.4 | 0.99 | - |
| NGC1189 | 1 | 1 | 1 | 1.00 | 38.68 | 1 | 0.40 | 0 | -0.12 | 0.12 | Sdm-Sm | 3.7e+09 | 2.08 | 34.5 | <0.028 | - |

Note. — The columns are: (1) Galaxy name; (2) number of observations; (3) number of X-ray point sources detected above $4\sigma$ in all observations; (4) number of sources detected in the stitched deep survey; (5) the surveyed area A as a fraction of $D_{25}$ isophotal area; (6) the limiting $L_X$ at which the surveyed blue light is 50% of the total blue light surveyed; (7) number of sources detected above $L_{X,lim}$; (8) the predicted foreground/background sources for $L > L_{X,lim}$; (9) the number of ULXs found in all observations; (10) the number of ULXs detected in the deep survey minus the predicted foreground/background sources for $L > 2 \times 10^{39}$ erg s$^{-1}$; (11) the predicted foreground/background sources for $L > 2 \times 10^{39}$ erg s$^{-1}$; (12) the galaxy type; (13) the blue light content of the galaxy in unit of $L_\odot$; (14) the $D_{25}$ isophotal area in unit of arcmin$^2$; (15) the galaxy distance; (16) the SFR in $M_\odot$/yr estimated based on the flux density at $60\mu$m observed by IRAS; (17) the star-forming and nuclear activities.

Table 2. ULX Rates for Different Survey Galaxy Samples

| | | | | | | | | $L_X > 2\times10^{39}$ erg s$^{-1}$ | | | | | $L_X > 4\times10^{39}$ erg s$^{-1}$ | | | | | $L_X > 1\times10^{40}$ erg s$^{-1}$ | | | | |
|---|---|---|---|---|---|---|---|---|---|---|---|---|---|---|---|---|---|---|---|---|---|---|
| Sample | $N_{gal}$ | $N^a_{src}$ | $N^a_U$ | Area | $L_B$ | $N_X$ | $N_{b/f}$ | $n_U$ | $n_G$ | $n_{b/f}$ | $U/G$ | $U/L_B$ | $n_U$ | $n_G$ | $n_{b/f}$ | $U/G$ | $U/L_B$ | $n_U$ | $n_G$ | $n_{b/f}$ | $U/G$ | $U/L_B$ |
| (1) | (2) | (3) | (4) | (5) | (6) | (7) | (8) | (9) | (10) | (11) | (12) | (13) | (14) | (15) | (16) | (17) | (18) | (19) | (20) | (21) | (22) | (23) |
| all | 343 | 5920 | 282 | 9.9e+07 | 247.4 | 4970 | 1170.56 | 218 | 117 | 33.1 | 0.54±0.04 | 0.75±0.06 | 98 | 91 | 14.1 | 0.24±0.03 | 0.34±0.04 | 31 | 66 | 4.0 | 0.08±0.02 | 0.11±0.02 |
| early | 130 | 2311 | 66 | 2.1e+07 | 129.1 | 1945 | 259.86 | 49 | 58 | 17.3 | 0.24±0.05 | 0.25±0.05 | 17 | 47 | 7.5 | 0.07±0.03 | 0.07±0.03 | 6 | 33 | 2.1 | 0.03±0.02 | 0.03±0.02 |
| late | 213 | 3609 | 216 | 7.8e+07 | 118.3 | 3025 | 910.7 | 169 | 59 | 15.7 | 0.72±0.06 | 1.30±0.11 | 81 | 44 | 6.6 | 0.35±0.04 | 0.63±0.08 | 25 | 33 | 2.0 | 0.11±0.02 | 0.19±0.04 |
| elliptical | 55 | 1509 | 47 | 8.7e+06 | 81.4 | 1299 | 123.59 | 34 | 28 | 10.5 | 0.43±0.11 | 0.29±0.07 | 10 | 21 | 4.5 | 0.10±0.06 | 0.07±0.04 | 5 | 15 | 1.2 | 0.07±0.04 | 0.05±0.03 |
| lenticular | 75 | 802 | 19 | 1.2e+07 | 47.6 | 646 | 136.27 | 15 | 30 | 6.8 | 0.11±0.05 | 0.17±0.08 | 7 | 26 | 3.0 | 0.05±0.04 | 0.08±0.06 | 1 | 18 | 0.8 | 0.00±0.01 | 0.00±0.02 |
| spiral | 187 | 3380 | 190 | 7.5e+07 | 113.7 | 2865 | 874.4 | 154 | 56 | 14.9 | 0.74±0.07 | 1.22±0.11 | 70 | 42 | 6.2 | 0.34±0.04 | 0.56±0.07 | 20 | 32 | 1.9 | 0.10±0.02 | 0.16±0.04 |
| irregular | 21 | 173 | 8 | 2.9e+06 | 2.3 | 124 | 31.52 | 7 | 1 | 0.2 | 0.32±0.13 | 3.00±1.17 | 5 | 1 | 0.1 | 0.23±0.11 | 2.17±0.99 | 2 | 0 | 0.0 | 0.09±0.07 | 0.87±0.63 |
| peculiar | 5 | 56 | 18 | 3.3e+05 | 2.4 | 36 | 4.75 | 8 | 2 | 0.6 | 1.48±0.57 | 3.13±1.20 | 6 | 1 | 0.3 | 1.15±0.49 | 2.43±1.04 | 3 | 1 | 0.1 | 0.58±0.35 | 1.24±0.73 |
| S0/a-Sa | 32 | 395 | 23 | 4.4e+06 | 19.3 | 355 | 44.88 | 20 | 18 | 2.8 | 0.54±0.14 | 0.89±0.23 | 8 | 15 | 1.1 | 0.21±0.09 | 0.36±0.15 | 1 | 11 | 0.3 | 0.02±0.03 | 0.03±0.05 |
| Sab-Sb | 52 | 788 | 51 | 1.4e+07 | 40.7 | 718 | 135.96 | 40 | 25 | 5.6 | 0.66±0.12 | 0.84±0.16 | 17 | 19 | 2.4 | 0.28±0.08 | 0.36±0.10 | 4 | 16 | 0.7 | 0.06±0.04 | 0.08±0.05 |
| Sbc-Sc | 42 | 850 | 57 | 1.3e+07 | 33.5 | 754 | 144.26 | 51 | 12 | 3.8 | 1.12±0.17 | 1.41±0.21 | 26 | 7 | 1.5 | 0.58±0.12 | 0.73±0.15 | 11 | 5 | 0.5 | 0.25±0.08 | 0.31±0.10 |
| Scd-Sd | 38 | 1177 | 33 | 3.8e+07 | 12.6 | 915 | 501.74 | 29 | 0 | 1.6 | 0.72±0.14 | 2.17±0.43 | 12 | 0 | 0.7 | 0.30±0.09 | 0.89±0.27 | 1 | 0 | 0.3 | 0.02±0.03 | 0.06±0.08 |
| Sdm-Sm | 23 | 170 | 26 | 5.5e+06 | 7.5 | 123 | 47.59 | 14 | 1 | 1.1 | 0.56±0.16 | 1.72±0.50 | 7 | 1 | 0.5 | 0.28±0.12 | 0.87±0.35 | 3 | 0 | 0.1 | 0.12±0.08 | 0.38±0.23 |
| AGN | 121 | 2595 | 101 | 3.6e+07 | 113.3 | 2222 | 377.13 | 85 | 72 | 13.6 | 0.59±0.08 | 0.63±0.08 | 32 | 57 | 5.5 | 0.22±0.05 | 0.23±0.05 | 10 | 42 | 1.5 | 0.07±0.03 | 0.07±0.03 |
| nAGN | 227 | 3328 | 181 | 6.3e+07 | 134.5 | 2751 | 793.9 | 133 | 45 | 19.5 | 0.50±0.05 | 0.84±0.09 | 66 | 34 | 8.6 | 0.25±0.04 | 0.43±0.06 | 21 | 24 | 2.5 | 0.08±0.02 | 0.14±0.03 |
| LAGN | 80 | 1327 | 73 | 2.4e+07 | 65.2 | 1210 | 218.9 | 63 | 44 | 8.0 | 0.69±0.10 | 0.84±0.12 | 26 | 33 | 3.2 | 0.28±0.06 | 0.35±0.08 | 6 | 25 | 0.9 | 0.06±0.03 | 0.08±0.04 |
| LnAGN | 133 | 2282 | 143 | 5.4e+07 | 53.2 | 1815 | 691.8 | 106 | 15 | 7.7 | 0.74±0.08 | 1.85±0.19 | 55 | 11 | 3.4 | 0.39±0.06 | 0.97±0.14 | 19 | 8 | 1.0 | 0.14±0.03 | 0.34±0.08 |
| sfrl02 | 208 | 3232 | 96 | 5.6e+07 | 127.9 | 2735 | 690.86 | 73 | 51 | 17.9 | 0.26±0.04 | 0.43±0.07 | 28 | 40 | 7.5 | 0.10±0.03 | 0.16±0.04 | 6 | 28 | 2.2 | 0.02±0.01 | 0.03±0.02 |
| sfrg02 | 90 | 1760 | 69 | 3.1e+07 | 70.7 | 1434 | 343.85 | 55 | 41 | 8.9 | 0.51±0.08 | 0.65±0.10 | 25 | 30 | 3.9 | 0.23±0.06 | 0.30±0.07 | 11 | 20 | 1.1 | 0.11±0.04 | 0.14±0.05 |
| sfrg2 | 45 | 928 | 117 | 1.2e+07 | 48.8 | 801 | 135.85 | 90 | 25 | 6.3 | 1.86±0.21 | 1.72±0.19 | 45 | 21 | 2.7 | 0.94±0.15 | 0.87±0.14 | 14 | 18 | 0.7 | 0.29±0.08 | 0.27±0.08 |
| Sbrst | 15 | 529 | 62 | 5.9e+06 | 16.7 | 403 | 83.82 | 37 | 5 | 2.3 | 2.32±0.41 | 2.08±0.36 | 18 | 5 | 1.1 | 1.13±0.28 | 1.01±0.25 | 7 | 3 | 0.3 | 0.45±0.18 | 0.40±0.16 |

Note. — The columns are: (1) name of the galaxy survey sample; (2) the number of surveyed galaxies; (3) the number of point sources above $4\sigma$ detected from all observations; (4) the number of ULXs detected from all observations; (5) the surveyed sky area in pixel$^2$ from the stitched deep survey of individual galaxies; (6) the surveyed blue light content in unit of $10^{10}L_\odot$; (7) the total number of X-ray point sources detected in the stitched survey; (8) the number of foreground/background objects expected for the survey; (9) the number of ULXs ($L_X > 2\times10^{39}$ erg s$^{-1}$) in the survey; (10) the number of galaxies with at least one ULX ($L_X > 2\times10^{39}$ erg s$^{-1}$) in the survey; (11) the number of predicted contaminating sources with $L_X > 2\times10^{39}$ erg s$^{-1}$; (12) the net number of ULXs ($L_X > 2\times10^{39}$ erg s$^{-1}$) per surveyed galaxy and its error; (13) the net number of ULXs ($L_X > 2\times10^{39}$ erg s$^{-1}$) per $10^{10}L_\odot$ blue light and its error; (14) the number of ULX ($L_X > 4\times10^{39}$ erg s$^{-1}$) in the survey; (15) the number of galaxies with at least one ULX ($L_X > 4\times10^{39}$ erg s$^{-1}$) in the survey; (16) the number of predicted contaminating sources with $L_X > 4\times10^{39}$ erg s$^{-1}$; (17) the net number of ULXs ($L_X > 4\times10^{39}$ erg s$^{-1}$) per surveyed galaxy and its error; (18) the net number of ULXs ($L_X > 4\times10^{39}$ erg s$^{-1}$) per $10^{10}L_\odot$ blue light and its error; (19) the number of ULX ($L_X > 10^{40}$ erg s$^{-1}$) in the survey; (20) the number of galaxies with at least one ULX ($L_X > 10^{40}$ erg s$^{-1}$) in the survey; (21) the number of predicted contaminating sources with $L_X > 10^{40}$ erg s$^{-1}$; (22) the net number of ULXs ($L_X > 10^{40}$ erg s$^{-1}$) per surveyed galaxy and its error; (23) the net number of ULXs ($L_X > 10^{40}$ erg s$^{-1}$) per $10^{10}L_\odot$ blue light and its error.

Table 3. Single and Broken Power Fits to Differential Curves for Net Non-nuclear Sources

| | | | | single power-law | | | broken power-law | | | | | |
|---|---|---|---|---|---|---|---|---|---|---|---|---|
| Sample | $\lg L_{X1}$ | $\lg L_{X2}$ | $N_{bin}$ | $\chi^2_1$ | A | $\alpha$ | $\chi^2_2$ | *prob* | A | $\alpha$ | $L_b$ | $\alpha_2$ |
| (1) | (2) | (3) | (4) | (5) | (6) | (7) | (8) | (9) | (10) | (11) | (12) | (13) |
| all | 38.02 | 40.47 | 51 | 86.78 | 0.2 ± 2.2% | 0.98 ± 0.01 | 48.84 | 0.0498 | 0.21 ± 2.2% | 0.51 ± 0.06 | 38.42 ± 0.02 | 1.10 ± 0.02 |
| early | 38.13 | 40.13 | 42 | 78.95 | 0.15 ± 3.3% | 1.33 ± 0.02 | 35.53 | 0.0149 | 0.2 ± 3.2% | 1.02 ± 0.03 | 38.95 ± 0.01 | 2.29 ± 0.18 |
| late | 37.87 | 40.47 | 54 | 67.81 | 0.21 ± 3.2% | 0.78 ± 0.02 | 51.16 | 0.3187 | 0.24 ± 3.1% | 0.61 ± 0.03 | 38.80 ± 0.02 | 0.96 ± 0.05 |
| elliptical | 38.02 | 40.13 | 44 | 119.46 | 0.17 ± 3.6% | 1.21 ± 0.02 | 40.73 | 0.0055 | 0.19 ± 3.5% | 0.68 ± 0.11 | 38.65 ± 0.02 | 1.80 ± 0.03 |
| lenticular | 38.27 | 39.77 | 32 | 39.65 | 0.087 ± 8.6% | 1.50 ± 0.07 | 27.66 | 0.3412 | 0.1 ± 8.3% | 0.96 ± 0.10 | 38.87 ± 0.02 | 2.74 ± 0.10 |
| spiral | 37.87 | 40.47 | 54 | 67.54 | 0.21 ± 3.2% | 0.80 ± 0.02 | 50.62 | 0.3079 | 0.25 ± 3.2% | 0.64 ± 0.02 | 38.90 ± 0.04 | 1.02 ± 0.06 |
| irregular | 36.87 | 39.83 | 61 | 32.57 | 0.33 ± 6.6% | 0.26 ± 0.10 | | | | | | |
| peculiar | 38.42 | 40.27 | 39 | 12.61 | 0.32 ± 4.1% | 0.55 ± 0.30 | | | | | | |
| S0/a-Sa | 37.68 | 39.77 | 44 | 67.00 | 0.17 ± 6.5% | 0.98 ± 0.03 | 50.68 | 0.3772 | 0.14 ± 6.3% | -0.19 ± 0.01 | 37.98 ± 0.02 | 1.22 ± 0.03 |
| Sab-Sb | 37.87 | 40.08 | 46 | 73.19 | 0.17 ± 6.5% | 0.78 ± 0.03 | 40.46 | 0.0560 | 0.18 ± 6.1% | -0.08 ± 0.01 | 38.42 ± 0.03 | 1.13 ± 0.05 |
| Sbc-Sc | 37.87 | 40.42 | 53 | 46.47 | 0.2 ± 6.6% | 0.70 ± 0.04 | | | | | | |
| Scd-Sd | 37.22 | 39.87 | 55 | 56.83 | 0.2 ± 9.7% | 0.54 ± 0.04 | | | | | | |
| Sdm-Sm | 38.18 | 40.08 | 40 | 19.82 | 0.13 ± 6.0% | 0.34 ± 0.17 | | | | | | |
| sfrl02 | 38.02 | 40.13 | 44 | 100.59 | 0.18 ± 3.0% | 1.13 ± 0.02 | 59.79 | 0.1011 | 0.18 ± 2.9% | 0.76 ± 0.04 | 38.63 ± 0.02 | 1.49 ± 0.04 |
| sfrg02 | 38.42 | 40.32 | 40 | 35.16 | 0.17 ± 6.6% | 1.22 ± 0.07 | | | | | | |
| sfrg2 | 38.13 | 40.47 | 49 | 44.77 | 0.23 ± 5.7% | 0.78 ± 0.04 | | | | | | |
| Sbrst | 38.18 | 40.27 | 44 | 28.93 | 0.2 ± 11.7% | 0.54 ± 0.08 | | | | | | |

Note. — The columns are: (1) name of the galaxy survey sample; (2) the low luminosity end for the XLF curve; (3) the high luminosity end for the XLF curve; (4) the number of bins ($\delta \lg L = 0.05$) for the XLF curve; (5) the resulted $\chi^2$ for the single power-law fit; (6) the A parameter and error in percentage normalized by the surveyed blue light for the sample; (7) the power-law slope and error; (8) the resulted $\chi^2$ for the broken power-law fit; (9) the probability for the broken power-law fit is no better than the single power-law; (10) the A parameter and error in percentage normalized by the surveyed blue light for the sample; (11) the power-law slope and error; (12) the luminosity at which the power-law breaks; (13) the second power-law slope and error.